UNIVERSITY OF OKLAHOMA
GRADUATE COLLEGE

HYDRAULIC FRACTURE PROPAGATION IN ANISOTROPIC FORMATION AND PROPPANT TRANSPORT.

A THESIS

SUBMITTED TO THE GRADUATE FACULTY

in partial fulfillment of the requirements for the

DEGREE OF

MASTER OF SCIENCE

By

SREE SUJON SUTRADHOR

Norman, Oklahoma

2024

HYDRAULIC FRACTURE PROPAGATION IN ANISOTROPIC FORMATION AND

PROPPANT TRANSPORT.

A THESIS APPROVED FOR THE
MEWBOURNE SCHOOL OF PETROLEUM AND GEOLOGICAL ENGINEERING

BY THE COMMITTEE CONSISTING OF

Dr. Ahmad Ghassemi, Chair

Dr. Bor-Jier (Ben) Shiau

Dr. Catalin Teodoriu

Dr. Mashhad Fahes

Acknowledgements

I want to express my sincere gratitude to Dr. Ahmad Ghassemi, my advisor, for all his help, advice, and encouragement during my time at the University of Oklahoma. It has been incredibly fulfilling to work under his guidance, and I am incredibly grateful for the chances he has given me to learn and develop. His flexibility, tolerance, and unshakeable faith in my abilities have been crucial to my academic career. I look forward to continuing our collaboration and am excited about the future endeavors we may share.

I extend my heartfelt thanks to Dr. Dharmendra Kumar for his invaluable guidance and assistance, particularly in overcoming coding challenges. When I began my journey here, I had no prior experience working with FORTRAN. Dr. Kumar's guidance and unwavering support were instrumental in helping me acquire and develop this skill efficiently. I am also deeply grateful to Steve, our lab manager, for his unwavering support during my lab experiments. His assistance throughout each experiment made the procedure much smoother and more efficient.

In addition, my sincere thanks go to Dr. Zhi Ye, Dr. Yawei Li, and Sunghyun Ko (Danny) for their collaboration and support in the lab. Their assistance and shared knowledge greatly enriched my research experience. Additionally, I owe a special debt of gratitude to Dr. Varahanaresh Sesetty, whose papers and code provided the foundation for my understanding of hydraulic fracture modeling.

Finally, I would like to express my heartfelt appreciation to my friends and family for their constant encouragement and support throughout this journey. Their unwavering belief in me has been a source of strength and inspiration, and I attribute much of my success to their love and faith.

Thank you all for being an integral part of this chapter in my life.

Table of Contents:

List of Figures:

List of Tables:

Nomenclature:

Nomenclature			
A_{ij}	influence coefficients	g	gravitational acceleration
C_L	Carter leak-off coefficient, $m/s^{1/2}$	h	fracture height, m
D_i	displacement discontinuity components, m	n	number of perforations per cluster
D_n	normal displacement discontinuity, m	p	fluid pressure, Pa
D_s	shear displacement discontinuity, m	t	time, s
K_{IC}	fracture toughness, $MPa.m^{0.5}$	w	fracture width, m
K_I	Mode-I stress intensity factor, $MPa.m^{0.5}$	δ	dirac delta function
K_{II}	Mode-II stress intensity factor, $MPa.m^{0.5}$	σ	minimum in-situ horizontal stress, MPa
K_{II}	Mode-II stress intensity factor, $MPa.m^{0.5}$	ν	Poisons ratio
P_{perf}	frictional pressure drops due to perforation friction, MPa	μ	fluid viscosity, cp
Q_{inj}	volumetric injection rate, m^3/s	**Abbreviation**	
ρ_p	proppant density, kg/m^3	DD	Displacement Discontinuity
d_p	proppant diameter, m	DDM	Displacement Discontinuity Method
ρ_f	fluid density, kg/m^3	LDC	Low Density Ceramic Proppant
d_{ij}	Distance between two elements i and j	P3D	Pseudo-3D
q_L	fluid mass leak-off rate per unit area, $kg/m^2/s$	PC	Petroleum-Coke based proppant
u_i	displacement vector, m	RC	Resin-coated Ceramic proppant
σ_b	stress barrier above and below pay zone, MPa	SEM	Scanning Electron Microscopy
C	perforation discharge coefficient	SIF	Stress Intensity Factor
D	perforation diameter, inch	VTI	Vertical Transverse Isotropic
E	Young modulus, GPa		
G	shear modulus, Pa		
H	pay zone thickness, m		
L	fracture length, m		

Abstract

Recent advancements in hydraulic fracturing technology have significantly improved the extraction of hydrocarbons and geothermal energy from unconventional reservoirs. The efficiency of hydraulic fracturing in unconventional reservoirs is greatly influenced by proppant transport, fracture geometry, and in-situ stress conditions. Rock anisotropy is known to affect fracture aperture, size, and propagation trajectory and should be considered in modeling and design. We present results of a novel approach to considering proppant transport in multiple hydraulic fractures in anisotropic rock. We employ a DD-based numerical approach to simulate multi-cluster hydraulic fracture propagation under both symmetric and asymmetric stress barriers. The analysis includes the effects of fracture spacing and stress barriers in anisotropic formations, as well as the variation of propagation regime (viscous and toughness).

The study explores the critical role of proppant in maintaining fracture conductivity and controlling fracture closure. The effects of proppant size, density, concentration, and slurry injection rate on fracture network efficiency are investigated to optimize proppant distribution across clusters. Comparative analyses of fracture closure following injection, both with and without proppant, highlight the critical role of proppants in maintaining fracture openness. The findings highlight that well-designed proppant schedules can significantly improve fracture connectivity and enhance long-term reservoir performance, offering valuable insights for optimizing hydraulic fracturing operations in unconventional reservoirs.

Additionally, this study evaluates the performance of various proppant materials, including petroleum coke-based proppants (PC), high-transported ultra-low-density ceramic proppants (LDC), and resin-coated ceramic proppants (RC), focusing on their crush resistance and packing strength under simulated downhole conditions. Using the Standard procedure outlined in API ISO 13503-2, we assessed both dry proppants across two mesh sizes (10/35 and 35/60) and wet proppants that were exposed to high temperatures (300 °C) for 7, 14, and 30 days to simulate geothermal environments. The proppants were subjected to heat in the presence of water.

The dry test results indicate that petroleum coke-based proppants, despite their cost-effectiveness, exhibit significantly lower strength compared to ceramic proppants, with resin-coated ceramics showing exceptional stress tolerance exceeding 15,000 psi. Additionally, the study reveals that the crush resistance and packing strength of proppants generally diminish over time when exposed to high temperatures, with variations depending on the type and size of the proppant. Specifically, petroleum coke-based proppants demonstrated minimal reduction in strength after heat exposure, while ceramic-based proppants exhibited a more pronounced decrease in mechanical performance. Moreover, dry crush tests conducted on mixtures of PC with LDC and PC with RC at various proportions (at a stress level of 5,000 psi) shown that a mix of PC with LDC or RC substantially decreases the generation of fines, lowers compaction, and improves the overall mechanical properties of PC proppants. The findings emphasize the significance of taking temperature effects into account when selecting proppants for geothermal applications, particularly those that are ceramic-based, given the critical impact of prolonged high-temperature exposure on their mechanical integrity.

Introduction

The production of tight oil and shale gas in the United States has surged in recent years, with the country now holding some of the world's largest reserves. These resources are located in reservoirs characterized by extremely low permeability. Compared to conventional gas reservoirs, shale formations exhibit extremely low permeabilities, such as nano-Darcy permeability (Cipolla, 2009). In petroleum engineering, reservoir stimulation is commonly achieved by using hydraulic fracturing in horizontal wells through multiple clusters and stages. Hydraulic fracturing refers to the process of creating and expanding fractures in rocks through the application of hydraulic pressure using fluids. During hydraulic fracturing, the pressure inside the wellbore increased until the tensile stress around the rock or crack overcomes the tensile strength of the rock or fracture (Geertsma, n.d.). These multistage fracturing operations can be conducted either simultaneously or sequentially from perforation clusters. In simultaneous fracturing, multiple fractures are initiated and propagated simultaneously from the clusters, while in sequential fracturing, fractures are created one cluster at a time, with the previously formed fractures usually maintained either by propping them open or keeping them pressurized (Ghassemi & Zhang, 2019; Olson, 2008; Wu et al., 2017; Zhao et al., 2016). Schematic diagrams of multi-stage multi-cluster fractures are shown in Figure 1-1.1. In multi-cluster fracture propagation system, one fracture induces an additional stress on other fractures, and changes the in-situ stress conditions. This phenomenon is considered as stress shadow effects and has been studied a lot in numerical modeling (Kumar & Ghassemi, 2016; Sesetty et al., 2018a; Sesetty & Ghassemi, 2019; Spence & Sharp, 1985; Waters et al., 2009). Besides unconventional oil and gas reservoir, hydraulic fracturing stimulation technique is widely used in geothermal reservoir to enhance energy extraction (Brown, 2000), waste disposal (Abou-Sayed et al., 2007), mining (Jeffrey & Mills, 2000), and CO_2 sequestration (Huerta et al., 2020; Johnson & Morris, 2009).

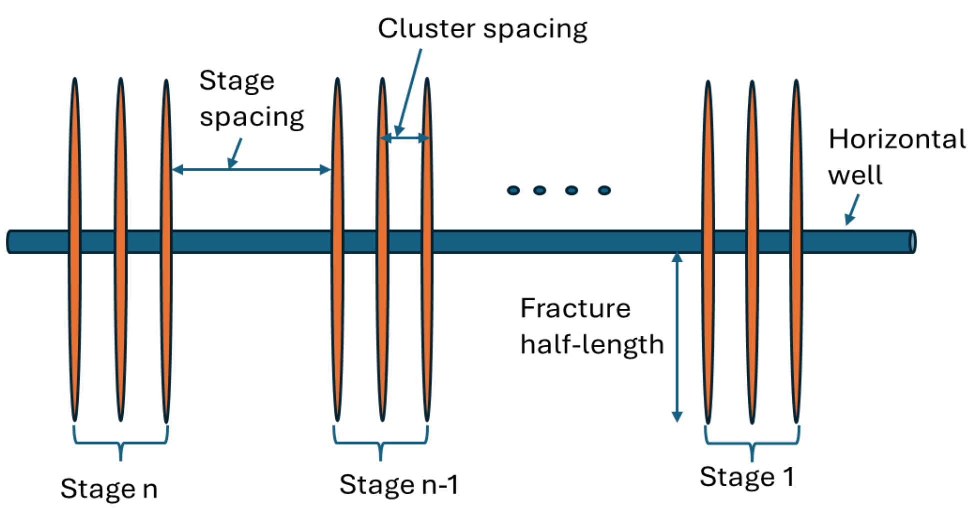

Figure 1-1.1: Schematic of multistage and multi-cluster fracture propagation.

Hydraulic fracturing by water injections is extensively used to stimulate unconventional gas and geothermal reservoirs. Numerous hydraulic fracturing models exist to simulate the fracture in 2D and 3D conditions. The process of fracture propagation can be conceptualized as an incremental lengthening process (Yew, 1997). At each time interval, the injection of pumping fluid into the fracture increases the net fluid pressure, fracture width, and stress intensity factor (SIF), leading up to propagation. When the SIF at the fracture tip reaches a critical threshold, corresponding to the material's resistance to propagation, the fracture front advances by a certain distance. The energy requirements for hydraulic fracture propagation depends on the regime in which it occurs (J. Adachi et al., 2007; Detournay, 2004; Spence & Turcotte, 1985). The P3D (pseudo-3D) model is an advanced hydraulic fracturing model developed to address the limitations of earlier 2D models like KGD and PKN. These models were used to describe the growth of vertical fractures in terms of length and apertures. According to these models, fracture will grow vertically until it reaches the higher stress bounded surface (Perkins & Kern, n.d.). The fracturing fluid applies pressure on the fracture surface, pushing it to open and extension. At the same time, high stresses in the upper and lower regions of the fracture seek to restrict it to extend beyond the pay zone. Therefore, fractures will propagate along their length. However, P3D models introduce a criterion for fracture height growth based on the concept that hydraulic fractures are constrained by the higher stresses in the layers above and below the pay zone (Simonson Member et al., 1978; Teufel & Clark, 1984; Warpinski et al., 1982). In these models, the analytical solution for fracture height growth is derived under the assumption that the stress intensity factor at the fracture tips in the vertical plane remains in balance with the rock's fracture toughness. However, the equilibrium fracture height growth models assume that the hydraulic fracture has a minimum height equal to the thickness of the pay zone by default and can only offer the excess development of fracture height into the higher stress layers above and below the pay zone.

This thesis is organized as follows. Chapter 1 introduces the theoretical development of the model, establishing the foundation for subsequent analysis. Chapter 2 presents numerical simulation examples, including verification to ensure the model's reliability. Chapter 3 discusses laboratory experiments on proppant strength measurement, highlighting practical applications and insights. Finally, Chapter 4 concludes the thesis, summarizing key findings and their implications for future research and industry practices.

Chapter 1 Theoretical Development of Model

1.1 Fracture aperture profile:

To investigate the influence of elastic anisotropy on hydraulic fracture propagation and height growth, Sesetty and Ghassemi introduced a Pseudo-3D (P3D) model designed for orthotropic rock formations considering both single and multiple fractures. For the case of multiple propagation, 2D DDM with height correction factor G (derived by Sessety) was employed to simulate the interaction between fractures. Consider a fracture in an infinite rock domain subjected to far-field principal stresses that are aligned with the global X-Y-Z (Figure 1.1). The axes of elastic symmetry of the rock (1-2-3) are parallel to the global coordinates X-Y-Z axes. When all points within the XY plane (A plane perpendicular to Z axis) demonstrate uniform elastic characteristics along the x-axis, we designate the x-axis as an axis of elastic symmetry. In the scenario where materials exhibit two axes of elastic symmetry, the plane defined by these two axes is termed the plane of elastic symmetry. The perpendicular direction to this plane of elastic symmetry is denoted as the principal direction of elastic symmetry. The fracture is subjected to lateral far-field in-situ compressive stress of magnitude σ in the X-direction applied over a thickness H (pay zone) as indicated in (Figure 1.1). The pay zone is symmetrically enclosed by two higher-stress regions that extend infinitely. Within these higher stress zones, the far-field stress magnitude in the X-direction is $\sigma+\sigma_b$. Additionally, in this work the vertical principal stress always aligns parallel to the Z-axis. Considering a symmetrical fracture labeled as ‘f’ that can also propagate into the higher stress zones, with a total height ‘h’ much smaller than its length L, so that it would be appropriate to utilize the plane strain condition within the X-Z plane. Similarly, when H >> L, the plane XY is in a state of plane strain, and physical quantities are independent of the Z direction. However, in reality, fractures have a finite height so that their stress effects cannot be neglected.

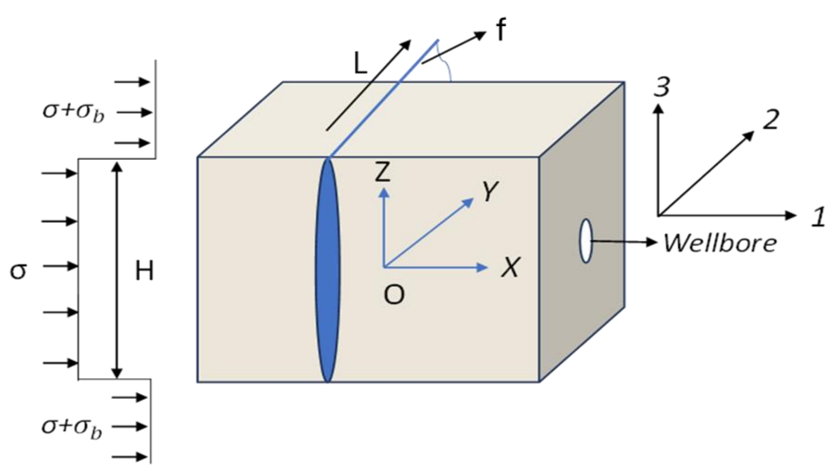

Figure 1.1: Illustrative figure of a fracture of length L and height H, where L/H>>1 propagated along global Y-axis from a horizontal well. The three axes of elastic symmetry 1-2-3

coincide with the three far-field principal stress directions also, the global coordinate axes X-Z-Y.

Choosing the origin 'O' as the center of the pay zone H (shown in Figure 1.1), fracture aperture profile along the fracture height for isotropic rock is (J. I. Adachi et al., 2010).

$$w(z) = \frac{1}{E'}(p - \sigma_b)\sqrt{h^2 - 4z^2} + \frac{2\sigma_b}{E'\pi}\left\{\sqrt{h^2 - 4z^2}\, arcsin\left(\frac{H}{h}\right) - 2z\, ln\left|\frac{H\sqrt{h^2-4z^2}+2z\sqrt{h^2-H^2}}{H\sqrt{h^2-4z^2}-2z\sqrt{h^2-H^2}}\right| + \frac{H}{2}\, ln\left|\frac{\sqrt{h^2-4z^2}+\sqrt{h^2-H^2}}{\sqrt{h^2-4z^2}-\sqrt{h^2-H^2}}\right|\right\} \quad (1.1)$$

For anisotropic rock (Sesetty & Ghassemi, 2018),

$$w(z) = \frac{b_{11}\Delta_0}{2\Delta_1}(p - \sigma_b)\sqrt{h^2 - 4z^2} + \frac{b_{11}\Delta_0\sigma_b}{\Delta_1\pi}\left\{\sqrt{h^2 - 4z^2}\, arcsin\left(\frac{H}{h}\right) - 2z\, ln\left|\frac{H\sqrt{h^2-4z^2}+2z\sqrt{h^2-H^2}}{H\sqrt{h^2-4z^2}-2z\sqrt{h^2-H^2}}\right| + \frac{H}{2}\, ln\left|\frac{\sqrt{h^2-4z^2}+\sqrt{h^2-H^2}}{\sqrt{h^2-4z^2}-\sqrt{h^2-H^2}}\right|\right\} \quad (1.2)$$

This equation can be used to calculate the fracture aperture profile in the X-Z plane. Where z is measured from the center 'O' along the Z-axis, p is the net pressure ($p_f - \sigma$). Where p_f is the fluid pressure and σ is the in-situ normal stress on the fracture. Appendix-A provides the definition of material constants $b_{11}, \Delta_0, \Delta_1$. The detail derivation of this aperture profile can be found in (Sesetty, V. (2018)).

1.2 Height growth of the fracture:

The equilibrium fracture height growth model assumes that changes in fluid pressure along the fracture height are negligible. This signifies the absence of viscous dissipation in the vertical direction of the fracture, resulting in the complete control of fracture growth by fracture toughness. This assumption is valid when the fracture height growth is much smaller than the lateral growth of fracture so that pressure losses remain small in the z-direction. Therefore, when the pay zone is bounded by two higher stress barriers which can restrict the vertical growth of fracture, this model can be applicable. Assuming plane strain condition in the plane X-Z, the mode-1 stress intensity factor due to distributed net pressure p(z) along the entire fracture height h is given as ((Barnett & Asaro, 1972; Simonson Member et al., n.d.),

$$\boldsymbol{K_I = \frac{1}{\sqrt{a\pi}}\int_{-\frac{h}{2}}^{\frac{h}{2}}\sqrt{\frac{a+z}{a-z}}\, p(z)dz} \quad (1.3)$$

The bounding conditions for the net pressure p(z) are:

$$p(z) = \begin{pmatrix} p - \sigma_b, \frac{H}{2} \leq z \leq \frac{h}{2} \\ p, \quad -\frac{H}{2} \leq z \leq \frac{H}{2} \\ p - \sigma_b, \quad -\frac{H}{2} \leq z \leq \frac{h}{2} \end{pmatrix} \tag{1.4}$$

As previously stated, fracture height growth is considered to occur in a toughness-dominated regime, therefore the mode-1 stress intensity factor (K_I) at fracture tips in the plane X-Z is always in equilibrium with the rock's fracture toughness (K_{IC}). For a symmetrical fracture 'f' bounded by high stress, using bounding conditions given in equation (**1.4**) and performing piece wise integration of equation (**1.3**) gives:

$$2 \arcsin\left(\frac{H}{h}\right) - \left(1 - \frac{p}{\sigma_b}\right)\pi = \sqrt{\frac{2\pi}{H}}\frac{K_{IC}}{\sigma_b}\sqrt{\frac{H}{h}} \tag{1.5}$$

The above equation can be used to evaluate fracture height h, when the net pressure p inside the fracture is known, and other parameters such as pay zone thickness H, fracture toughness K_{IC} and excess stress in bounding layers σ_b is already given. Once the toughness convergence is achieved (criteria is given in Eq-1.6), we know the net pressure inside the fracture along its length, then we use Equation-(**1.5**). As the fracture height in equation (**1.5**) appears twice and one is inside the arcsin function, it is solved iteratively.

1.3 2D Displacement Discontinuity Method (DDM) with Height Correction Factor:

The displacement discontinuity method is a boundary element approach that relies on the analytical solution for a constant displacement discontinuity across a finite segment in an infinite or semi-infinite domain. This method addresses the problem by distributing multiple displacement discontinuity segments along a boundary where either displacement or stress is specified. The fracture is discretized into N straight-line segments, each assuming a constant displacement discontinuity across its length. Consider the portion of the x-axis where $|x| \leq 2a$ and y=0 to be line fractures. The two surfaces of the crack are y=0+, which is on the positive side of the y=0 line, and y=0-, which is on the negative side. Displacement discontinuity D_i is defined as the difference between the displacements of two surfaces.

$$D_i = u_i(x_1, 0_-) - u_i(x_1, 0_+) \tag{1.6}$$

Displacement in the x and y directions are:

$$\boldsymbol{D_x = u_x(x_1, 0_-) - u_x(x_1, 0_+)}$$
$$\boldsymbol{D_y = u_y(x_1, 0_-) - u_y(x_1, 0_+)} \tag{1.7}$$

Where u_x and u_y are positive in the positive x-axis and y-axis. D_x is positive if the upper surface moves to the left relative to the lower surface, and D_y is positive if the two surfaces move toward one another.

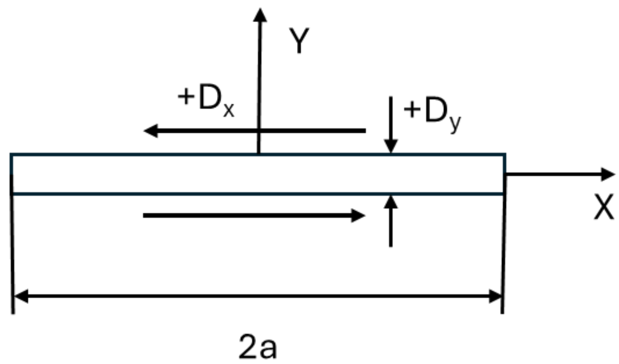

Figure 1.2: Displacement discontinuity components D_x and D_y along the x and y-axis.

The displacement and stress components resulting from a unit displacement discontinuity (DD) on an element of length 2a are described by the corresponding solution (Crouch et al., 1983).

$$\boldsymbol{u_x = D_x[2(1-\vartheta)f_{,y} - yf_{,xx}] + D_y[-(1-2\vartheta)f_{,x} - yf_{,xy}]}$$
$$\boldsymbol{u_y = D_x[(1-2\vartheta)f_{,x} - yf_{,xy}] + D_y[2(1-\vartheta)f_{,y} - yf_{,xx}]} \tag{1.8}$$

And

$$\boldsymbol{\sigma_{xx} = 2GD_x[2f_{,xy} + yf_{,xyy}] + 2GD_y[f_{,yy} + yf_{,yyy}]}$$
$$\boldsymbol{\sigma_{yy} = 2GD_x[-yf_{,xyy}] + 2GD_y[f_{,yy} - yf_{,yyy}]}$$
$$\boldsymbol{\sigma_{xy} = 2GD_x[2f_{,yy} + yf_{,yyy}] + 2GD_y[-yf_{,xyy}]} \tag{1.9}$$

The function $f(x, y)$ in these equations is,

$$f(x,y) = \frac{-1}{4\pi(1-\vartheta)}\left[y\left(\arctan\frac{y}{x-a} - \arctan\frac{y}{x+a}\right) - (x-a)ln\sqrt{[(x-a)^2 + y^2]} + (x+a)ln\sqrt{[(x+a)^2 + y^2]}\right]$$

To apply the displacement discontinuity method to a problem with a curved fracture, the crack is divided into *N* straight-line segments, and displacements are calculated at various points along the curve. Each of these segments represents a discrete displacement discontinuity serving as a boundary element. The illustration below demonstrates the process of discretizing a continuous curve into *N* elements. The displacement component of each element is represented by its local coordinate system s and n, as depicted in Fig. 4 The components of displacement discontinuity in j[th] element with respect to the local coordinate system s and n can be represented as,

$$\boldsymbol{D_s^j = u_s^{j-} - u_s^{j+}}$$
$$\boldsymbol{D_n^j = u_n^{j-} - u_n^{j+}} \quad (1.10)$$

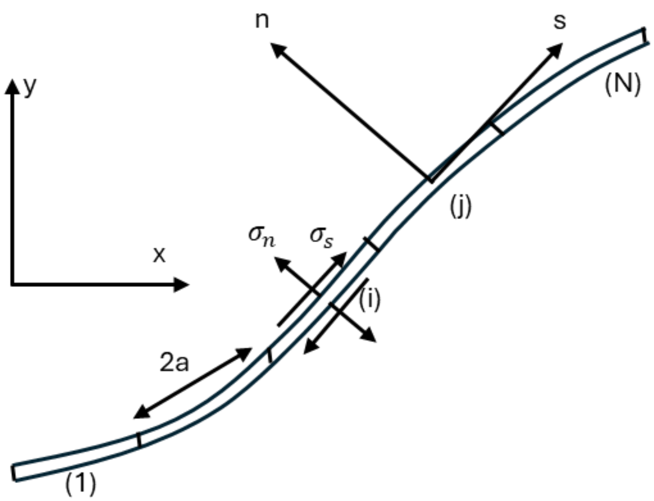

Figure 1.3: Discretization of a curved crack into N elements with each elements having its own local coordinate system, and a global coordinate system x-y (Crouch et al., 1983).

By taking account the effect of displacement discontinuity of one element on the displacement discontinuity and induced stresses at another element, the shear and normal stresses at the midpoint of an element that is caused by a displacement discontinuity of another element can be expressed as follows:

$$\boldsymbol{\sigma_s^i = A^{ij}{}_{ss} D_s^j + A^{ij}{}_{sn} D_s^j} \quad (1.11)$$

$$\boldsymbol{\sigma_n^i = A^{ij}{}_{nn} D_n^j + A^{ij}{}_{ns} D_n^j}$$

Where A^{ij} is the influence coefficient for the stresses, and σ_n and σ_s are the normal and shear stresses at the i[th] element due to displacement discontinuity in j[th] element. Stresses at the midpoint of i[th] element considering the displacement in all N elements can be written as:

$$\boldsymbol{\sigma_s^i = \sum_{j=1}^{N} A^{ij}{}_{ss} D_s^j + \sum_{j=1}^{N} A^{ij}{}_{sn} D_n^j} \quad (1.12)$$
$$\boldsymbol{\sigma_n^i = \sum_{j=1}^{N} A^{ij}{}_{ns} D_s^j + \sum_{j=1}^{N} A^{ij}{}_{nn} D_n^j}$$

When employing 2D plane strain numerical methods like 2D DDM to model the evolution of fracture length and aperture, there is a risk of obtaining inaccurate values for fracture aperture, length, and stress distribution around the fractures. This inaccuracy arises because the standard approach implicitly assumes an infinite fracture height to reduce the problem to plane strain, which is not realistic. To address this issue, a partial solution is to introduce the "3D correction factor," denoted as G, as proposed by Olson in 2004. This correction factor considers the effect of the finite fracture height (h) when using plane strain DDM for isotropic rock. Then the fracture is discretized into N number of elements along its length, the normal and shear stresses at the center of each element can be represented as:

$$\boldsymbol{\sigma_s^i = \sum_{j=1}^{N} G^{ij} A^{ij}{}_{ss} D_s^j + \sum_{j=1}^{N} G^{ij} A^{ij}{}_{sn} D_n^j} \tag{1.13}$$

$$\boldsymbol{\sigma_n^i = \sum_{j=1}^{N} G^{ij} A^{ij}{}_{ns} D_s^j + \sum_{j=1}^{N} G^{ij} A^{ij}{}_{nn} D_n^j}$$

Where the influence coefficients $A^{ij}{}_{ss}$, etc., gives normal/shear stress at element i (i=1, N) due to a unit normal/shear displacement discontinuity at element j (Crouch et al., 1983).

The 3D correction factor G^{ij} for isotropic (Olson, 2004) and anisotropic body (Sesetty et al., 2018a; Sesetty & Ghassemi, 2018) respectively is given as:

$$\boldsymbol{G^{ij} = 1 - \frac{d_{ij}^{\beta}}{\left[d_{ij}^2 + \left(\frac{h}{\alpha}\right)^2\right]^{\frac{\beta}{2}}}} \tag{1.14}$$

$$\boldsymbol{G^{ij} = 2\,Real\left[\frac{P\mu_2}{2(\mu_1 - \mu_2)}\left(\frac{(\mu_1 d_{ij})^{\beta}}{\sqrt{(\mu_1 X)^2 - \left(\frac{H}{\alpha}\right)^2}} - 1\right) + \frac{P\mu_1}{2(\mu_2 - \mu_1)}\left(\frac{(\mu_2 d_{ij})^{\beta}}{\sqrt{(\mu_2 X)^2 - \left(\frac{H}{\alpha}\right)^2}} - 1\right)\right]}$$

where d_{ij} is the distance between elements i, j, and h is the fracture height of that element. The constant α and β are empirically derived which take the values 1.0 and 2.3 respectively.

1.4 3D DDM Formulation:

An analytical solution of 3D DDM for elements with constant displacement discontinuities was documented by (Crouch et al., 1983; Shou, 1993). This method is derived from the analytical solution for a constant displacement discontinuity over a finite rectangular element. Figure 1.4 shows a 3D crack discretized into small rectangular elements, within an element DD will be considered constant. A 3D fracture is discretized as an assembly of rectangular elements (Figure 1.4), where $x1$, $x2$, $x3$ represent the local coordinate system of each displacement discontinuity element, in which $x3$ oriented perpendicular to the element's plane. Each element has a positive (x3 = 0+) side and a negative (x3 = 0-) side.

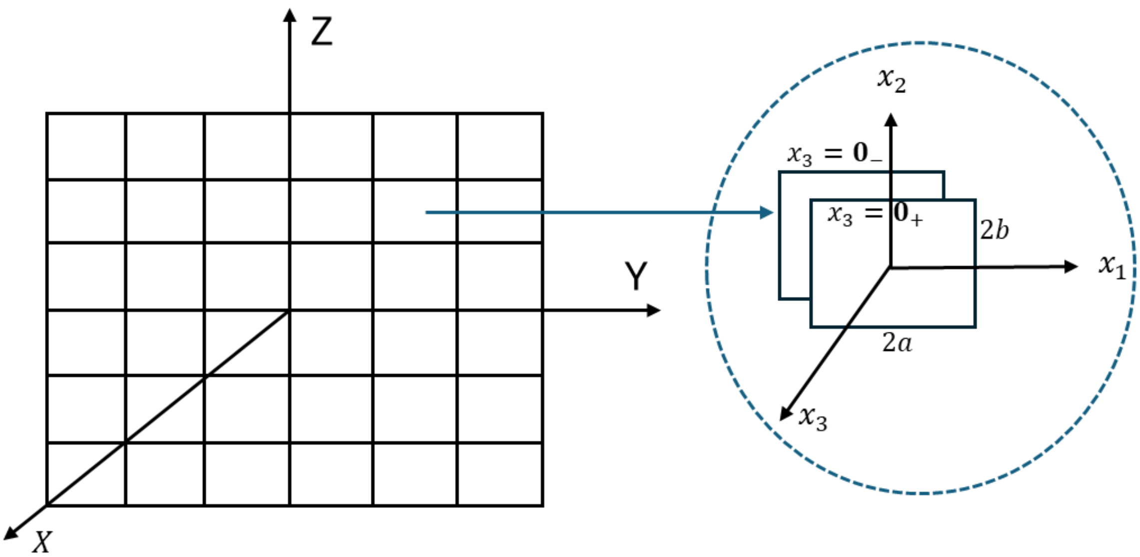

Figure 1.4: A 3D crack discretized into rectangular elements where 2a and 2b are the length and height of elements. X-Y-Z is the global coordinate system and $\boldsymbol{x_1, x_2, x_3}$ are the axis of local coordinate system.

$$\begin{aligned} \boldsymbol{D_1(x_1, x_2, 0) = u_1(x_1, x_2, 0_-) - u_1(x_1, x_2, 0_+)} \\ \boldsymbol{D_2(x_1, x_2, 0) = u_2(x_1, x_2, 0_-) - u_2(x_1, x_2, 0_+)} \\ \boldsymbol{D_3(x_1, x_2, 0) = u_3(x_1, x_2, 0_-) - u_3(x_1, x_2, 0_+)} \end{aligned} \tag{1.15}$$

The detailed derivation 3D DDM are given in (Crouch et al., 1983). In this work, as we neglected the shear DD, the normal stress induced on a crack element can be written by,

$$\boldsymbol{\sigma_n^i = \sum_{j=1}^{N} A^{ij}{}_{nn} D_n^j} \tag{1.16}$$

Where $A^{ij}{}_{nn}$ are the boundary influence coefficients for stresses, and defined as

$$A^{ij}{}_{nn} = A^{ij}{}_{333} = \frac{G}{4\pi(1-\vartheta)}\left[(1-2\vartheta)sin^2\gamma\, I_{,22} + I_{,33} - x_3\left(sin^2\gamma\, I_{,311} + cos^2\gamma\, I_{,333} - sin2\gamma\, I_{,313}\right)\right]$$

Where $\gamma = \beta^i - \beta^j$, And $I_{,k}, I_{,kl}, I_{,klm}$ are first, second and third order derivatives of $I(x_1, x_2, x_3)$ with respect to coordinate x_k, x_l, x_m respectively. $I(x_1, x_2, x_3)$ is kernel analytical solution presented by (Crouch et al., 1983; Shou, 1993; Shou & Crouch, 1995) to the problem with a constant displacement discontinuity D_i over a randomly oriented rectangular element in an infinite elastic domain solved by employing the Green's function approach,

$$I(x_1, x_2, x_3) = \int_{-b}^{b}\int_{a}^{a} \frac{1}{\sqrt{(x_1-\xi_1)^2 + (x_2-\xi_2)^2 + {x_3}^2}} d\xi_1 d\xi_2$$

1.5 Fluid flow equation:

The flow of fluid within a fracture is modeled by treating the fractures as parallel plates. The continuity equation inside the fracture for fluid flow can be written as, (Batchelor & Young, 1968; Nordgren, 1972)

$$\frac{\partial \overline{w}}{\partial t} + \frac{\partial \overline{q}}{\partial y} + \frac{C'}{\sqrt{t - t_0(y)}} = \frac{Q_0}{H} \qquad (1.17)$$

Here $C' = 2C_L$ is Carter's leak-off coefficient, Q_0 is the fluid injection rate, $t_0(y)$ is the time when fluid at this y point, $\bar{q}$ is the average flux, and $\bar{w}$ is the width of the element.

$$\overline{q} = -\frac{1}{12\mu H}\frac{\partial p}{\partial y}\int_{-\frac{h}{2}}^{\frac{h}{2}} w(z,y)^3 dz \qquad (1.18)$$

$$\overline{w} = \frac{1}{H}\int_{-\frac{h}{2}}^{\frac{h}{2}} w(z,y) dz$$

Incorporation of a flow distribution equation for each individual perforation cluster is essential within the interrelated set of equations governing coupled fracture deformation and fluid flow. Disregarding the effects of wellbore friction, the calculation of pressure drops resulting from friction in perforations is determined using Equation (1.19) (Elbel et al., 1992). The perforation friction equation (Eq. (1.19)) requires the flowrates in each cluster to calculate the pressure loss dure perforation friction. And, as the perforation friction happens only in the central elements where fluid is injected, pressure drop only added for the central elements at each cluster. However, the flow rate into each cluster is also dependent on the pressure drop due to the perforation friction, to mitigate this issue, pressure drop is considered in the P-W coupling iteration process.

$$P_{perf} = \frac{0.237\,\rho {q_i}^2}{n^2 D^4 C^2} \tag{1.19}$$

$$\sum_{i}^{N} q_i = Q \tag{1.20}$$

Where n is the number of perforations per cluster, D is the perforation diameter, C is perforation discharge coefficient, ρ is fluid density.

1.6 Fracture propagation regime:

Hydraulic fracturing refers to the process of creating and expanding fractures in rocks by injecting fluid at high pressure. During fracture propagation, when the energy dissipated due to fluid flow within the fracture is minimal compared to the energy required to create a new rock surface, the fracture propagation is said to be in a toughness-dominated regime. Conversely, if the energy required to create a new rock surface is negligible relative to the energy lost to viscous dissipation from fluid flow within the fracture, then the propagation occurs in a viscous-dominated regime. Early studies by (Barenblatt, 1962), (Spence & Sharp, 1985), (Spence & Turcotte, 1985), (Lister, 1990), and (Desroches et al., 1994) mentioned that the shape of a fracture tip in rock differs when fracture toughness is zero compared to cases where fracture toughness is non-zero. The solution procedure for toughness dominated regime and viscous dominated regimes are different, so two separate solution procedures are used.

1.7 R3D for asymmetric stress barrier:

In the previous scenario, the model assumed symmetrical bounding stress above and below the pay zone, implying an equal excess stress distribution in both regions. The current model, however, is designed to simulate hydraulic fracture propagation under conditions where stress barriers are asymmetrical. With the equilibrium-height assumption (fluid flow in vertical direction is assumed zero), the fracture cross-sectional shape can be expressed as a function of the net pressure. Simonson et al. (1978) provided a solution for a scenario in the case of a symmetric three-layer system (Simonson et al., 1978). (Fung et al., 1987) derived a more general solution applicable to non-symmetric multilayer systems. There is not so much study that has been conducted on the fracture height growth in asymmetric stress barrier. (Kresse et al., 2011, 2017; Kresse & Weng, 2018) and (Dontsov & Peirce, 2017) have analyzed the effect of asymmetric stress barrier on fracture height growth. In a multilayered formation, the fracture height growth and width profile along height and length of a fracture depend on fluid pressure, the in-situ stress, fracture toughness, layer thickness, and elastic modulus of each layer covered by the fracture height (in this study we assumed elastic modulus is same in all layers). Figure 1.5 shows the schematic of fracture cross section in asymmetrical stress barriers.

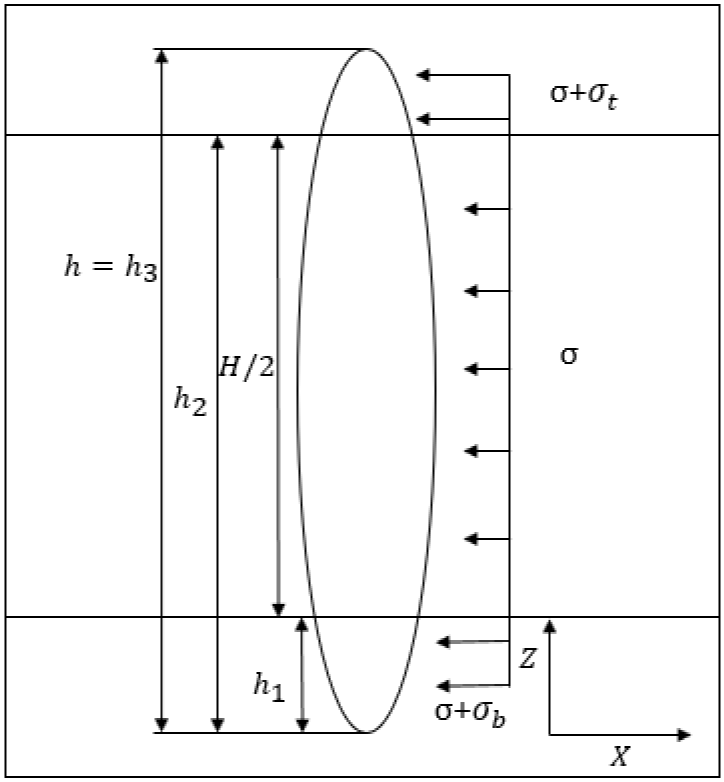

Figure 1.5: Schematic of fracture cross-section in asymmetrical stress barriers. Fracture propagates along Y-axis, a vertical cross-section perpendicular to Y-axis were shown in figure.

Following Fung et al. (1987) the stress intensity factors at the top tip and the bottom tip K_{Itop} and K_{Ibot}, respectively, can be written as function of the pressure at the center of the fracture and the closure stresses in the layers σ_i as

$$\boldsymbol{K_{Itop} = \sqrt{\frac{\pi h}{2}}\left(p_{cp} - \sigma_n + \rho_f g(h_{cp} - \frac{3h}{4}\right) + \sqrt{\frac{2}{\pi h}}\sum_{i=1}^{n-1}(\sigma_{i+1} - \sigma_i)\left[\frac{h}{2} arccos\left(\frac{h-2h_i}{h}\right) - \sqrt{h_i(h-h_i)}\right]} \quad (1.21)$$

$$\boldsymbol{K_{Ibot} = \sqrt{\frac{\pi h}{2}}\left(p_{cp} - \sigma_n + \rho_f g(h_{cp} - \frac{3h}{4}\right) + \sqrt{\frac{2}{\pi h}}\sum_{i=1}^{n-1}(\sigma_{i+1} - \sigma_i)\left[\frac{h}{2} arccos\left(\frac{h-2h_i}{h}\right) - \sqrt{h_i(h-h_i)}\right]}$$

Fracture aperture along the fracture height can calculated using the following equation

$$w(z) = \frac{4}{E'}\left[\left(p_{cp} - \sigma_n + \rho_f g(h_{cp} - z)\right)\right]\sqrt{z(h-z)} + \frac{4}{\pi E'}\sum_{i=1}^{n-1}(\sigma_{i+1} - \sigma_i)\left[(h_i - z)cosh^{-1}\frac{z\left(\frac{h-2h_i}{h}\right)+h_i}{|z-h_i|} + \sqrt{z(h-z)}arccos\left(\frac{h-2h_i}{h}\right)\right] \tag{1.22}$$

Where K_{Itop} and K_{Ibot} are the stress intensity factors at the upper lower tips, respectively. $w(z)$ is the fracture aperture at any point along the fracture height z, σ_n is the in-situ stress at the top tip, and σ_i is the in-situ stress at the i-th layer, h is the fracture height, h_i is the height of the top of the i-th layer from the bottom tip.

1.7.1 Solution procedure for asymmetric stress barrier:

The solution procedure is similar to the symmetrical stress barrier solution explained in previous sections. At the beginning of every timesteps, as the fluid pressure inside the fracture is unknown, equation ***(1.22)*** is used to calculate the average fluid pressure inside the fracture using $K_{Itop} = K_{Ibot} = K_{IC}$. Then using equation (***1.22***), average fracture aperture and aperture profile along the fracture for all elements were calculated. Fluid flow equation (**1.17**) were solved in an iterative process, and converged fracture aperture and pressure were found. Using the aperture at the tip element, stress intensity factor at the tip element were calculated. If the difference between SIF and fracture toughness is within the tolerance limit (5%), a new grid is added before going to the next timestep. If they were not satisfied, a new timestep was based on the difference between SIF and K_{IC}. Bisection method was used to accelerate the process. To calculate the height growth of the fracture in asymmetric stress barrier, we assume that fracture toughness in both layers above and below the pay zone is same as the K_{IC}. Discretize the fracture along its height and calculate the fracture aperture top and bottom tip. Using the top and bottom tip aperture SIF can be calculated. If SIF exceeds the K_{IC}, a new element was added along the vertical axis, again SIF is calculated, and the process repeated until SIF in both top and bottom layers lower than K_{IC}.

Chapter 2 Simulation Examples

2.1 P3D Model Validation:

Propagation of a single planar hydraulic fracture is considered using the P3D hydraulic fracture propagation model. The model uses the viscous regime propagation criteria to model fracture propagation. The result is compared with the result from the literature (Sesetty et al., 2018a). The input parameters employed for the validation of our model are presented in Table 2-1 for isotropic rock and Table 2-2 for anisotropic rock. These are the same input parameters that were used in literature (Sesetty et al., 2018b). a vertically transverse isotropic (VTI) rock, with a degree of anisotropy of 4, signifying the ratio of Young's moduli parallel and perpendicular to the bedding plane (E1/E3) used in this study to see the effect of rock anisotropy. The simulation scenarios involved the injection of slick water (with a viscosity of 1 cP) at a rate of 10 barrels per minute (bpm) for a duration of 300 seconds through a small perforation of 2 meters in length. The maximum and minimum horizontal stresses are specified as 40 MPa and 39 MPa, respectively, with symmetrical barriers above and below the pay zone experiencing an excess stress of 1.0 MPa. A pay zone thickness of 30m is employed across all simulation scenarios. Fluid compressibility is considered negligible at 1×10-9 psi^{-1}, with a fluid density of 8.33 lb/gal. The initial perforation diameter is 0.6 inches, and a perforation discharge coefficient of 0.9 is assumed. Notably, fluid leak-off is disregarded in accordance with the literature (Sesetty et al., 2018a).

Table 2-1: Input parameters used for P3D model for isotropic case.

E (GPa)	$\boldsymbol{\vartheta}$	$\boldsymbol{\mu}$ (cp)	H (m)	$\boldsymbol{Q_0}$ (bpm)	σ_b (MPa)	σ_{max} (MPa)	Kic (MPa.m$^{0.5}$)
40	0.15	1.0	30	10	1.0	40	1.5

Table 2-2: Input parameters used for P3D model for anisotropic case.

Ex (GPa)	Ez (GPa)	$\boldsymbol{\vartheta_{12}}$	$\boldsymbol{\vartheta_{13}}$	$\boldsymbol{G_{13}}$ (GPa)	σ_b (MPa)	Kic 1 (MPa.m$^{0.5}$)	Kic 2 (MPa.m$^{0.5}$)
40.0	10	0.15	0.185	7.45	1.0	1.5	1.5

Figure 2.1 and Figure 2.2 illustrates a comparison of fracture half-height along the half-length fracture between P3D viscous model and Sesetty's result for isotropic rock and anisotropic rock, respectively. The findings reveal that anisotropic rocks exhibit higher fracture aperture compared to isotropic ones. However, the isotropic model predicts greater height growth into the bounding layers in contrast to the anisotropic model. This discrepancy arises due to the lower net injection pressures observed during fracture propagation in anisotropic rock (shown in

Figure 2.3). Since fracture height growth correlates directly with the net pressure within the fracture, as per Equation (**1.5**), the lower net pressure in anisotropic rock leads to reduced height growth compared to the isotropic scenario. Notably, no significant difference in fracture lengths is noticed between isotropic and anisotropic rocks. In summary, these findings underscore that simplifying a VTI (Vertical Transverse Isotropic) rock as isotropic will result in underestimated fracture apertures and overestimated fracture height, thus highlighting the importance of considering rock anisotropy for accurate modeling. The comparison demonstrates that our model accurately predicts fracture propagation. A minor discrepancy is observed in the fracture dimensions (length and height) between our model and Sesetty's results. Specifically, our model predicts a slightly greater fracture height compared to Sesetty's, which consequently results in a slightly shorter fracture length. These differences are minimal and validate the accuracy of our model, as the overall results are closely aligned with Sesetty's findings.

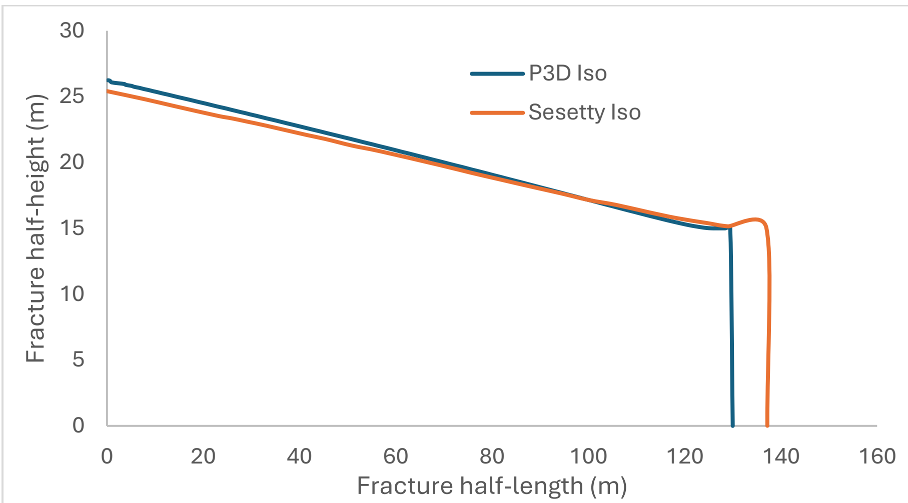

Figure 2.1: Comparison of fracture half-height along the half-length of the fracture between P3D viscous model and Sesetty's result for isotropic rock.

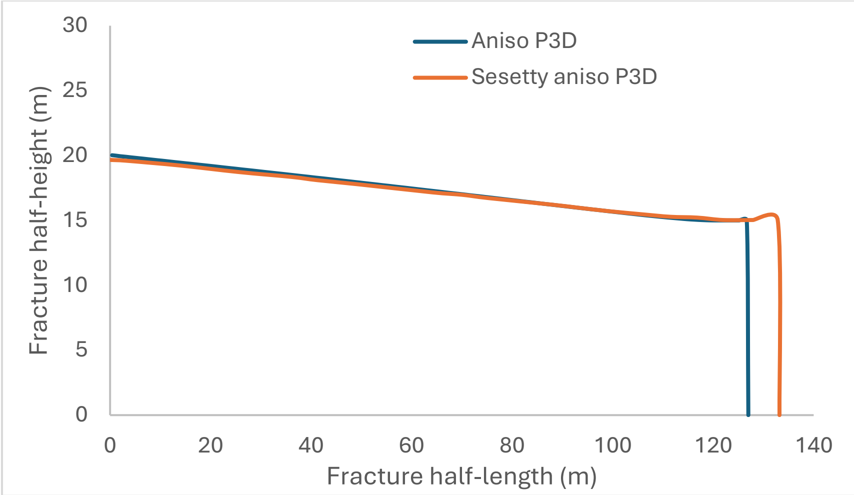

Figure 2.2: Comparison of fracture half-height along the half-length of the fracture between P3D viscous model and Sesetty's result for anisotropic rock.

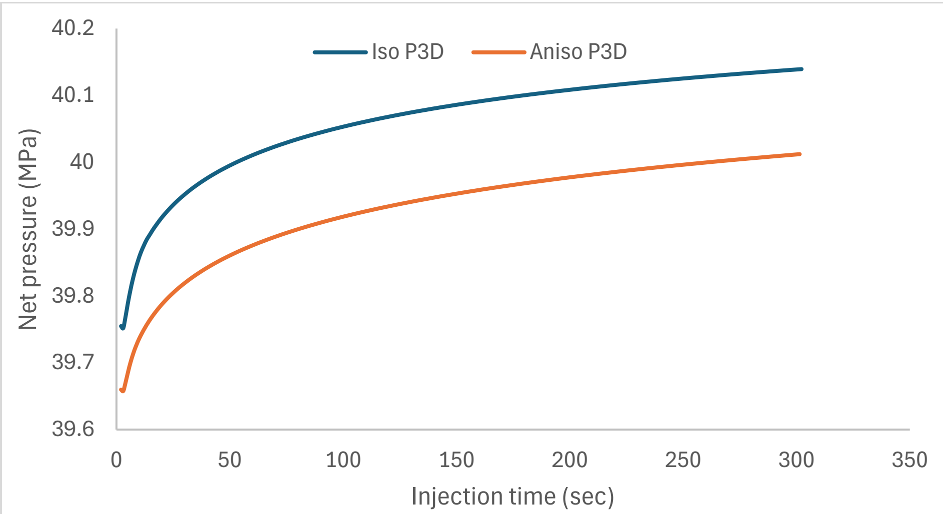

Figure 2.3: Comparison of net injection pressure between isotropic and anisotropic rock.

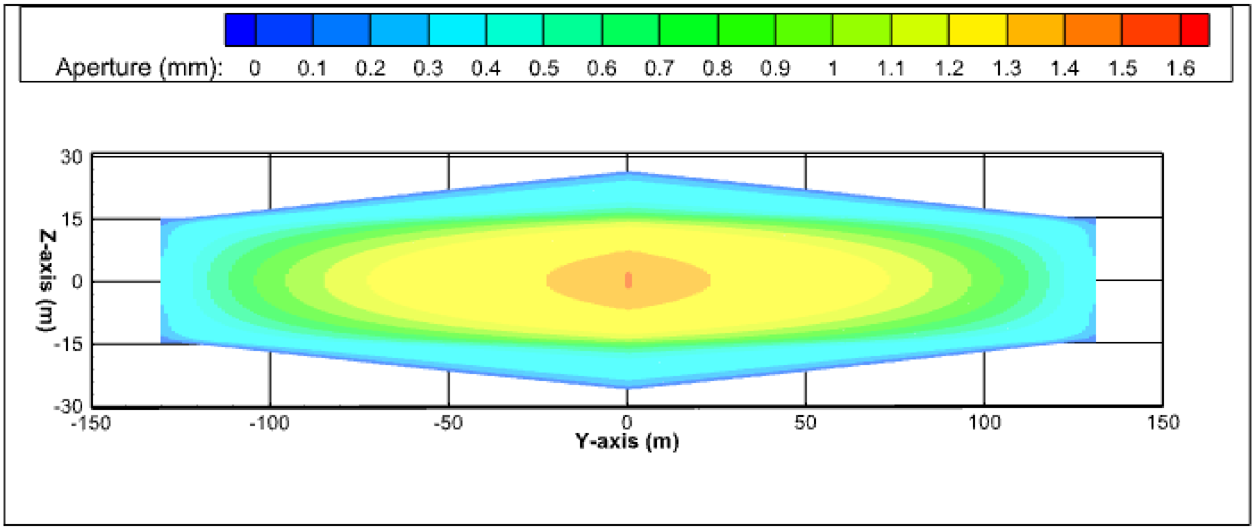

Figure 2.4: Contour map of fracture aperture distribution using P3D viscous model after 5 minutes injection in isotropic formation.

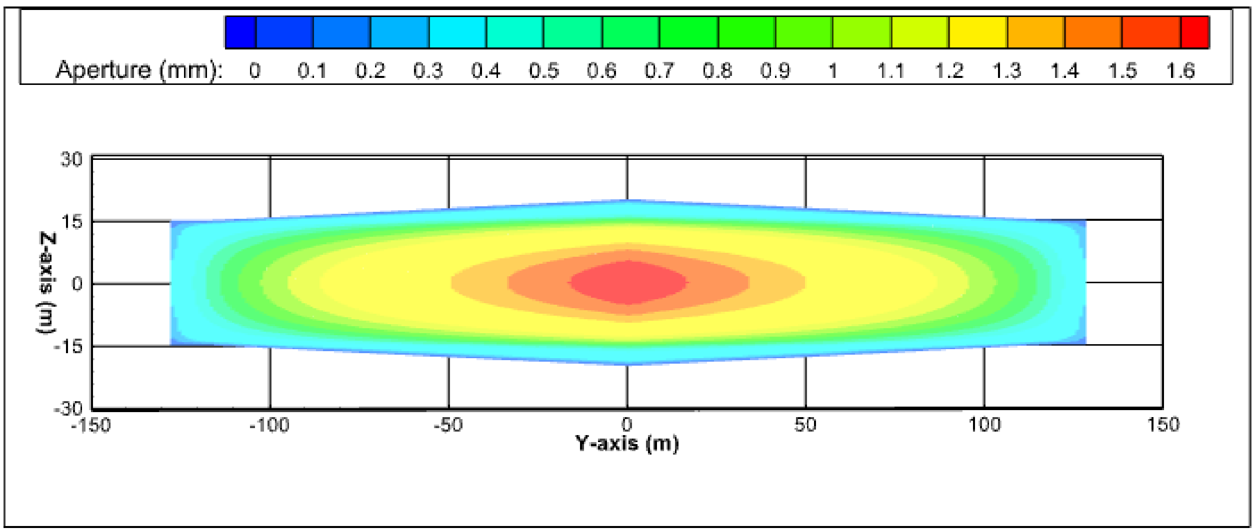

Figure 2.5: Contour map of fracture aperture distribution using P3D viscous model after 5 minutes injection in anisotropic formation.

2.2 P3D multi-cluster fracture propagation:

To simulate simultaneous propagation of hydraulic fractures from multiple perforation clusters using P3D model, at the end of every time step, stress shadow between the fractures need to calculate. 2D DDM were employed to evaluate the induced stress on one fracture due displacement discontinuity on other fractures. Induced stress was calculated at the center of the pay zone and stress barriers were assumed to be the same as the initial conditions. In the next timestep, these induced normal stresses are added to far-field stress. This way of externally calculating induced stresses using a 2D DDM after every timestep mimics the interaction between multiple fractures.

In this example, we propagate 5 clusters simultaneously with each cluster separated by 20 m. To stimulate the fractures, slick water with a viscosity of 4 cp was injected at a rate of 50 bpm for a duration of 300 seconds in each fracturing stage. The rock properties assumed anisotropic, and the rock properties are same as given in Table 2-2. Additionally, symmetrical barriers located above and below the pay zone experienced an excess stress of 4 megapascals (MPa). This high stress barrier was chosen intentionally to compare the result with P3D multi-cluster result from (Sesetty et al., 2018). No perforation friction was considered in this case. Negligible leak-off, referring to the no fluid loss into the surrounding formation, was considered in these simulations. The number of perforations per cluster is taken as 50, this high number was taken intentionally to make the effect of perforation in flow partition among all clusters negligible. So that the flow partition into each cluster is completely determined from the stress shadow effect. These examples take all the input parameters same as the literature (Sesetty et al., 2018a) to verify the multi cluster model.

Table 2-3: Fracture properties and perforation data.

Perforation diameter (inch)	0.6
Perforation discharge coefficient	0.9
Number of parallel wells	1
Number of perforations per cluster	50
Number of stages per well	1
number of clusters per stage	5
cluster spacing (m)	20

Figure 1.19 shows the contour map of fracture geometry after 300 seconds injection of fluid with viscosity 1 cp at 50 bpm flow rate. From the figure, in multi-cluster fracture system, stress shadow plays a very important role in fracture propagation. As the outer fracture experiences less, induced stress compared to the inner fracture, the fracture aperture at the outer fracture is higher than the fracture aperture in inner fracture. The magnitude of stress shadow effects is influenced by the displacement discontinuity (DD) and the spacing between fractures. Fractures situated closer to the outer fracture encounter stronger stress shadow effects, as the DD in the outer fracture is significantly greater. Consequently, the second and fourth clusters are observed to completely close after several timesteps due to the stress shadow.

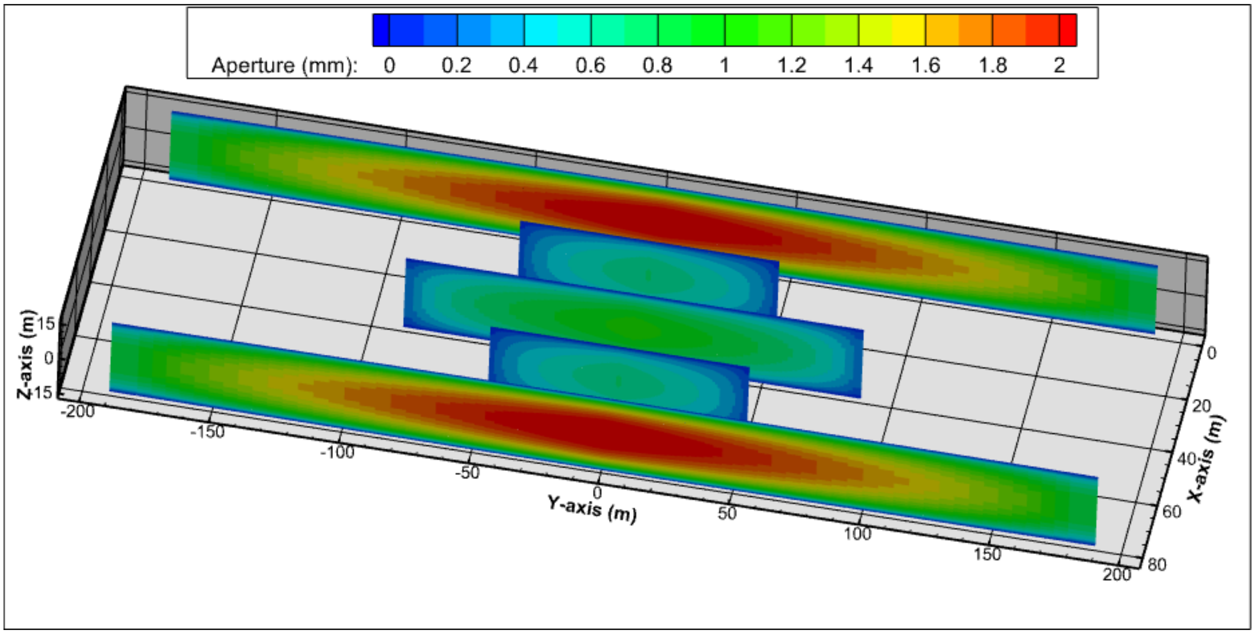

Figure 2.6: Fracture aperture distribution obtained from multi-cluster fracture propagation using P3D viscous fracture propagation model for anisotropic rock with symmetric stress barriers of 4.0 MPa.

2.3 Multi-stage and Multi-well Fracture Propagation:

In this study, fracture propagation is simulated sequentially from two parallel horizontal wells, each consisting of two fracturing stages with five clusters per stage. For the initial stage in each well, in-situ stress conditions are applied directly, as no prior fracturing has altered the natural stress field. However, for the subsequent stage, the induced stress from the initial fracturing must be incorporated to accurately model stress changes. To account for this induced stress, we apply a 60% fracture aperture to estimate the stress influence using the 2D Displacement Discontinuity Method (DDM) along with a height correction factor G. This approach captures stress perturbations from the first stage, thereby refining the conditions for fracture propagation in the second stage. The fracture propagation across the two wells follows a zipper pattern, an arrangement designed to optimize stimulation efficiency by allowing controlled interaction between fractures from adjacent wells. One example of multi wells and multistage fracture propagation is given below.

2.3.1 Effect of the number of perforations per cluster:

The growth of hydraulic fractures is greatly influenced by the number of perforations per cluster. To thoroughly analyze this effect, a numerical simulation was conducted on two hydraulic fracture scenarios, each with a different number of perforations. The simulation aimed to replicate the multi-stage hydraulic fracturing process in two parallel wells. The fracturing process consisted of two stages in each well, and each stage comprised five perforation clusters with one facture in each cluster. Along the lateral length, each stage spanned 160 m with a spacing of 40 m between the perforation clusters. The stage spacing, which refers to the distance between the outermost fractures of subsequent stages, was also set to 40 m. In the first case, 50 perforations were considered per cluster, while the second case had 10 perforations per cluster. To stimulate the fractures, slick water with a viscosity of 1 cp was injected at a rate of 80 barrels per minute (bpm) for a duration of 300 seconds in each fracturing stage. The rock properties assumed in both cases were isotropic, featuring an elastic modulus of 40 GPa and a Poisson's ratio of 0.15. Additionally, symmetrical barriers located above and below the pay zone experienced an excess stress of 1.5 megapascals (MPa). No perforation friction was considered in this case. Negligible leak-off, referring to the no fluid loss into the surrounding formation, was considered in these simulations. The other input parameters were given in Table 2-4 and

Table 2-5.

Table 2-4: Input parameter of isotropic rock used for P3D model.

E (GPa)	$\boldsymbol{\vartheta}$	$\boldsymbol{\mu}$ (cp)	H (m)	$\boldsymbol{Q_0}$ (bpm)	σ_b (MPa)	σ (MPa)	Kic (MPa.m$^{0.5}$)
40	0.15	1.0	33	80	1.5	39	1.5×10^{6}

Table 2-5: Fracture geometry and perforation data.

Perforation diameter (inch)	0.6
Perforation discharge coefficient	0.9
Number of parallel wells	2
spacing between the wells (m)	300
number of stages per well	2
number of clusters per stage	5
cluster spacing (m)	40
stage spacing (m)	40
offset between the fractures of parallel wells (m)	20

Figure 2.7 and Figure 2.8 illustrate a comparison net pressure at the center of fracture and fracture half-height along fracture half-length, respectively between the cases with 50 and 10 perforations per cluster. The breakdown pressure of the specimen or rock reduced with the increase of density of perforation (Ali Daneshy & Services, n.d.). So, with the increase of number of perforations per cluster, the fracture will propagate with lower pressure and faster. The results show that the growth of fractures is relatively higher in the case with a larger number of

perforations. Since the fluid injection rate remains constant, the pressure at the wellbore is higher when there are fewer perforations compared to the case with more perforations. As a result, the fracture height, length, and aperture exhibit greater growth over time in the scenario with a higher number of perforations.

The contour maps of fracture aperture for both cases shown in Figure 2.9 and Figure 2.10 reveal significant variations from stage to stage in the case with 50 perforations per cluster. On the other hand, in the scenario with 10 perforations per cluster, there is no notable difference in fracture length and apertures from stage to stage. From Equation (1.19), with the increase of number of perforations per cluster, the effect of perforation friction in flow partitioning becomes less significant. Consequently, the distribution of flow among individual clusters is entirely dictated by the stress shadow interactions between the fractures. This discrepancy in the fracture growth can be attributed to the presence of stress shadowing. With a higher number of perforations and subsequent increased fracture growth, the induced stress shadow effect becomes more pronounced. This effect has a significant negative impact on the growth of inner fractures in both stages for both wells. But the effect is stronger on the heel side and weaker on the toe side. As fracturing was done first on the toe side and then on the heel side, the toe side fracture did not experience stage to stage stress shadow effect. However, on the heel side fracture propagation, a stress shadow effect was added due to the propagated fractures on the toe side. Consequently, the outermost fractures on the heel side of Stage 2 exhibit the largest lengths among all fractures. This phenomenon is commonly referred to as "heel bias."(Waters et al., 2009). For the case of 10 perforation per clusters, fluid partitions dictated by pressure drop due to perforation friction loss, and there is negligible effect of stress shadow.

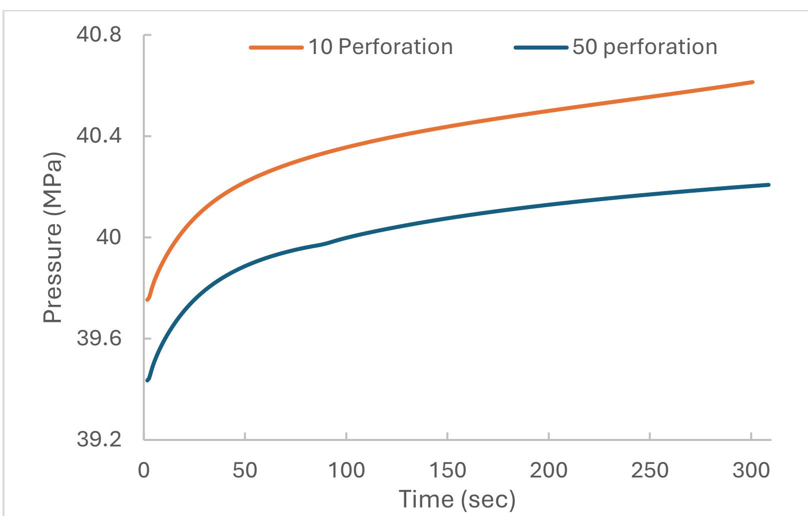

Figure 2.7: Net injection pressure at the wellbore during fracturing with 50 perforations per cluster and 10 perforation per cluster.

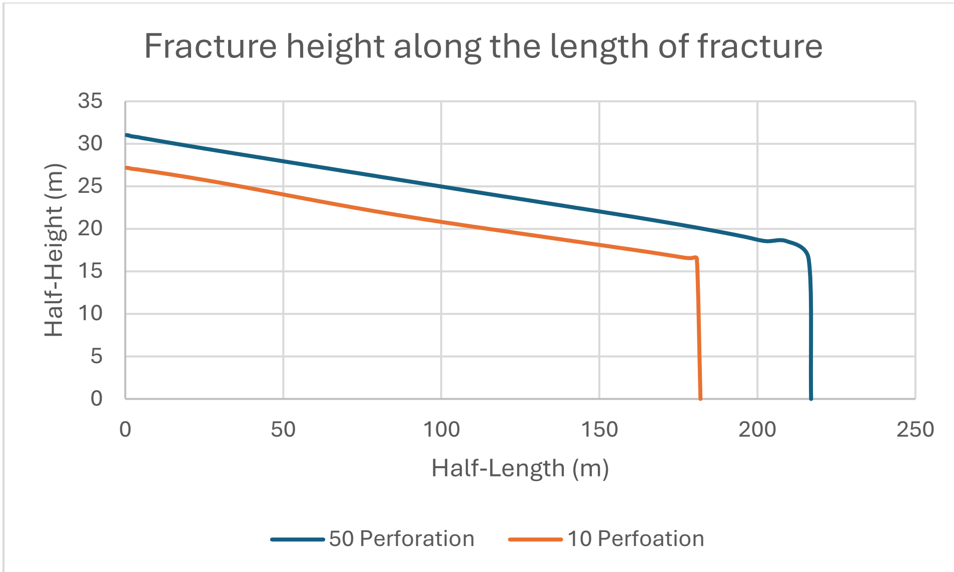

Figure 2.8: Comparison of fracture height along the length of the fracture of 1st fracture of 1st stage for 50 perforations per cluster and 10 perforation per cluster.

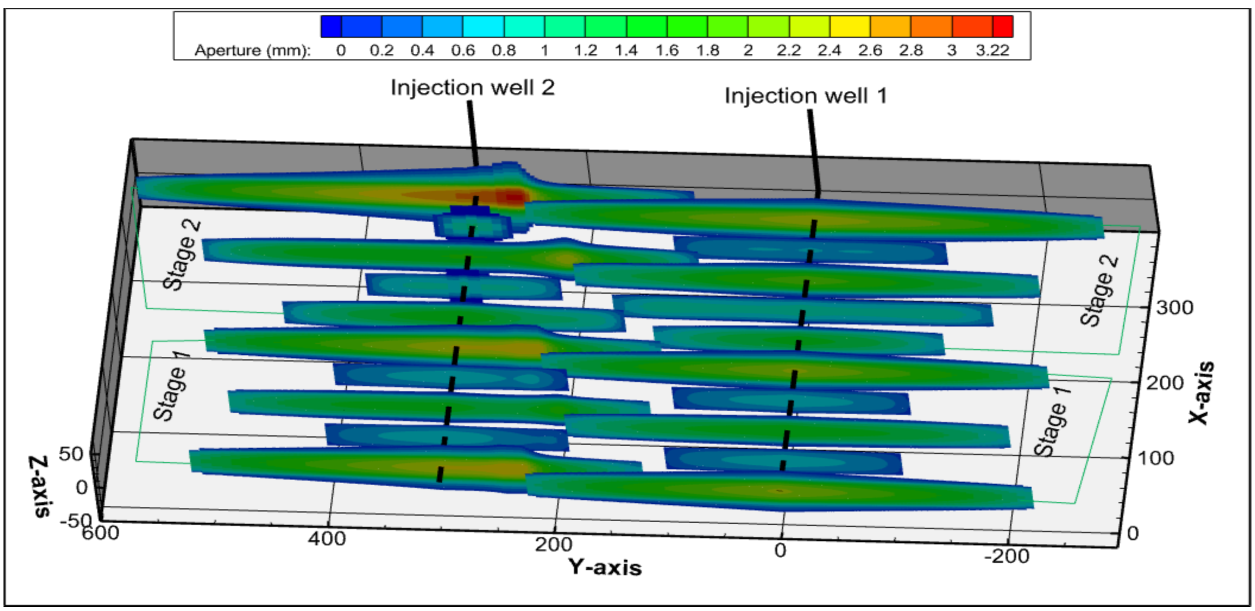

Figure 2.9: Contour map of fracture aperture after 300 sec of injection with number of perforations per cluster is 50.

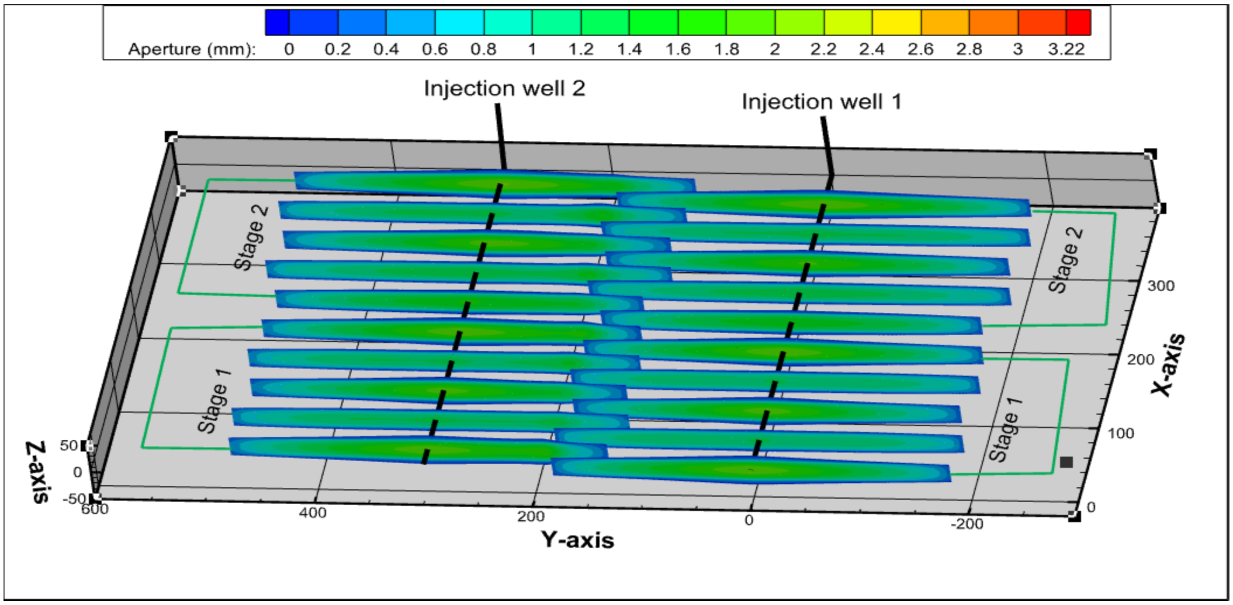

Figure 2.10: Contour map of fracture aperture after 300 sec of injection with number of perforations per cluster is 10.

2.3.2 Effect of fluid leak-off:

To investigate the impact of fluid leak-off on fracture network behavior, a case involving different leak-off coefficients was examined. This was achieved by incorporating a pressure-dependent leak-off term into the fluid flow equation. The Carter leak-off model was employed to quantify the effect of leak-off on the propagation of hydraulic fractures. Two different leak-off coefficients, 1×10^{-4}, and 1×10^{-5}ms$^{-0.5}$ were used to analyze the influence of leak-off on fracture behavior. The rock properties and fracture geometry remained consistent with the previous examples, apart from the injection time, which was extended to 1000 seconds from 300 seconds to better visualize the impact of leak-off.

As the leak-off coefficient increases, the dissipation of fluid from the fractures intensifies, resulting in lower pressures within the fractures as well as reduced wellbore pressure. Since fracture growth is directly proportional to the fluid pressure inside the fractures, fractures experience enhanced growth with lower leak-off coefficients. However, it is important to note that the pressure at the wellbore is not uniform across different stages of the fracture, even with the same leak-off coefficient. This variation arises due to the presence of stress shadowing effects. Subsequent stage fractures experience higher injection pressures compared to previous stage fractures, as the new fractures are formed within the influence of stress shadowing.

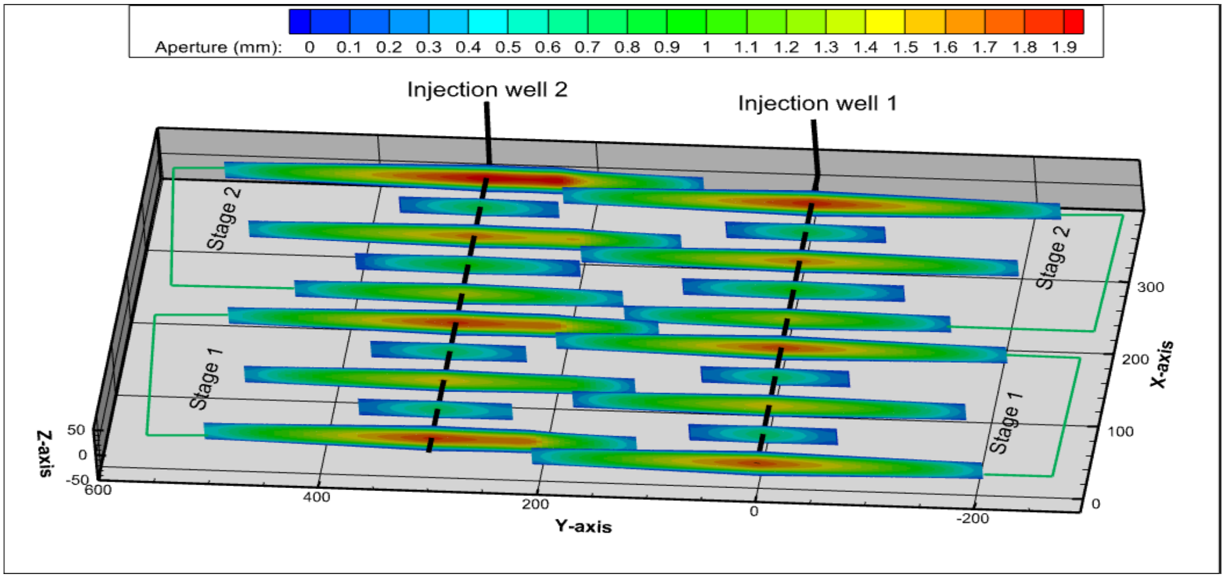

Figure 2.11: Contour map of fracture aperture for fluid leak-off coefficient 1×10^{-5} *ms*$^{-0.5}$ *after 1000 sec fluid injection at a rate of 80 bpm per stage.*

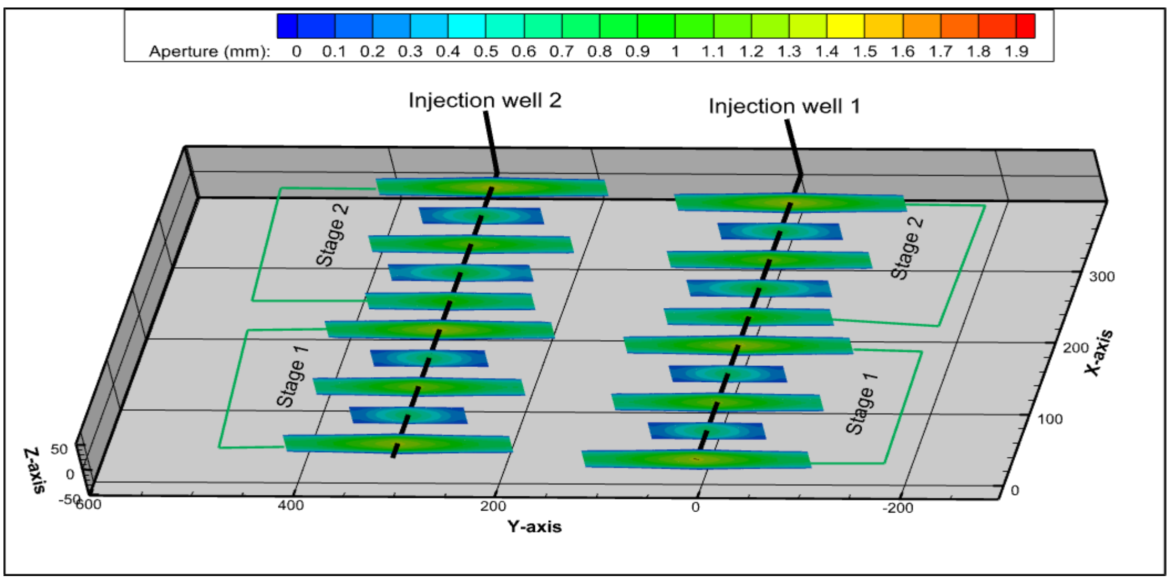

Figure 2.12: Contour map of fracture aperture for fluid leak-off coefficient 1×10^{-4} *ms*$^{-0.5}$ *after 1000 sec fluid injection at a rate of 80 bpm per stage.*

2.4 Proppant Transport in P3D Anisotropic model:

Multi-stage and multi-cluster fracturing treatments in horizontal wells are essential for the efficient development of unconventional reservoirs with very low permeability. The developed proppant transport model enables the simulation of proppant placement across multiple hydraulic fractures (Liu & Ghassemi, 2024) in a rapid multi-cluster, multi-stage hydraulic fracture model. To validate the proppant transport model is working, a single cluster fracture was propagated, and proppant was injected into the cluster. The simulation was run for 15 minutes, where fluid was pumped for 10 minutes at a rate of 15 bpm (0.04 m^3/s) and 5 minutes shut-in periods to settle the proppant. Proppant injections were initiated after 5 minutes of fluid pumping at a rate of 15 bpm (0.04 m^3/s). Proppants parameters are given in Table 2-6, and other input parameters are same previous examples.

Table 2-6: Injected proppant properties.

E (GPa)	ϑ	Proppant density (kg/m^3)	Radius of proppant (m)	Q_0 (bpm)	σ_b (MPa)
50	0.15	2650	3×10^{-4}	15	1.0

Figure 2.14 illustrate the contour maps of proppant concentration within the fracture, as predicted by the R3D and P3D models. Both models indicate that the proppant tends to accumulate at the lower portion of the fracture, particularly near the fracture base. The results also show that in both models, the proppant travels approximately 50-60 meters along the fracture length.

However, the fracture simulated using the R3D model exhibits a higher fracture aperture and more pronounced height growth compared to the P3D model. In contrast, the P3D model predicts a longer fracture length but with lower fracture aperture and reduced height growth.

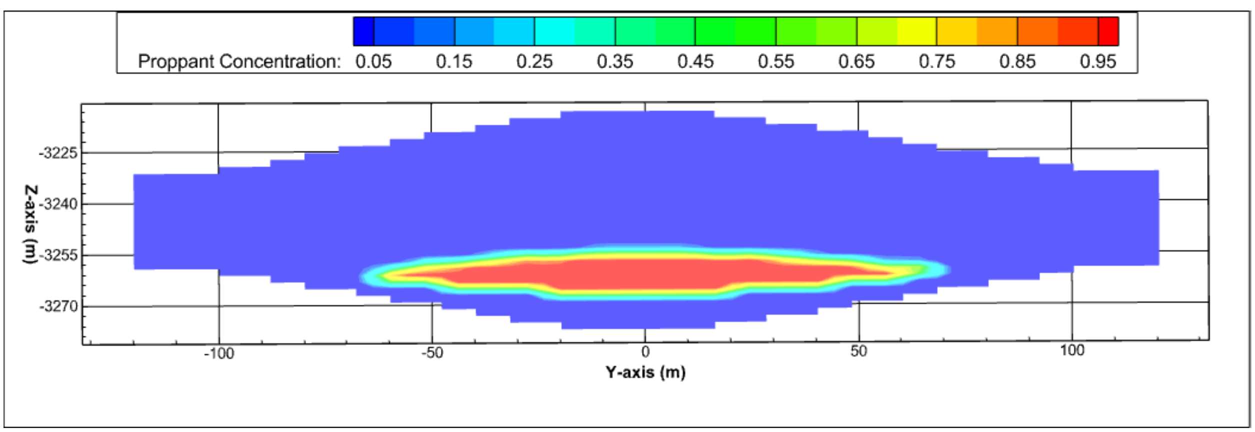

Figure 2.13: Contour map of proppant concentration within the fracture after 5 minutes of injection at a rate of 15 bpm, followed by a 5-minute shut-in period, as simulated using the R3D fracture model.

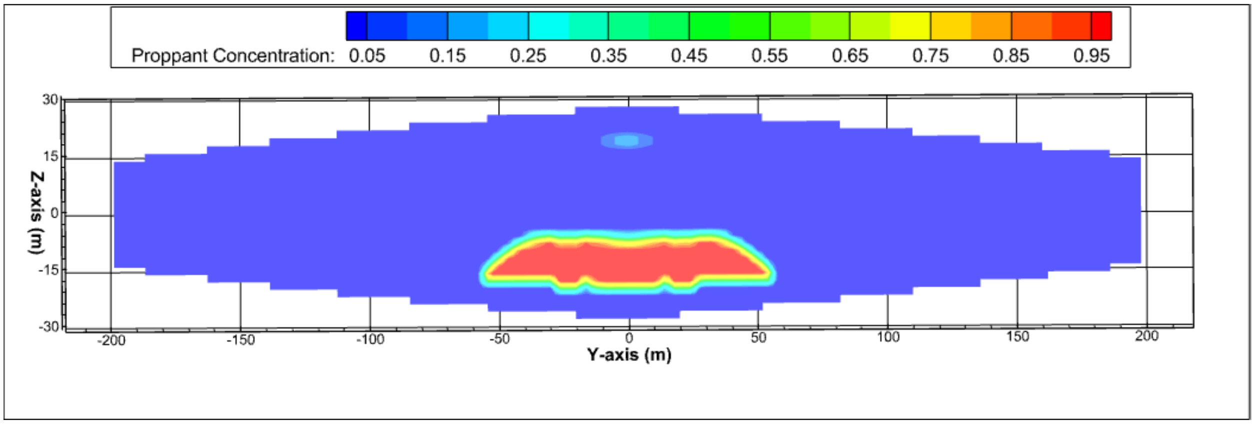

Figure 2.14: Contour map of proppant concentration within the fracture after 5 minutes of injection at a rate of 15 bpm, followed by a 5-minute shut-in period, as simulated using the P3D fracture model.

2.4.1 Multi-cluster example with proppant:

To simulate simultaneous propagation of hydraulic fractures from multiple perforation clusters using anisotropic P3D model, at the end of every time step, stress shadow between the fractures need to calculate. 2D DDM for anisotropic rock were employed to evaluate the induced stress on one fracture due displacement discontinuity on other fractures. Induced stress was calculated at the center of the pay zone and stress barriers were assumed to be the same as the initial conditions. In the next timestep, these induced normal stresses are added to far-field stress. This way of externally calculating induced stresses using a 2D DDM after every timestep mimics the interaction between multiple fractures.

In this example, we propagate 5 clusters simultaneously with each cluster separated by 20 m. To stimulate the fractures, water with a viscosity of 3 cp was injected at a rate of 50 bpm for a duration of 10 minutes in each fracturing stage. In this example we used 10 number of perforations per cluster. Additionally, symmetrical barriers located above and below the pay zone experienced an excess stress of 1 megapascals (MPa). No perforation friction was considered in this case. Negligible leak-off, referring to the no fluid loss into the surrounding formation, was considered in these simulations. The input parameters are listed in Table 2-2 and Table 2-3. Proppant injection was initiated after 100 seconds of the fracture simulation started and ended at 10 minutes of simulation. And then proppant was allowed to settle down for 2 minutes. Proppant parameters were given in Table 2-6.

Figure 1.29 presents the contour map of fracture aperture distribution for anisotropic rock, while Figure 1.30 shows the contour map of proppant concentration at each cluster after 10 minutes of simulation using the P3D model. The figures demonstrate that due to the high stress shadow effects, the growth of the inner fractures was constrained, resulting in reduced fracture aperture and limited proppant distribution within these regions.

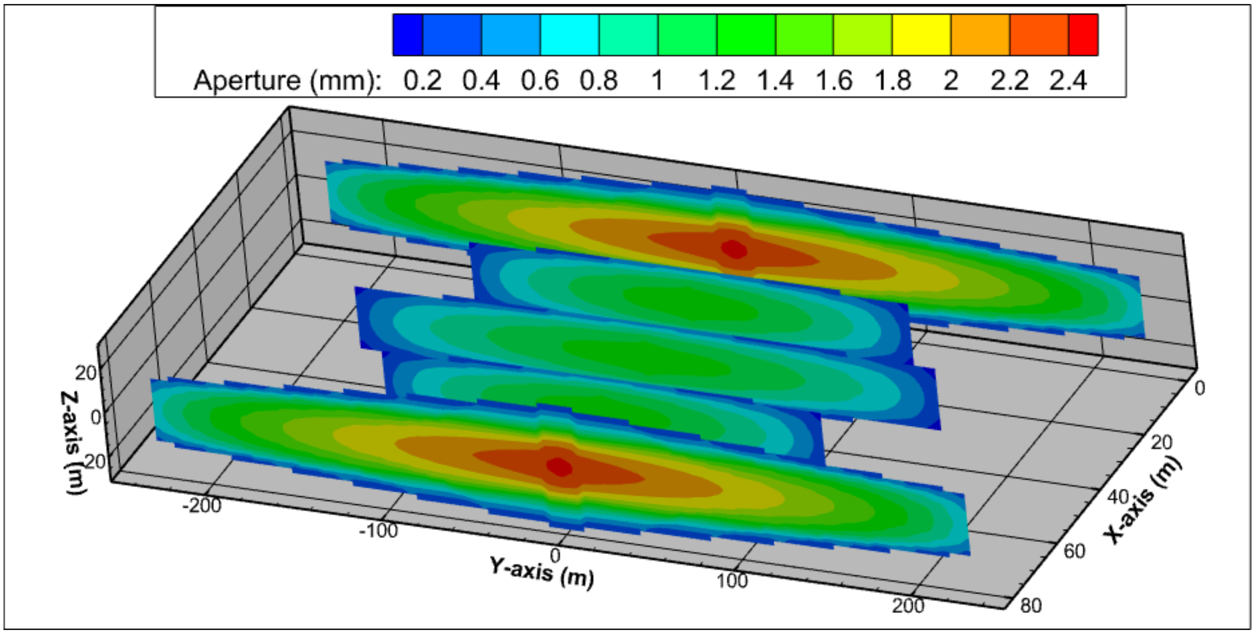

Figure 2.15: Contour map illustrating the fracture geometry following 10 minutes of fluid injection in anisotropic rock, simulated using the P3D model. The injection fluid has a viscosity of 3 cP.

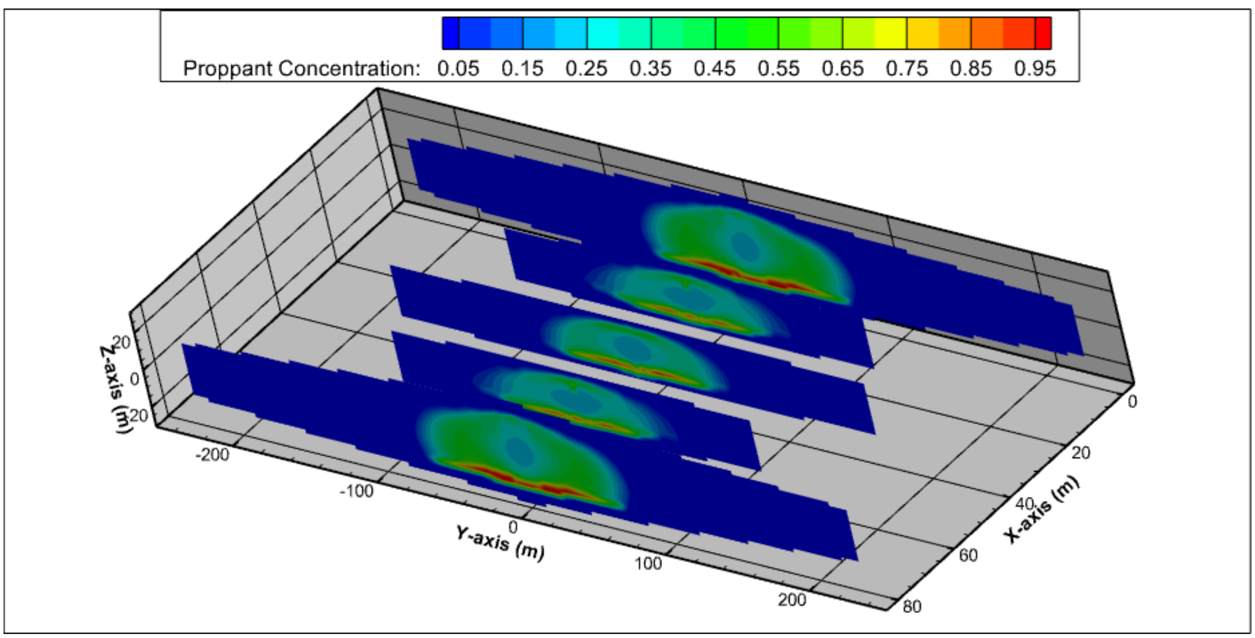

Figure 2.16: Contour map of proppant concentration around the fracture before shut-in simulated by using P3D model for anisotropic rock.

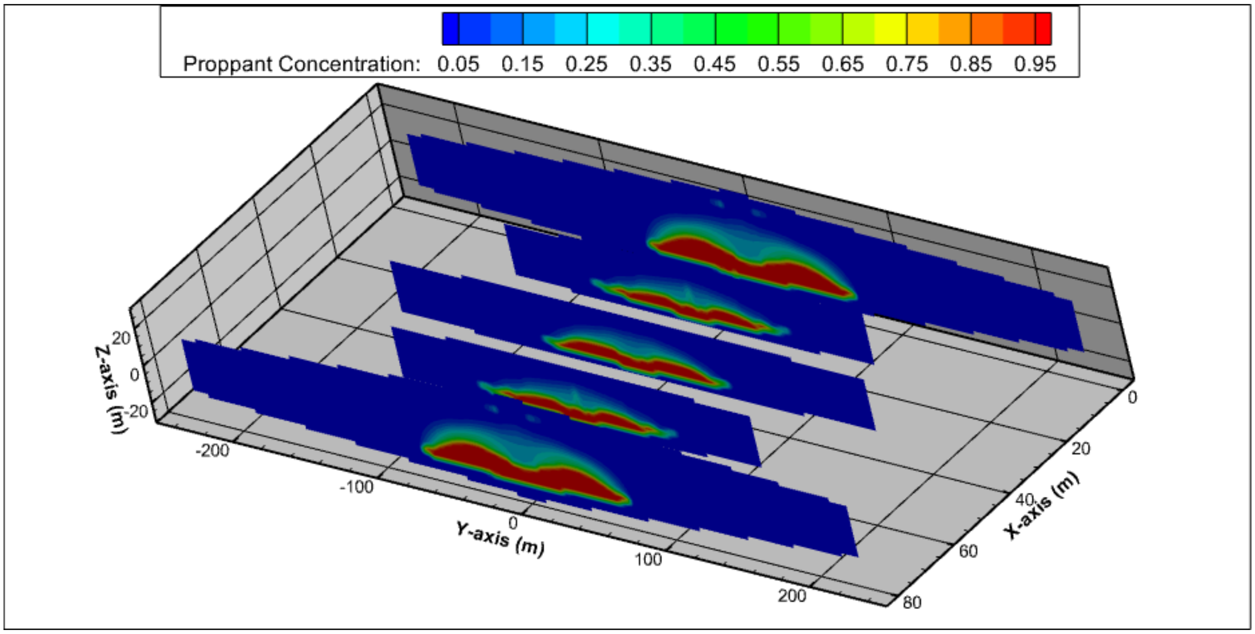

Figure 2.17: Contour map of proppant concentration around the fracture after the injection being shut down for 2 minutes for anisotropic rock.

Chapter 3 Characterization of proppant and applicability in Geothermal field

3.1 Introduction:

In recent decades, advances in hydraulic fracturing technology have enhanced production from unconventional oil and gas reservoirs, as well as from geothermal resources. As most geothermal fields are in formations that consist of igneous and metamorphic rock with low permeability, it requires different stimulation techniques to extract heat energy efficiently. Along with the unconventional reservoir and geothermal field, hydraulic fracturing technique also adapt in extracting coal bed methane (Suponik et al., 2023). Hydraulic fracturing is the prevailing and viable method of stimulation that establishes the primary flow path for fluid towards a producing wellbore (Ghassemi et al., 2005). Due to high in-situ compressive stress, the fracture tends to close and result in permeability reduction. To avoid the closure of fractures, proppant is inserted into the fracture to withstand the in-situ force and keep the fracture open. Proppants are granular materials, usually sand or ceramic particles, that are injected into fractures to keep them open and so increase hydrocarbon flow from the reservoir to the wellbore. When proppants are placed between cracks, they tend to form a proppant pack and fluid can flow through their porous volume and in channels around distributed packs (Hari et al., 2021), as shown in Figure 3.1. The appropriate selection and evaluation of proppants is a crucial factor that has a considerable influence on the efficacy of hydraulic fracturing. Proppant cost, density, and strength are key factors to consider when selecting proppant, especially in practical applications where significant quantities of proppant must be mixed with water and injected into the field. Among the wide array of proppants used, petroleum coke proppants have gained significant attention in recent times due to their notable advantages in terms of being lightweight and cost-effective. The most important parameter of hydraulic fracturing is the conductivity of the fracture which is defined as the multiplication of fracture permeability with fracture width. The width of the producing fracture varies with closure stress, amount of proppant within the fracture, proppant strength, and formation hardness and (Mcdaniel & Services, 1986). The overall strength of the proppants is assessed by evaluating two critical parameters: crush resistance and packing strength. Crush resistance is defined as the maximum amount of stress that a proppant can withstand before producing more than 10% fines. It essentially assesses the proppant's capacity to endure the in-situ stress within the fracture without breaking down into fine particles that could diminishes the fracture permeability. Packing strength, on the other hand, refers to the proppant's ability to sustain fracture width under in-situ stress circumstances (Ko et al., n.d.). To ensure the efficient and sustainable development of these resources, proppant crush testing has emerged as a pivotal area of research, offering insights into the mechanical behavior and performance of petroleum coke proppants under downhole conditions. To most important mechanical parameters of a proppant should be considered before selecting a proppant: proppant crush resistance (which is also known as K value) and proppant packing strength. The mechanical properties, including crush resistance and packing strength, exhibit significant variability depending on the test conditions and the size of the proppant (Bandara et al., 2021; Palisch et al., 2010). It is important to note that the crush resistance of dry proppant differs from that of wet proppant of the same size and other relevant parameters (Simo et al., n.d.; Zheng et al., 2018). Furthermore, even when conducting tests under identical conditions using the same proppant material, the strength of the proppant greatly varies with its size (Ko et al., n.d.). Consequently, comprehensive testing involving different conditions and diverse size distributions of proppant is essential for obtaining thorough insights to aid in the selection of the most suitable proppant.

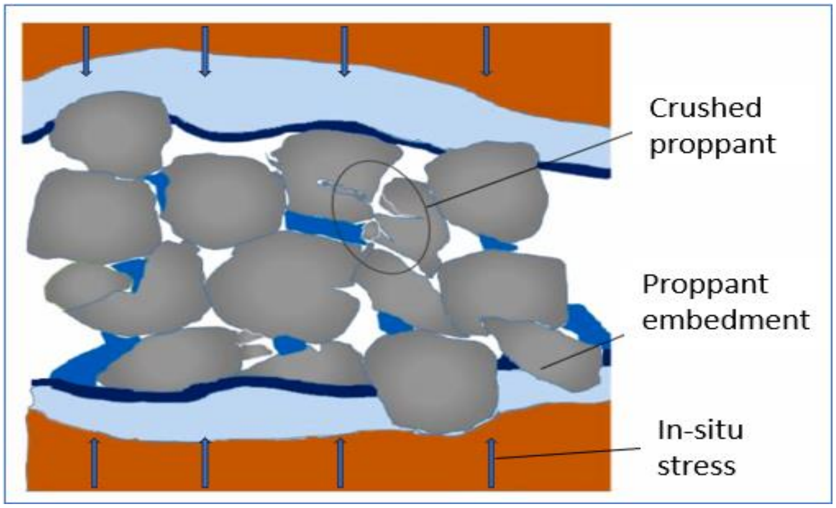

Figure 3.1: Visual representation of proppant embedment and proppant crushing under reservoir in-situ stress (Hari et al., 2021).

In this Experimental work, the Standard procedure provided by American Petroleum Institute (API) ISO 13503-2 (ISO/FDIS 13503-2, 2006) is followed to determine the crush resistance of the proppant. The acoustic emission data emitted from the crushed cell due to crushing is collected and used to estimate the packing strength of the proppant. In this study, we evaluated the crush strength and packing strength of three distinct proppant materials: petroleum coke-based proppants (PC), high-transported ultra-low-density ceramic proppants (LDC), and resin-coated ceramic proppants (RC). The tests were conducted on both wet and dry proppants to assess the changes in packing strength and crush resistance under varying conditions. We tested two mesh sizes (10/35 and 35/60) for each type of proppant. To investigate the impact of high temperatures on the mechanical properties of the proppants, wet crush tests were performed on samples subjected to a high temperature of 300 °C for 7 and 14 days. These experimental results offer valuable insights into the behavior of proppant packs in Enhanced Geothermal Systems (EGS) at approximately 300 °C, contributing to the design of advanced proppants for geothermal applications. Additionally, Scanning Electron Microscopy with Energy Dispersive X-ray Spectroscopy (SEM-EDX) analysis was conducted to observe surface structure changes after heat exposure. Given that petroleum coke-based proppants are cheaper and weaker compared to ceramic-based proppants, we also performed crush tests on mixtures of PC with LDC and RC at varying ratios. These mixed proppant tests were carried out at a fixed pressure of 5000 psi (34.5 MPa) to determine the most economical and effective mixing ratio for field injection. We selected 5000 psi as the test pressure because it is the most common reservoir pressure encountered in field conditions. By analyzing stress-strain data and crush percentages across different mixing ratios, we can propose optimal mixing ratios for practical applications.

3.2 Sample preparation and Material properties:

Three distinct proppant materials: petroleum coke-based proppants (PC), high-transported ultra-low-density ceramic proppants (LDC), and resin-coated ceramic proppants (RC) were prepared for the test. Before running the crush resistance test, elemental composition, bulk density, sphericity, and roundness were first characterized. As the strength of the proppant varies with the size of the proppant, in this study, two distinct size distributions of all three types of proppants have been tested to assess their suitability for use in hydraulic fracturing to keep the fracture open by resisting closure pressure. The proppant samples were sieved using a RO-TAP RX-29 sieve shaker, as shown in Figure 3.3. We used two different mesh sizes for our experimental analysis: 10/35 (with particle sizes ranging from 2000 to 500 microns) and 35/60 (with particle sizes falling between 500 and 250 microns). These sample sizes were chosen due to their ample availability, ensuring we had enough to carry out the test. According to the guidelines prescribed in ISO 13503-2, raw proppant samples were shaken for 10 minutes by a sieve shaker. Following the sieving, two desired-size distributed samples were collected to be used in the crush test. After sieving, the average bulk density of the proppant of each size distribution was measured. According to ISO 130503-2, the proppant concentration 4 lb/ft^2 was used. The mass of proppant (m_p) needed for each test is then calculated using the equation $m_p = 24.7 \times \rho_{bulk}$. For the mixed testing, samples were prepared by combining proppants in various weight ratios: 1:3, 1:1, and 3:1. Specifically, the mixtures included 25% PC with 75% LDC, 50% PC with 50% LDC, 75% PC with 25% LDC, 25% PC with 75% RC, 50% PC with 50% RC, and 75% PC with 25% RC. In the context of proppant usage in well stimulation, the bulk density of the proppant plays a crucial role in determining the necessary mass of proppant to be injected into the well, and it also determines how far proppant will travel. Proppant with smaller bulk density will go far from the injection point whereas heavier proppant will settle close to the injection point. Moreover, the bulk density value serves as a key parameter for calculating the required sample mass for testing within the crush cell. Density measurement data and proppant shape are given below in Table 1. The shape of the proppants was determined by visual estimation based on the chart given by iso standard (shown in Figure 3.2).

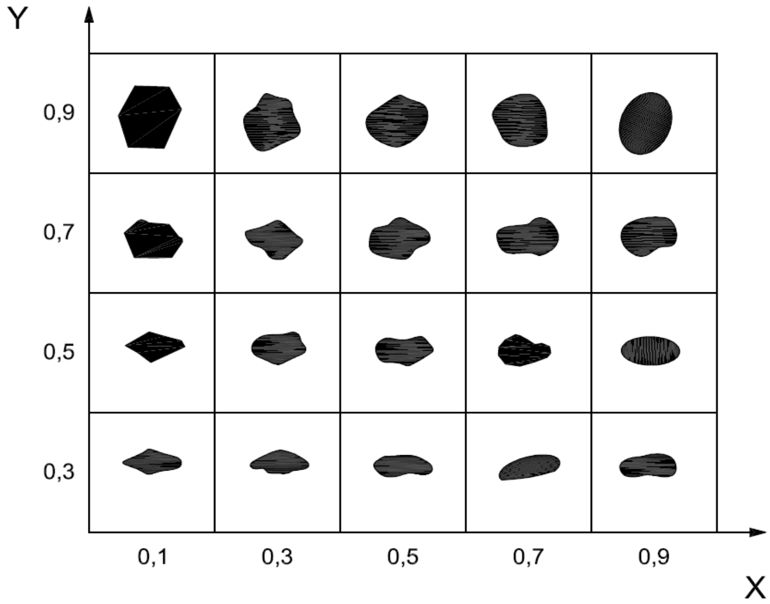

Figure 3.2: Chart for visual estimation of Roundness and Sphericity. (X= Roundness, Y= Sphericity).

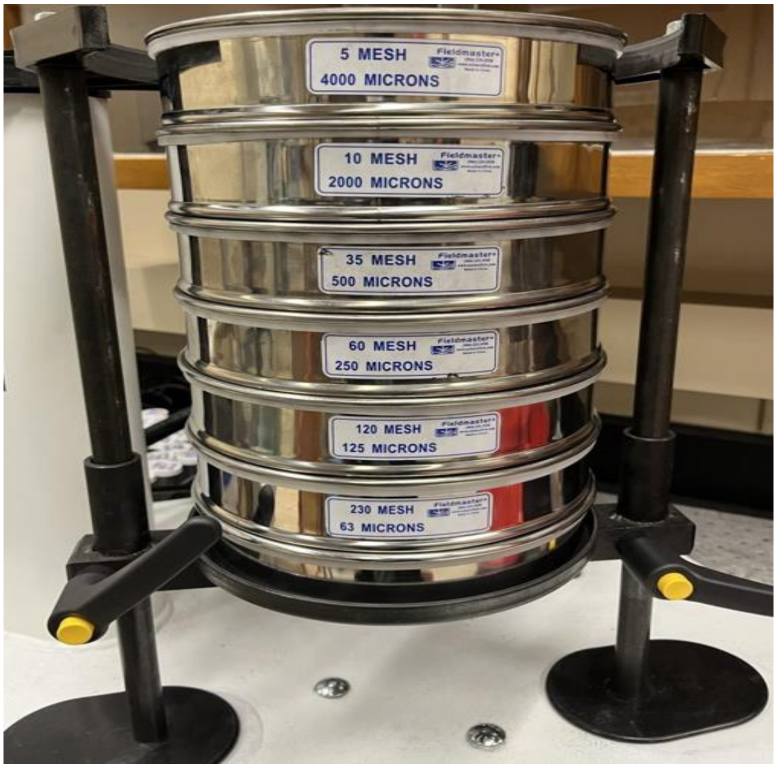

Figure 3.3: The arrangement of multiple sieves stacked within a sieve shaker with decreasing sieve openings from top to bottom.

Table- 1:

Table 3-1: Density Measurement and the shape of Proppants of Various Sizes.

Type of proppant	Sizes	Bulk Density (gm/cc)	Proppant shape (X= Roundness, Y= sphericity)
Pet coke	10/35	1.09	(0.7,0.7)
	35/60	0.99	(0.3,0.5)
LDC	10/35	1.21	(0.9,0.9)
	35/60	1.27	(0.9,0.9)
RC	10/35	1.6	(0.9,0.9)
	35/60	1.53	(0.9,0.9)

3.3 Proppant description:

3.3.1 Resin-Coated Ceramic:

The higher-strength CARBOBOND LITE resin-coated high-performance ceramic proppant is effective at greater well depths and stresses. CARBOBOND LITE resin-coated is designed with high cyclic loading tolerance, while the bonded proppant pack reduces the effective stresses encountered deeper depths. The SEM-EDX analysis in Table 3-2 shows it consists of 61 % carbon, 12.4% nitrogen, and 24.2 % Oxygen. The scanning electron microscope (SEM) image shows that the proppant surface doesn’t have any noticeable micro-cracks in it before exposed high temperature (Figure 3.4).

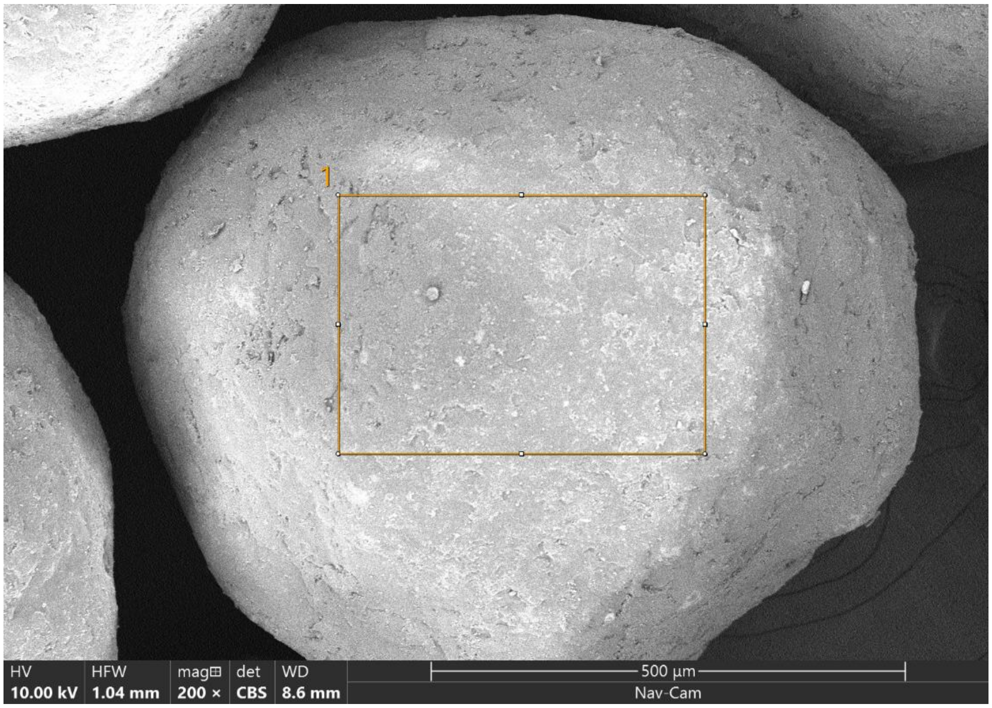

Figure 3.4: SEM image of resin-coated ceramic proppant of 10/35 mesh size.

Table 3-2: SEM-EDX report of resin-coated ceramic proppants.

Element	Atomic %	Atomic % Error	Weight %	Weight % Error
C	60.9	0.2	45.3	0.1
N	12.4	0.8	10.8	0.7
O	24.2	0.4	24.0	0.4
Al	0.5	0.0	0.8	0.0
Si	0.5	0.0	0.9	0.0
Ir	1.5	0.1	18.3	0.7

3.3.2 Ultra Low-Density Ceramic:

CARBOAIR high-transport, ultra low-density ceramic proppant technology enables operators to efficiently inject proppant at the long fracture. One of the key advantages of this proppant is that it can travel a long distance as the density is low, and it's much stronger compared to the petroleum coke-based proppants. The SEM-EDX analysis in Table 3-3 shows it consists of 69.3 % carbon, 27.6 % Oxygen, and trace number of other molecules. The scanning electron microscope (SEM) image shows that the proppant surface doesn't have any noticeable micro-cracks in it before exposed high temperature (Figure 3.5).

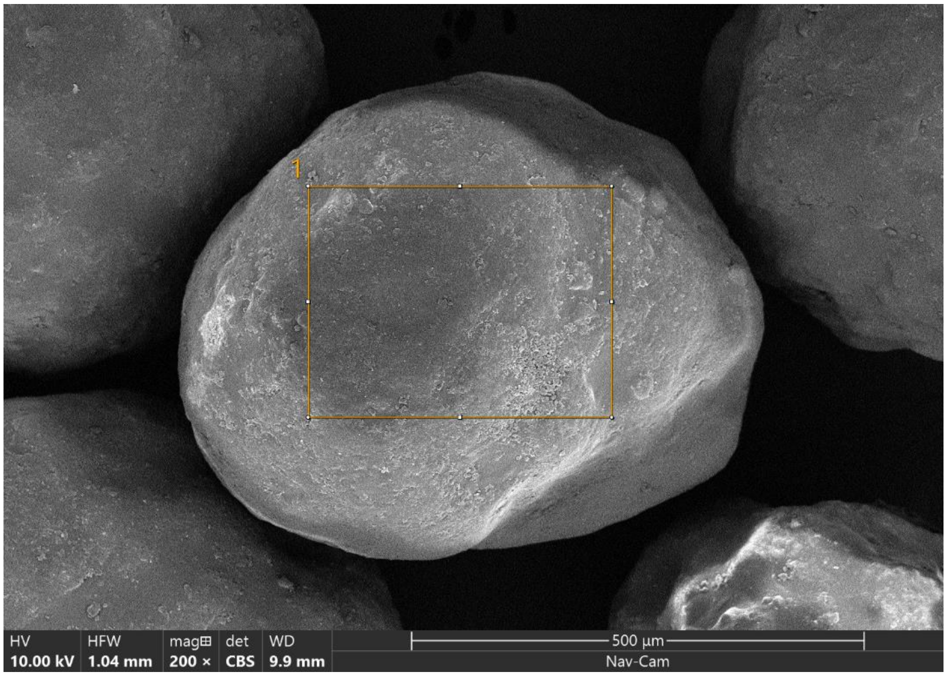

Figure 3.5: SEM image of ultra-low density ceramic proppant of 10/35 mesh size.

Table 3-3: SEM-EDX report of ultra-low density ceramic proppants.

Element	**Atomic %**	**Atomic % Error**	**Weight %**	**Weight % Error**
C	69.3	0.2	51.1	0.2
O	27.6	0.2	27.1	0.2
Na	0.5	0.0	0.7	0.0
Al	0.3	0.0	0.4	0.0
Si	0.3	0.0	0.5	0.0
Cl	0.5	0.0	1.1	0.0
Ir	1.6	0.0	19.0	0.5

3.3.3 Petroleum Coke:

Petroleum Coke is a carbon-rich material derived from oil refining processes and is often used for fuel or aluminum manufacturing. Coke is a material obtained from the pyrolysis of hard coal carried out at a temperature of approximately 1000 °C (Suponik et al., 2023). The structure of the Coke proppant limits its embedment. Due to its roughness, it supports the fracture wall at multiple points and reduces embedment compared to proppants of a smoother grain surface, such as treated sand, ceramics, and resin-coated proppants (Suponik et al., 2023). The SEM-EDX analysis in Figure 4 (b) shows it consists of 96 % carbon and 3.67 % sulfur. The scanning electron microscope (SEM) image shows that the proppant has few micro-cracks in it before applying any stress. The presence of microcracks will lead the proppant to fail at low stress. Petroleum coke proppants are well-known for their relatively low density and low price. When paired with low-viscosity foams and fracking fluids, this intrinsic feature allows them to be used more efficiently (Labus et al., 2019; Suponik et al., 2023). Furthermore, the low bulk and specific densities of coke proppants allow for the injection of large volumes of proppant from a single well into remote regions of the fractures. Petroleum coke proppant has a bulk density value that is nearly half that of sand. One main drawback of petroleum coke-based proppant is that they are relatively weak which make them less effective in keeping the fracture open.

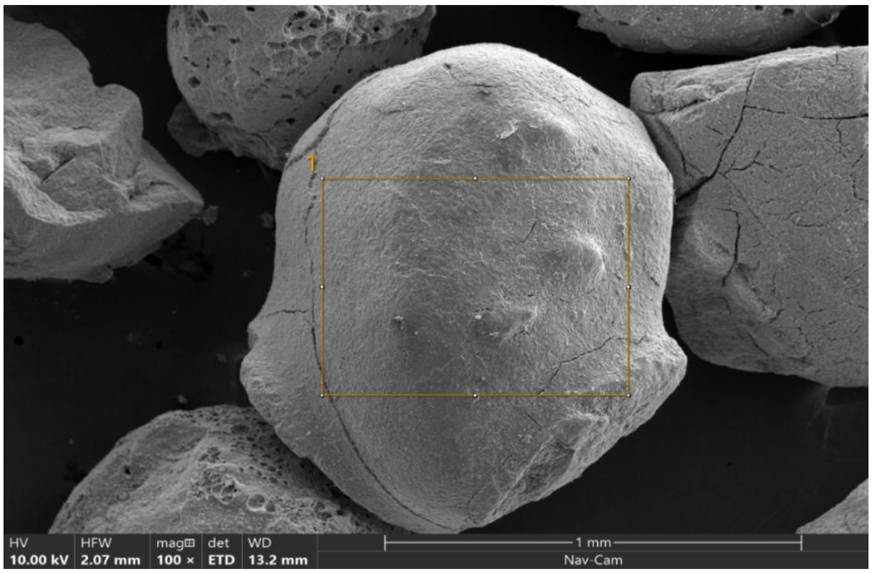

Figure 3.6: SEM image of proppant 10/35 consisting of petroleum coke.

Table 3-4: EDX results show element composition of proppant.

Element	Atomic %	Atomic % Error	Weight %	Weight % Error
C	94.3	0.2	71.4	0.2
Al	0.2	0.0	0.3	0.0
Si	0.1	0.0	0.2	0.0
S	3.6	0.0	7.4	0.0
Ir	1.7	0.0	20.8	0.4

3.4 Methodology:

The standard crush test procedure provided by ISO 130503-2 is being followed to conduct the test. In this proppant crush testing procedure, the first step involves sieving the proppant and separate them based on their size distribution. In the next step, the bulk density (ρ_{bulk}) of the proppant material was measured. According to ISO 130503-2, the proppant concentration 4 lb/ft^2 was used. The mass of proppant (m_p) needed for each test is then calculated using the equation $m_p = 24.7 \times \rho_{bulk}$. Next, the test cell is loaded carefully to achieve a consistent loose pack with a level surface. The piston is gently inserted into the test cell containing the pre-weighed proppant sample without applying any additional force. To ensure a level surface in the proppant pack, the piston is rotated clockwise by 180° once without applying extra pressure.

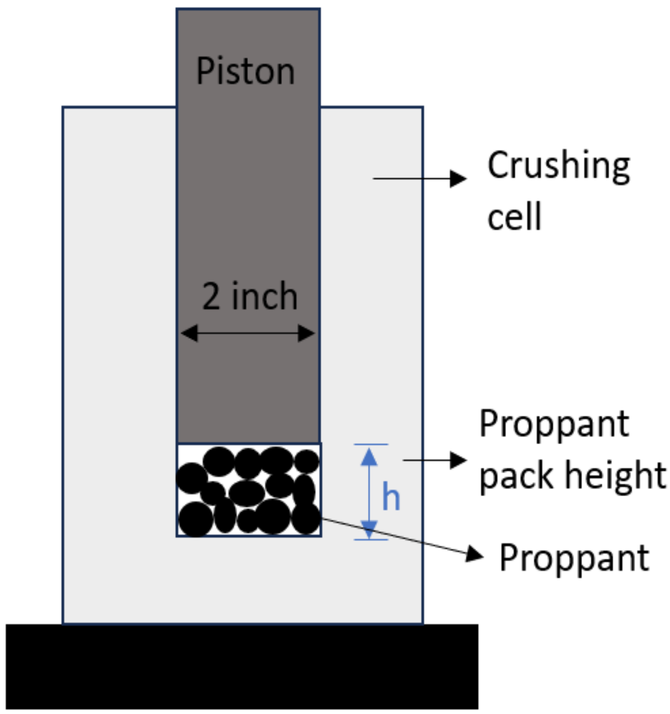

Figure 3.7: Schematic diagram of proppant crush cell assembly.

Hydraulic load frame with the capacity to apply very high load is used for this test to crush the proppant. The cell is placed beneath the loading piston of the MTS loading frame, ensuring its central positioning for uniform load distribution. For the crush test, the appropriate stress is applied to the test-cell piston at a constant rate of 2,000 psi/min, resulting in an applied load of F = 2000 * 3.1416 = 6283 lbf per minute, considering the piston's 2-inch diameter (with an area of 3.1416 inch^2). When the final stress level is achieved, the stress level is held for 2 minutes before being released. After crush testing, the proppant mass is re-screened to determine the percentage of fines generated due to the applied stress. Any particles smaller than the initial size of the proppant are categorized as fines. This test is repeated for the new sample of the same size with the final stress increment of 1000 psi until the percentage of fines generates exceed

10%. The "K-value" is determined as the maximum stress level attained during the testing process without exceeding 10.0% fines generation. This comprehensive procedure provides critical insights into the proppant's mechanical behavior, crush resistance, and packing strength, aiding in the selection and optimization of proppant materials for hydraulic fracturing and other applications. For the mixed proppants, a final stress of 5000 psi was applied to all samples using a hydraulic load frame at a loading rate of 2000 psi/min. Once the target stress level was reached, it was maintained for 2 minutes before being released. After the crush testing, the proppant mass was re-screened to quantify the percentage of fines generated due to the applied stress.

3.4.1 Heated Test Procedure:

To replicate the high-temperature conditions of Enhanced Geothermal Systems (EGS) in the laboratory, the proppant material was subjected to heating using tap water at a temperature of 300°C. The water-immersed proppant was placed into a specialized vessel capable of withstanding high pressure and temperature conditions, and then the vessel was plugged tightly to prevent steam leakage. Figure 3.8(a) shows the pressure vessels that were used to heat the proppant, Figure-6 (b) shows conceptual inside view of the vessel. Then the vessel was inserted into the oven at 300°C for 7, 14, and 30 days separately. Once the desired heating duration was attained, the vessel was allowed to cool down in the water. Following the cool-down, the vessel was unplugged, and the presence of water was checked. If water inside the vessel evaporates, then the previous steps should be repeated with new samples. Water was collected from inside the vessel to conduct chemical testing of water to analyze the dissolution of the proppant into water.

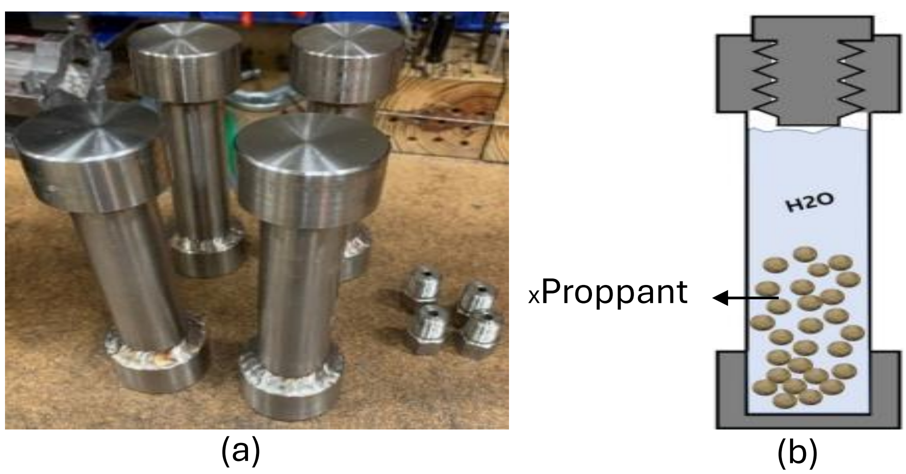

Figure 3.8: Pressure vessel used for heating proppants with water, b) inside view of the vessel.

After heating, the proppant was carefully transferred to a testing cell, where a wet crush test was conducted to assess its crush resistance in a wet state. Following the test, the crushed sample was collected and thoroughly dried to eliminate any remaining moisture. The total mass of the dried and crushed sample was recorded before sieving to account for any mass loss that might have occurred during the heating and transportation processes. Then the dried crushed samples were sieved to determine the percentage of fine generated at applied stress. Since the proppants were immersed in water while inside the vessel during the heating process, and the crush tests were conducted on these wet proppants, the heated test is referred to as a wet test.

3.4.2 Acoustic Emission:

Acoustic emissions (AE) are elastic waves emitted by a material or structure undergoing sudden fractures or frictional sliding along discontinuities and grain boundaries. AE testing has gained recognition as a nondestructive test (NDT) method widely employed to detect and locate microcracking in mechanically loaded structures and components (Hampton, 2015). However, AE data can be influenced by background noise, which includes any unwanted signals picked up by the sensors. An AE system generally consists of various components, including a sensor, preamplifier, filter, amplifier, display, and data storage units. AE sensors respond to dynamic motion from AE events through transducers that convert mechanical motion into electrical signals, typically utilizing a piezoelectric crystal, often made from lead zirconate titanate (PZT). In this study, two AE sensors were positioned near the bottom of the crushed cell to gather soundwave data emitted by the proppant during loading. AE data were captured using AEwins software by MISTRAS Group. The collected AE data is instrumental in understanding the proppant's response to stress. Acoustic emission (AE) data were collected by connecting two AE piezoelectric transducers to the side of the crushed cell near the bottom as shown in Figure 7(a). Figure 7(b) shows the hydraulic frame that was used for applying stress.

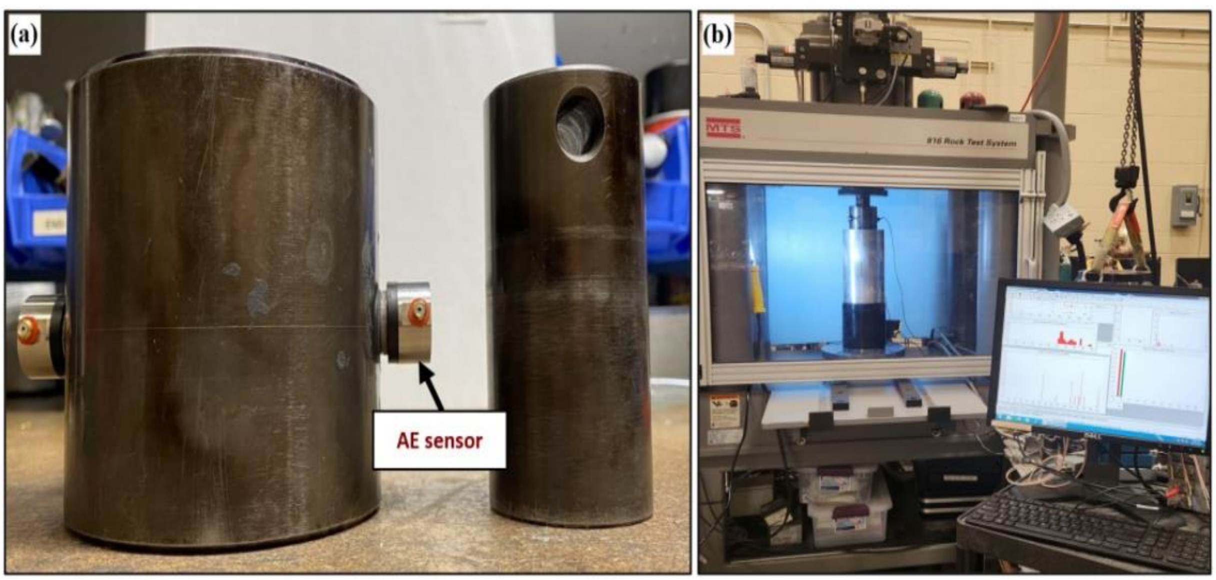

Figure 3.9: (a) Proppant crush test cell with acoustic emission transducers attached and piston on the right and (b) overall crush test set-up with hydraulic frame.

As the proppant grains are crushed during the crush test, acoustic emissions are generated and recorded, containing vital information such as frequency, amplitude, count, AE hit rate, and so on. The acoustic emission data is then analyzed to determine the packing strength of the proppant.

A data filter was applied to eliminate low to mid-amplitude noise that could have been caused by frictional sliding between proppants. The acoustic emission (AE) measurements were post-processed and synchronized with the hydraulic load frame stress profile and displacement profile. Post-processing was accomplished using Python and Excel. Notably, there is a noticeable reduction in the hit rate of the proppant pack after undergoing significant crushing, indicating the attainment of a critical stress level that closely approximates the strength of the proppant packing. This deflection in hit rate becomes evident even before the target stress value selected for the crush resistance test is reached. The deflection of the AE hit rate indicates that the proppant has reached its ultimate packing strength. The AE rate plot was synchronized with the stress plot over time to estimate the packing strength of the proppant.

3.5 Result and Discussion:

3.5.1 Dry Test Results:

A series of crush experiments were performed under different settings with two different proppant sizes, namely 10/35 mesh and 35/60 mesh. These tests were conducted in both wet and dry conditions in order to fully assess their performance. During the phase of dry testing, the significant frictional contacts among the proppant grains resulted in a notable amount of undesired noise in the acoustic emission (AE) data. To address this issue, the AE data was subjected to a filtering process to remove the noise from the raw data. Amplitude values less than 70dB were disregarded from the analysis since they were deemed to be noise. As the crushing rate of proppant increases with the increasing applied stress, the number of hits also exhibited a corresponding rise as proppant crush. However, after a certain stress, the number of hits started decreasing, indicating that the applied stress had exceeded the critical stress limit. Figure 3.10 depicts the hit rate, stress, and displacement over time for 10/35 dry proppant. This decrease in the number of hits was observed at approximately 107 seconds, indicating that the proppant had undergone severe crushing and had reached the critical stress level. From Figure 3.10, synchronizing the stress plot with hit rate plot, the applied stress at 107 seconds was measured at 2000 psi. For the dry proppant of size 35/60, the hit rate, stress, and displacement over time is shown in Figure 3.11. From Figure 3.11, the AE rate started to drop at 78 seconds, the applied stress at 78 seconds was measured at 1500 psi. The results suggest that higher size proppant shows the higher packing strength. This critical stress can be regarded as the packing strength of the proppant. The identified critical stress level serves as a significant parameter in understanding the proppant's performance and suitability for hydraulic fracturing operations and other applications.

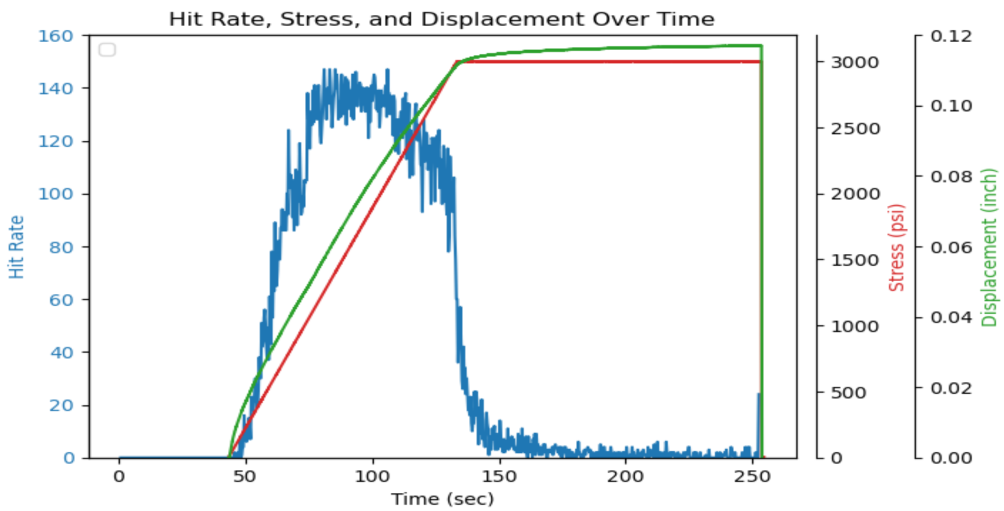

Figure 3.10: AE hit rate, applied stress, and displacement with respect to time during the crush test of petroleum coke-based proppant of size 10/35.

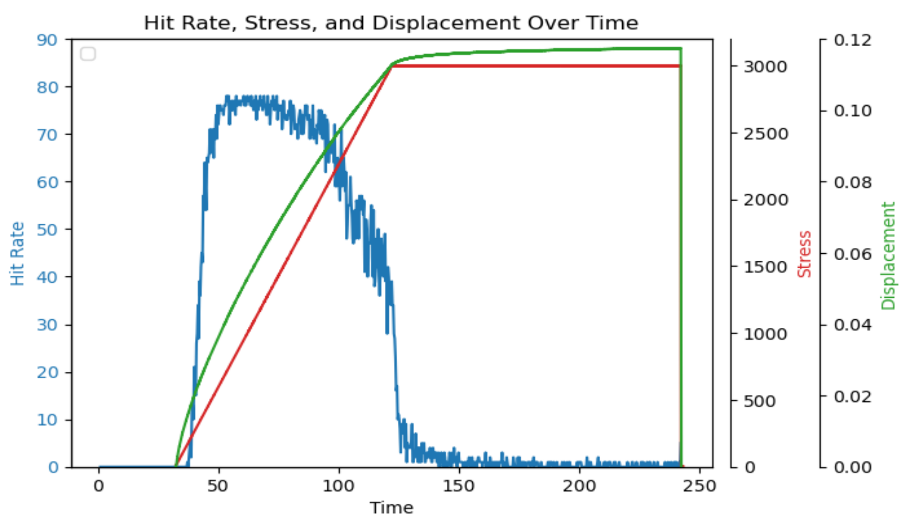

Figure 3.11: AE hit rate, applied stress, and displacement with respect to time during the crush test of petroleum coke-based proppant of size 35/60.

Figure 3.12 and Figure 3.13 illustrate stress, strain, and Acoustic Emission (AE) hit count response of LDC proppants with 10/35 mesh and 35/60 mesh sizes, respectively, over time. By correlating the AE hit count with the stress profile, it was determined that the packing strength of the LDC 10/35 mesh proppant is approximately 3800 psi, while the packing strength for the LDC 35/60 mesh proppant is approximately 6000 psi.

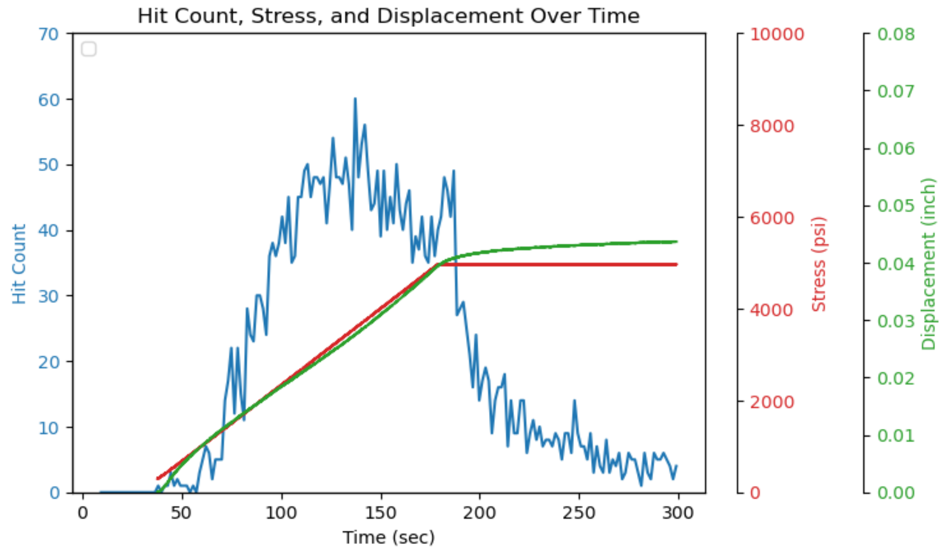

Figure 3.12: AE hit count, applied stress, and displacement with respect to time during the crush test of low-density ceramic (LDC) proppant of size 10/35.

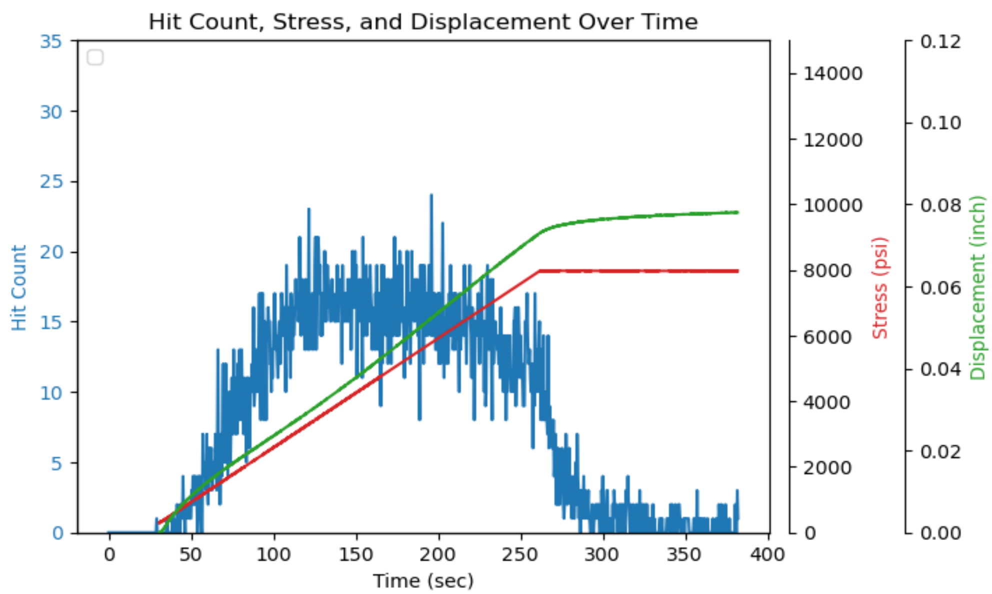

Figure 3.13: AE hit count, applied stress, and displacement with respect to time during the crush test of LDC proppant of size 35/60.

Similarly, Figure 3.14 and Figure 3.15 present the stress, strain, and AE hit count response of RC proppants with 10/35 mesh and 35/60 mesh sizes, respectively, over time. The AE hit response, when aligned with the stress profile, indicates that the packing strength of the RC 10/35 mesh proppant is approximately 10,000 psi, while the RC 35/60 mesh proppant exhibits a packing strength of approximately 12,500 psi.

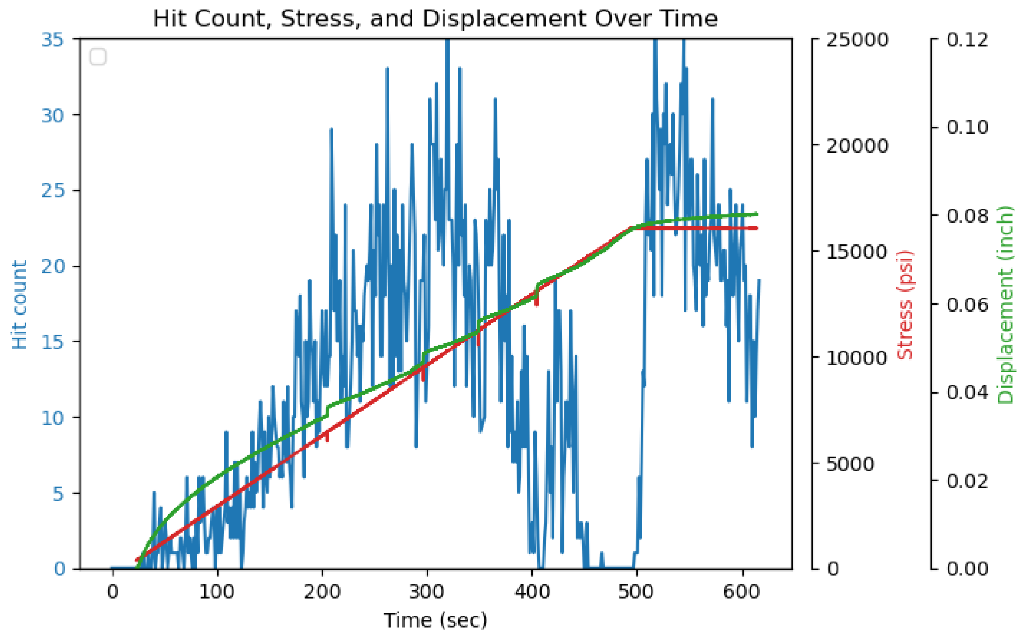

Figure 3.14: AE hit count, applied stress, and displacement with respect to time during the crush test of RC proppant of size 10/35.

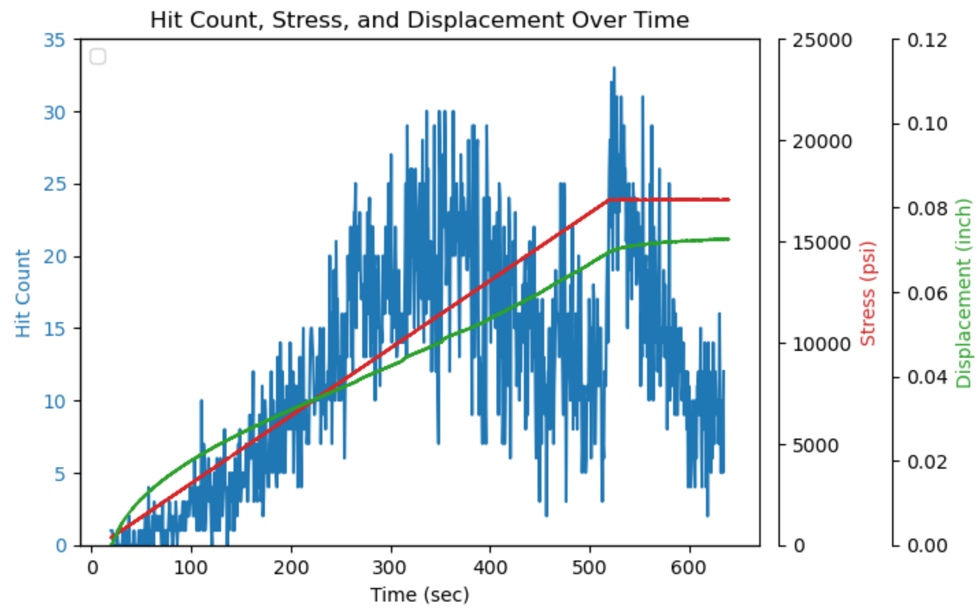

Figure 3.15: AE hit count, applied stress, and displacement with respect to time during the crush test of RC proppant of size 35/60.

Table 3-5 presents the crush resistance results for different proppants, focusing on their K-values, packing strengths, and the percentage of fines generated at the K-value. The K-value is a crucial measure that indicates the highest stress a proppant can withstand while producing less than 10% crushed fines. This parameter is key to understanding the durability and effectiveness of proppants under high-pressure conditions. The petroleum coke-based proppant (PC) is shown to be the weakest among the tested materials. For the 10/35 mesh size, the PC proppant has a packing strength of 2000 psi and a K-value of 2K, with 6.67% fines generated at this stress level. The 35/60 mesh size also exhibits a low packing strength of 1500 psi, with the same K-value of 2K, but with a slightly higher fines generation of 8.90%. These results suggest that PC proppants have limited capacity to withstand high pressures, making them less suitable for higher depth reservoir applications.

In contrast, the high-transported ultra-low density ceramic proppant (LDC) displays significantly higher strength and resistance. The 10/35 mesh size has a packing strength of 3800 psi and a K-value of 4K, and for the 35/60 mesh size, the packing strength is 6000 psi, and the K-value rises to 7K. These figures indicate that LDC proppants are much more robust compared to PC, making them better suited for environments with higher stress levels, and smaller size can withhold high stress.

The resin-coated ceramic proppant (RC) emerges as the strongest proppant tested. The 10/35 mesh size has an impressive packing strength of 10000 psi and a K-value of 15K. The 35/60 mesh size further increases in strength, with a packing strength of 12500 psi and a K-value of 17K. These results highlight the superior crush resistance of RC proppants, particularly in the finer 35/60 mesh size, making them ideal for extreme pressure environments such as high-stress hydraulic fracturing operations. This information is vital for selecting the appropriate proppant for specific applications, particularly in scenarios where high pressure and minimal fines generation are critical.

Table 3-5: K-value, packing strength, and percentage of fines generated at K-value for all types of proppants.

Proppant Type	Sizes	Packing strength (psi)	K-value	Fine generates at K-value (%)
PC	10_35	2000	2K	6.67
	35_60	1500	2K	8.90
LDC	10_35	3800	4K	7.77
	35_60	6000	7K	9.7
RC	10_35	10000	15K	7.5
	35_60	12500	17K	9.03

3.5.2 Heated test results:

All three types of proppants were being tested after been exposed to high temperature (300 C) for 7 days and 14 days, separately. In the wet test, the noise level is relatively lower than in the dry test. The data were filtered within the range of 60dB to 100dB, considering amplitude values lower than 60dB as noise. Figures 14 and 15 present the results of the crush tests conducted on petroleum-coke based proppants of sizes 10/35 and 35/60 that were exposed to heat for 7 and 14 days. For the 10/35 mesh proppants, the packing strength after 7 days of heat exposure was estimated at 1950 psi, decreasing to 1700 psi after 14 days, as shown in Figure 3.16. Similarly, for the 35/60 mesh proppants, the packing strength was 1550 psi after 7 days and reduced to 1250 psi after 14 days, as depicted in Figure 3.17.

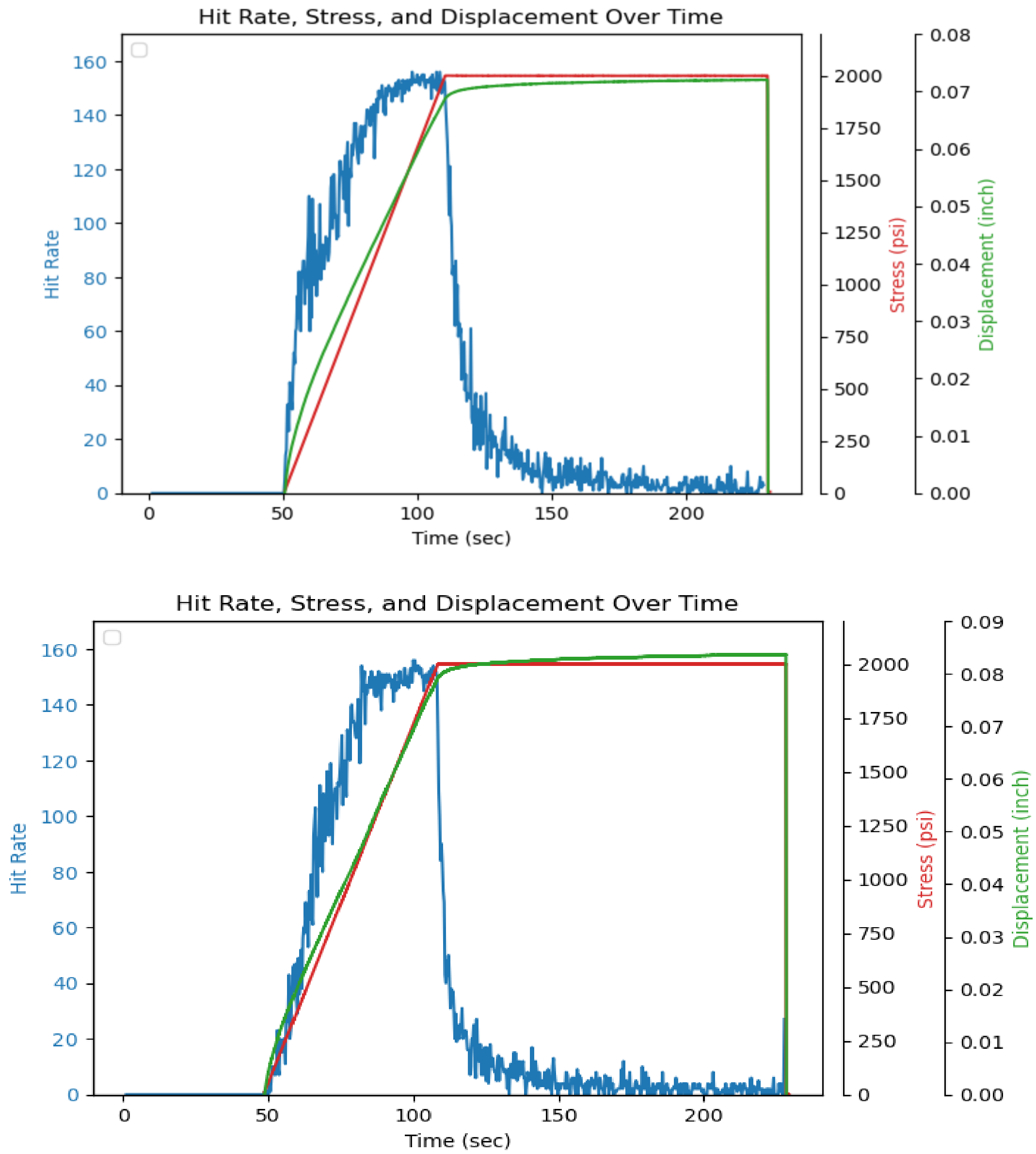

Figure 3.16: AE hit count, applied stress, and displacement with respect to time during the crush test of petroleum coke-based proppant of size 10/35 after being exposed to high temperature for 7 days (upper plot) and 14 days (lower plot).

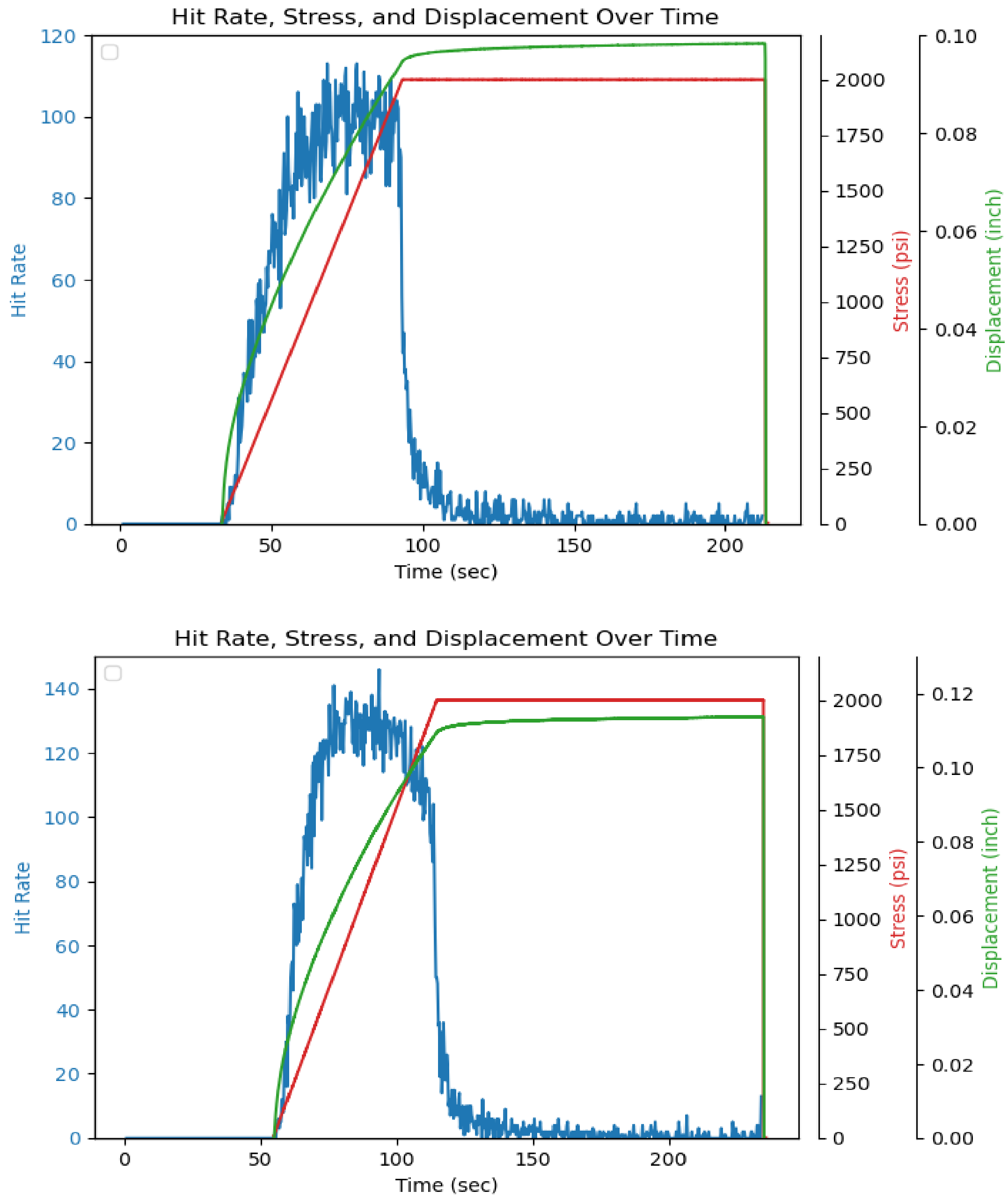

Figure 3.17: AE hit count, applied stress, and displacement with respect to time during the crush test of petroleum coke-based proppant of size 35/60 after being exposed to high temperature for 7days (upper) and 14 days (lower plot).

Figure 3.18 and Figure 3.19 display the results for the LDC proppants under the same conditions. For the 10/35 mesh LDC proppants, the packing strength was estimated at 3900 psi after 7 days of heat exposure, slightly decreasing to 3700 psi after 14 days, as shown in Figure 16. The 35/60 mesh LDC proppants exhibited packing strengths of 4500 psi and 3400 psi after 7 and 14 days of heat exposure, respectively, as illustrated in Figure 17.

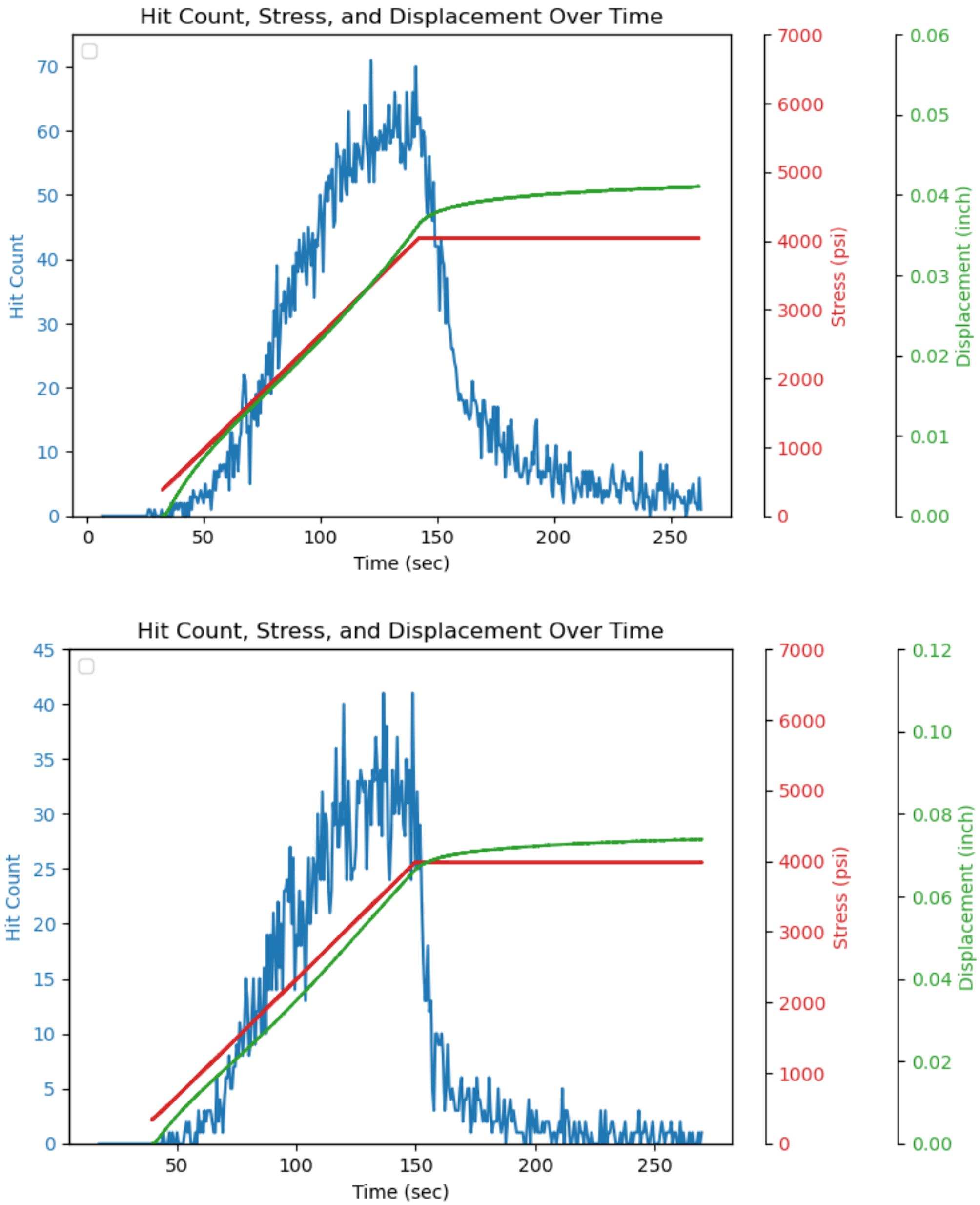

Figure 3.18: AE hit count, applied stress, and displacement with respect to time during the crush test of LDC proppant of size 10/35 after being exposed to high temperature for 7 days (upper one) and 14 days (lower one).

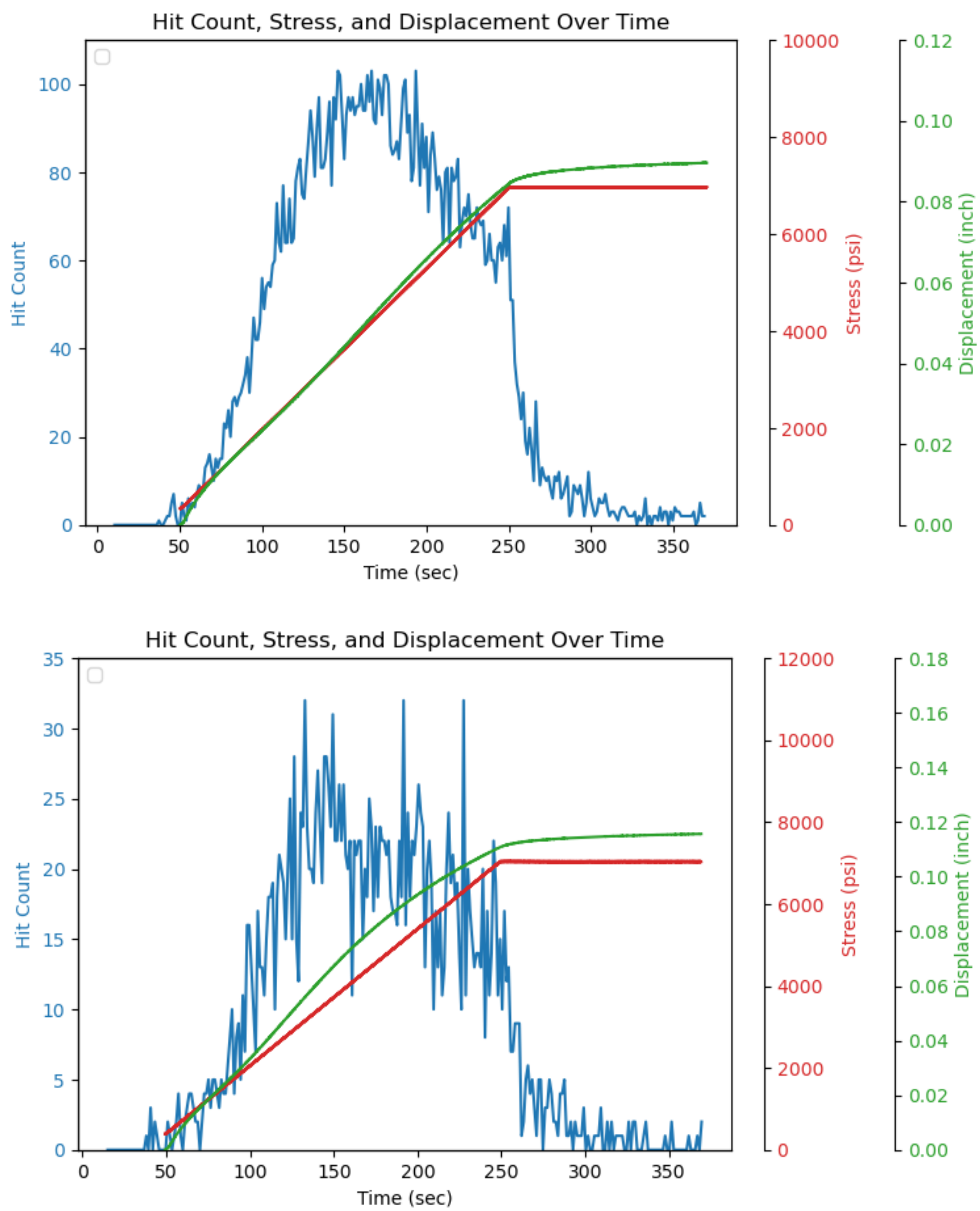

Figure 3.19: AE hit count, applied stress, and displacement with respect to time during the crush test of LDC proppant of size 35/60 after being exposed to high temperature for 7 days (upper one) and 14 days (lower one).

Figure 3.20 and Figure 3.21 show the results for the RC proppants. The packing strength for the 10/35 mesh RC proppants was 7800 psi after 7 days of heat exposure and slightly decreased to 7500 psi after 14 days, as demonstrated in Figure 3.20. For the 35/60 mesh RC proppants, the packing strength was estimated at 9000 psi after 7 days and decreased to 8000 psi after 14 days, as shown in Figure 3.21. These results indicate a general trend of decreasing packing strength with prolonged heat exposure across all proppant types and sizes, with RC proppants consistently demonstrating the highest packing strength.

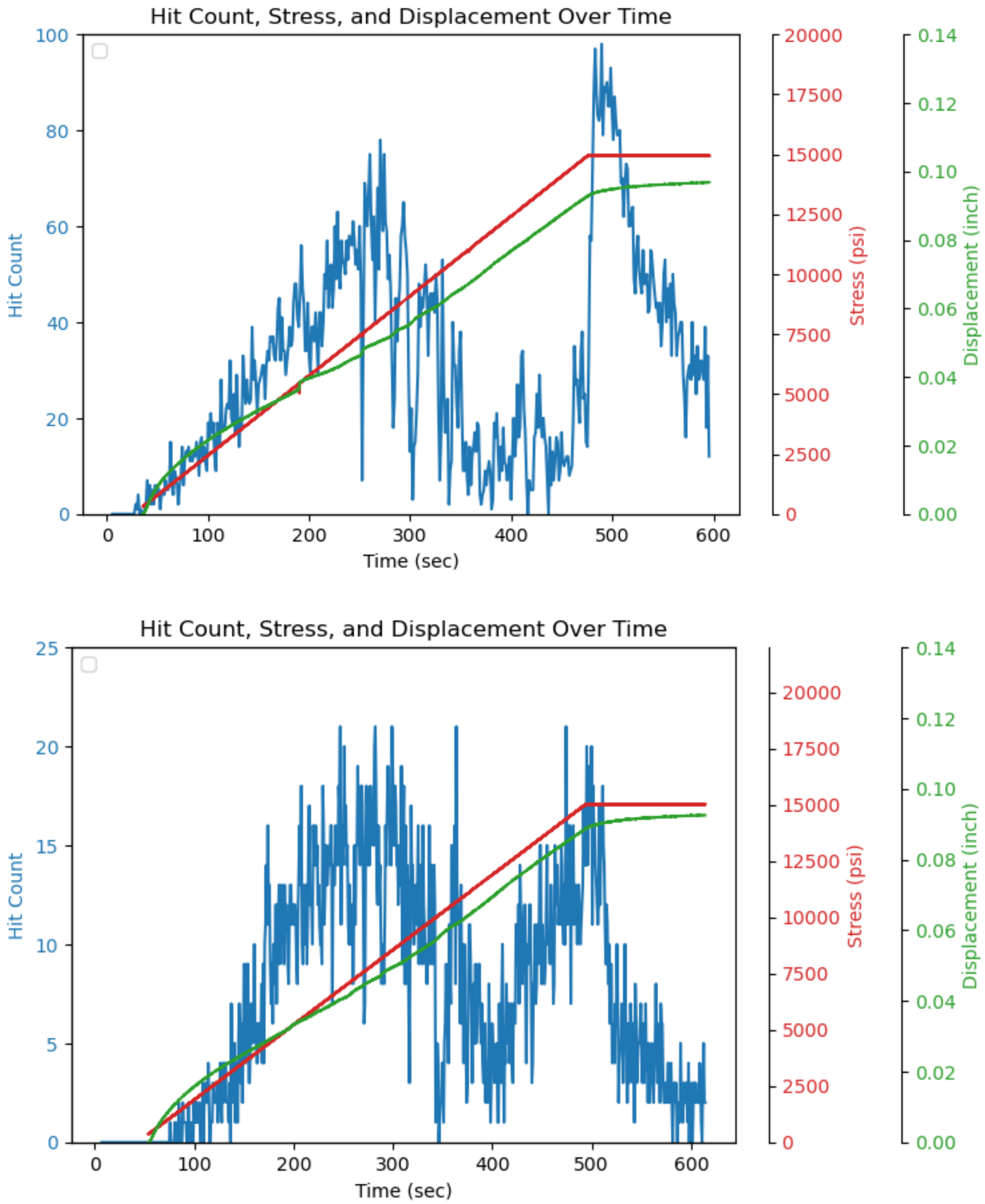

Figure 3.20: AE hit count, applied stress, and displacement with respect to time during the crush test of RC proppant of size 10/35 after being exposed to high temperature for 7 days (upper one) and 14 days (lower one).

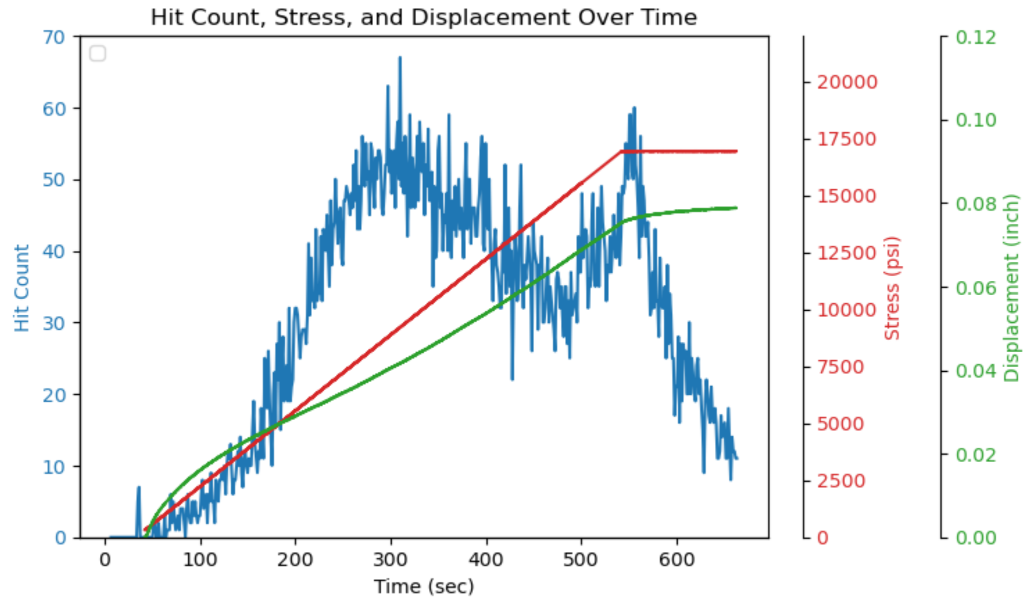

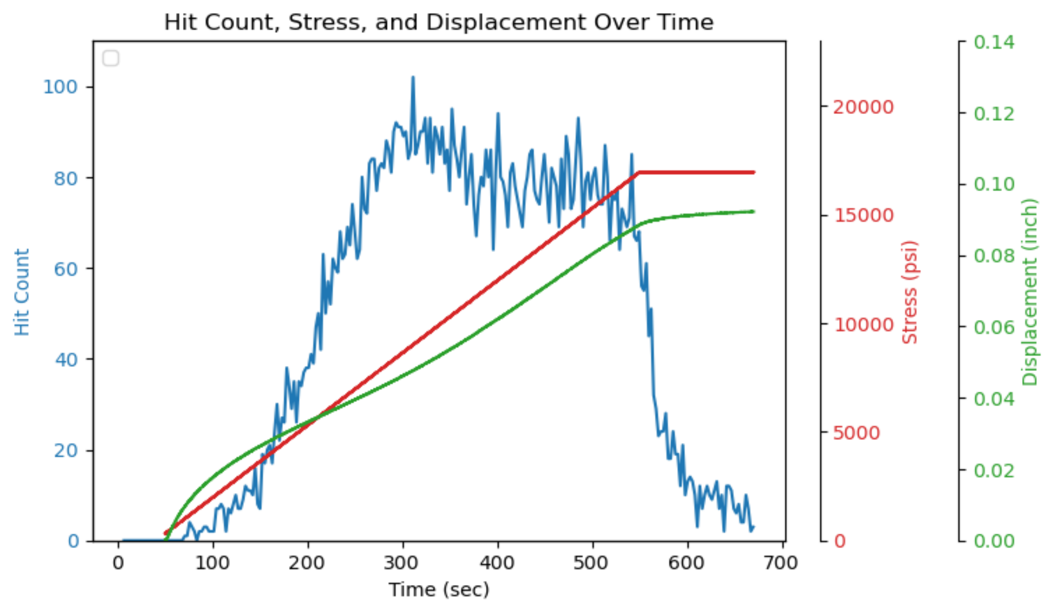

Figure 3.21: AE hit count, applied stress, and displacement with respect to time during the crush test of RC proppant of size 35/60 after being exposed to high temperature for 7 days (upper one) and 14 days (lower one).

Figure 3.22 and Figure 3.23 illustrate the percentage of fines generated for proppants of sizes 10/35 and 35/60, respectively, after being exposed to high temperatures for 0, 7, and 14 days. The data clearly indicates that the longer the proppants were subjected to heat, the more their structural integrity was compromised, leading to an increase in the percentage of fines.

For the petroleum coke (PC) proppants, as shown in the plot, the percentage of fines generated remained relatively stable, with values of 6.67%, 7.88%, and 8.23% for the 10/35 size after 0, 7, and 14 days of heat exposure, respectively. The 35/60 size PC proppants also showed minimal change, with fines percentages of 8.90%, 9.00%, and 11.10% across the same time periods. This minimal variation suggests that PC proppants have relatively consistent performance under heat exposure, though they are inherently weaker compared to other proppants.

In contrast, the LDC and RC proppants exhibited significant increases in fines generation with prolonged heat exposure, indicating a substantial loss in strength. For the LDC proppants, the 10/35 size showed fines percentages of 7.77%, 23.34%, and 28.25%, while the 35/60 size showed 9.70%, 21.62%, and 27.26% fines for 0, 7, and 14 days, respectively. This dramatic increase highlights the sensitivity of LDC proppants to high temperatures, particularly for longer exposure durations.

The RC proppants were even more affected by heat exposure. The 10/35 size proppants showed fines percentages of 7.50%, 28.47%, and 38.04%, while the 35/60 size recorded 9.03%, 15.36%, and 19.28% fines after 0, 7, and 14 days, respectively. The significant increase in fines, especially for the 10/35 size, demonstrates that RC proppants, despite their initial strength, experience considerable degradation when exposed to prolonged high temperatures.

Overall, these plots emphasize the impact of heat exposure on proppant strength, with RC proppants showing the most significant degradation, followed by LDC, and PC proppants demonstrating the least change, albeit from a lower initial strength baseline.

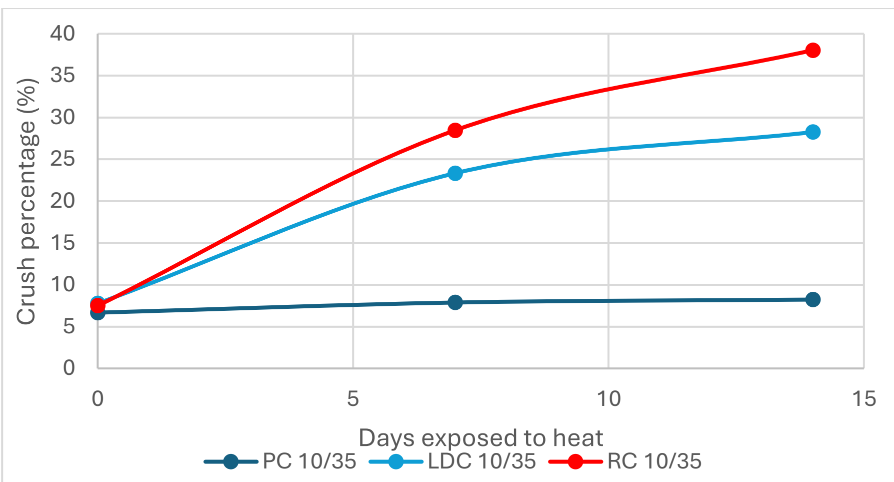

Figure 3.22: the percentage of fines generated for proppants of sizes 10/35 after being exposed to high temperatures for 0, 7, and 14 days.

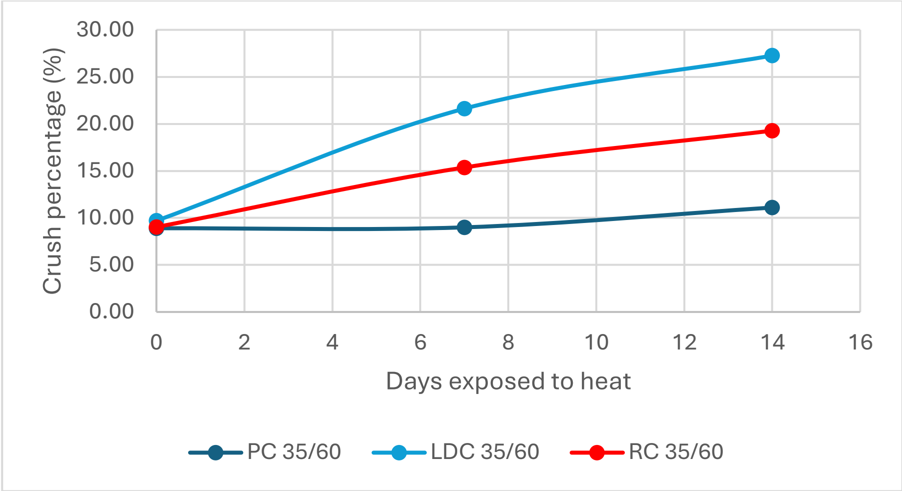

Figure 3.23: the percentage of fines generated for proppants of sizes 10/35 after being exposed to high temperatures for 0, 7, and 14 days.

3.5.3 Mixed test results:

From the above results, it's clear that PC has very low strength as 2000 psi, on the other hand RC has high strength as 17000 psi. But the price of RC or LDC is much higher compared to the PC price, and in real field tons of proppants need to inject to keep the fracture open. To efficiently select proppants, we tried mixing LDC in PC, and RC in PC at different ratio to enhance their strength and make the proppant injection economically viable. The displacement curve is a crucial indicator in assessing the performance of proppants in hydraulic fracturing. It provides insights into how well a proppant can tolerate load during the fracturing process. Specifically, a lower displacement on the curve suggests that the proppant is less likely to compact under stress. This lower compaction translates to higher fracture conductivity, as the proppant remains more effective in maintaining open fractures and facilitating fluid flow. Figure 3.24 shows the how the proppant pack thickness changes with applied stress 5000 psi final stress at 2000 psi/min loading rate for different mixing ratio of PC with LDC. The plot shows that increasing the LDC content reduces the displacement, reflecting better performance in withstanding stress. The stress-strain curve on the left plot for the 50% PC - 50% LDC of 10/35 mesh size mixture demonstrates a clear reduction in compaction compared to 100% PC, but it is not as effective as the RC mix. On the right plot, the reduction in displacement is more apparent as LDC content increases. The plot indicates that the 25% PC - 75% LDC mix is particularly effective in minimizing displacement, suggesting strong reinforcement by LDC at this ratio.

The RC mixtures demonstrate a more pronounced reduction in net displacement compared to the LDC mixes. Figure 3.25 shows that even after mixing 25% RC with 75 % PC has greatly reduced the compaction compared to the 100% PC. This indicates a significant improvement in the mechanical strength of the proppant pack when mixed with RC.

Figure 3.26 illustrates the relationship between the percentage of proppant concentration (PC) and the percentage of fines generated. The plot reveals that the fines generated remain nearly constant across various mixing ratios for the 10/35 PC and LDC combinations. This stability in fines generation is attributed to the fact that both LDC and 10/35 PC have K-values (4k and 2k, respectively) that are lower than the applied stress of 5000 psi.

For all other cases, the crush percentage generated decreases significantly as the percentage of LDC or RC in the mixture increases. This indicates that incorporating LDC or RC into the PC mixture substantially reduces fines generation and enhances the proppant's resistance to compaction, leading to improved fracture conductivity and efficiency.

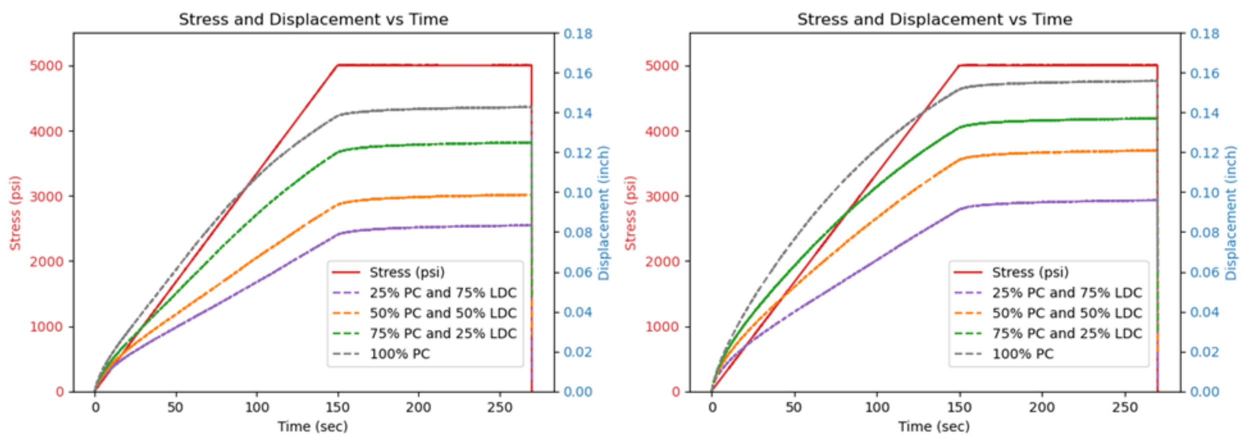

Figure 3.24: The stress and displacement response with respect to time for different mixing ratio of PC and LDC. The left figure shows the results for 10/35 mesh sizes and the right plot shows the results for 35/60 mesh sizes.

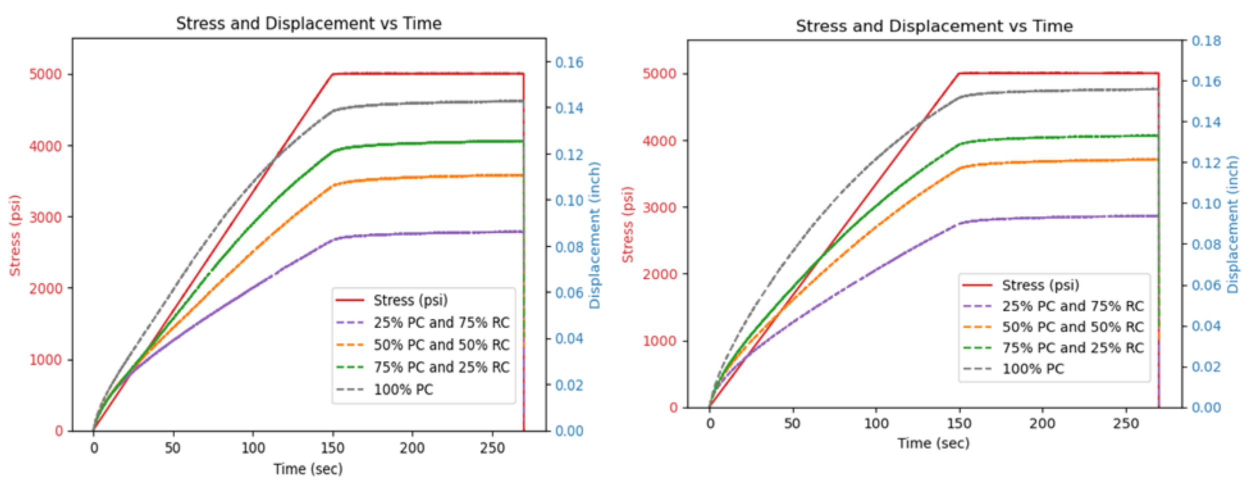

Figure 3.25: The stress and displacement response with respect to time for different mixing ratio of PC and RC. The left figure shows the results for 10/35 mesh sizes and the right plot shows the results for 35/60 mesh sizes.

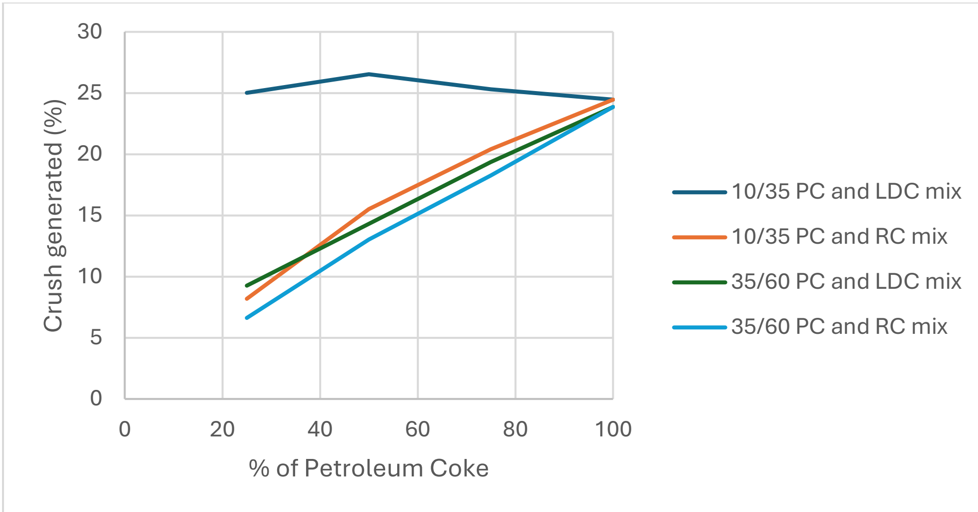

Figure 3.26: Crush generated with respect to the percentage of PC in the mixture, 5000 psi stress was applied in all mixture.

3.6 SEM image analysis of heated proppants:

Scanning Electron Microscopy (SEM) is an imaging method used to examine surfaces and near-surface areas of solid specimens. It works by exploiting different interactions, including elastic and inelastic scattering, between an electron beam and the specimen's surface (Stachowiak, G., & Batchelor, A. W. (2004)). In our study, we analyzed the surface of intact proppants and the surface of proppants that were exposed to high temperatures (300C) for 7, 14, and 30 days separately. SEM image was able to show the changes has taken place in the surface of proppant after being exposed to heat. Figure Figure 3.27 to Figure 3.34 shows the changes that were taken place on the surface of the proppants as they were exposed to high temperatures (300C) for 7, 14, and 30 days separately. From all the SEM images, it's clear that ceramic proppants undergo through degradation, and it's related to the duration of high temperatures exposure.

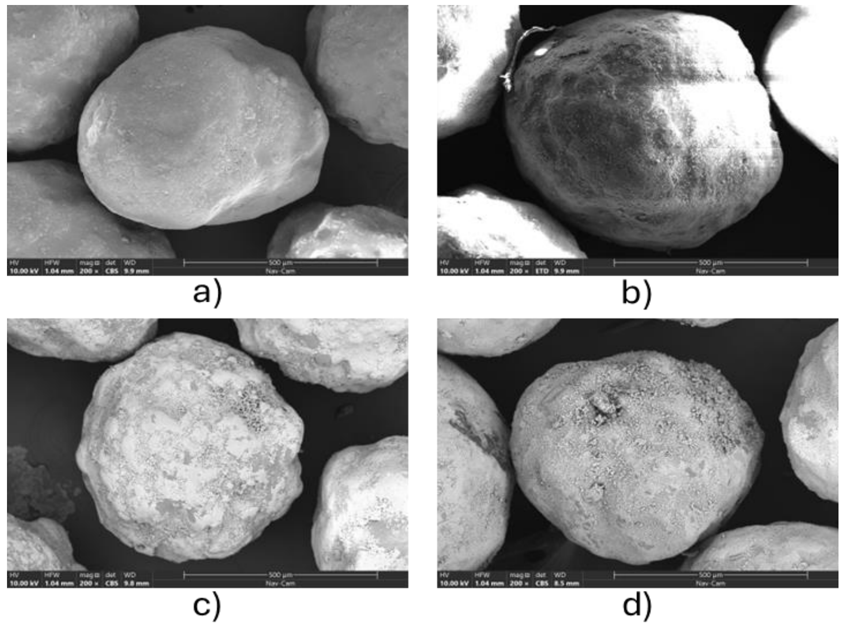

Figure 3.27: SEM images of LDC 10/35 proppants at 200x magnification. (a) Surface morphology of intact proppants, showing a smooth and unaltered structure. (b), (c), and (d) shows the surface of proppants that were exposed to heat for 7 days, 15 days, and 30 days, showing significant degradation with visible fractures and more pronounced surface roughness.

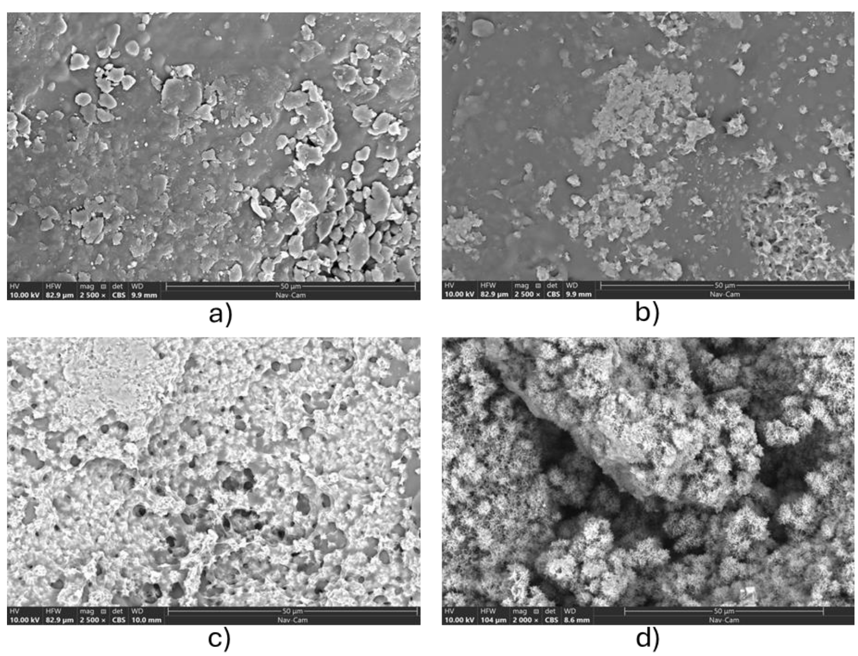

Figure 3.28: SEM images of LDC proppants at 2000x magnification for clear inspection. (a) Surface morphology of intact proppants, showing a smooth and unaltered structure. (b) Proppants exposed to heat for 7 days, (c) Proppants exposed to heat for 15 days, (d) Proppants exposed to heat for 30 days, showing significant degradation with visible fractures.

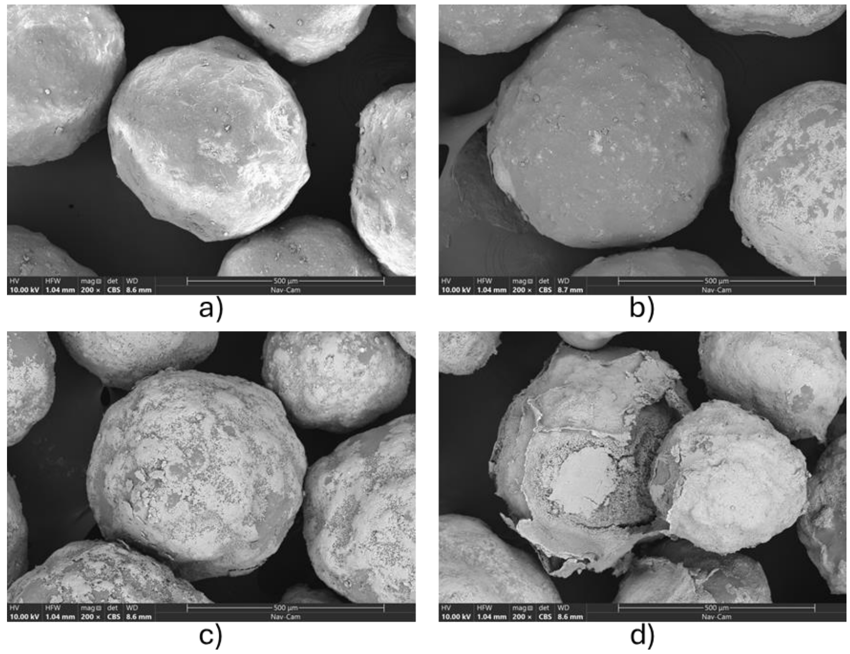

Figure 3.29: SEM images of LDC 35/60 proppants at 200x magnification. (a) Surface morphology of intact proppants, showing a smooth and unaltered structure. (b), (c), and (d) show the surface of proppants that were exposed to heat for 7 days, 15 days, and 30 days, respectively showing significant degradation with visible fractures and more surface roughness.

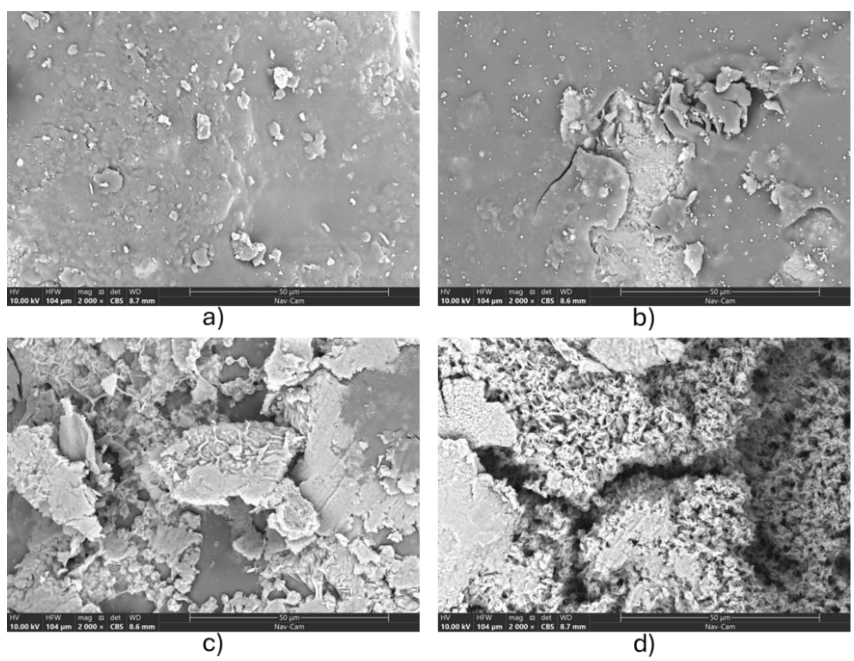

Figure 3.30: SEM images of LDC 35/60 proppants at 2000x magnification. (a) Surface morphology of intact proppants, showing a smooth and unaltered structure. (b), (c), and (d) show the surface of proppants that were exposed to heat for 7 days, 15 days, and 30 days, respectively showing significant degradation with visible fractures.

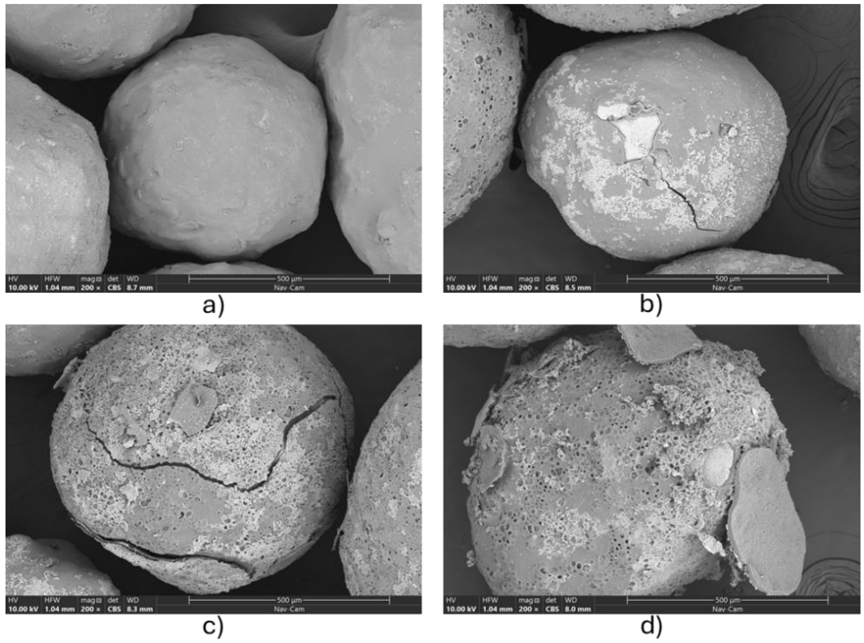

Figure 3.31: SEM images of RC 10/35 proppants at 200x magnification. (a) Surface morphology of intact proppants, showing a smooth and unaltered structure. (b), (c), and (d) show the surface of proppants that were exposed to heat for 7 days, 15 days, and 30 days, respectively showing significant degradation of coating surface.

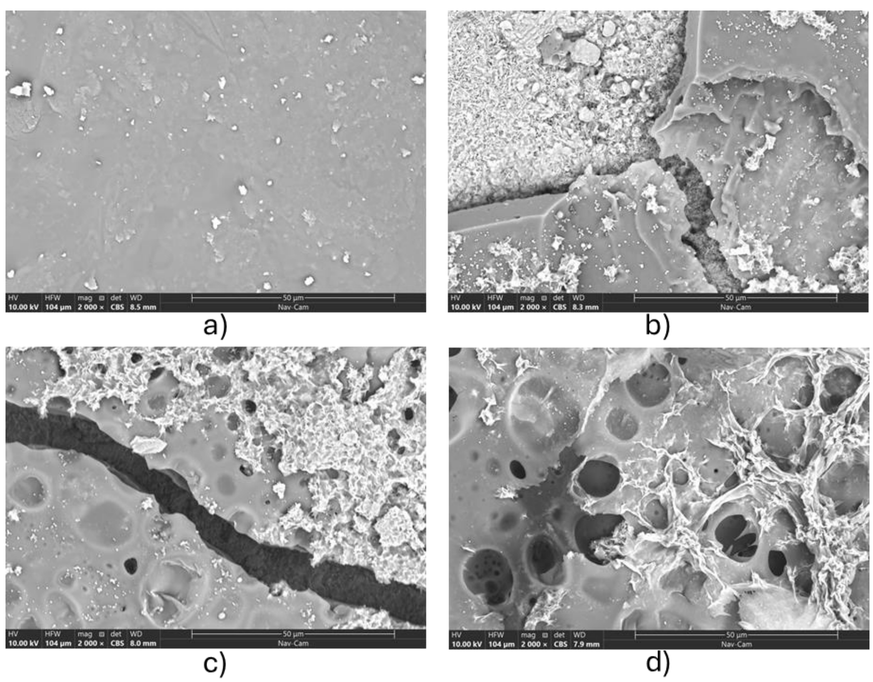

Figure 3.32: SEM images of RC 10/35 proppants at 2000x magnification. (a) Surface morphology of intact proppants, showing a smooth and unaltered structure. (b), (c), and (d) shows the surface of proppants that were exposed to heat for 7 days, 15 days, and 30 days, respectively showing significant degradation of coating surface.

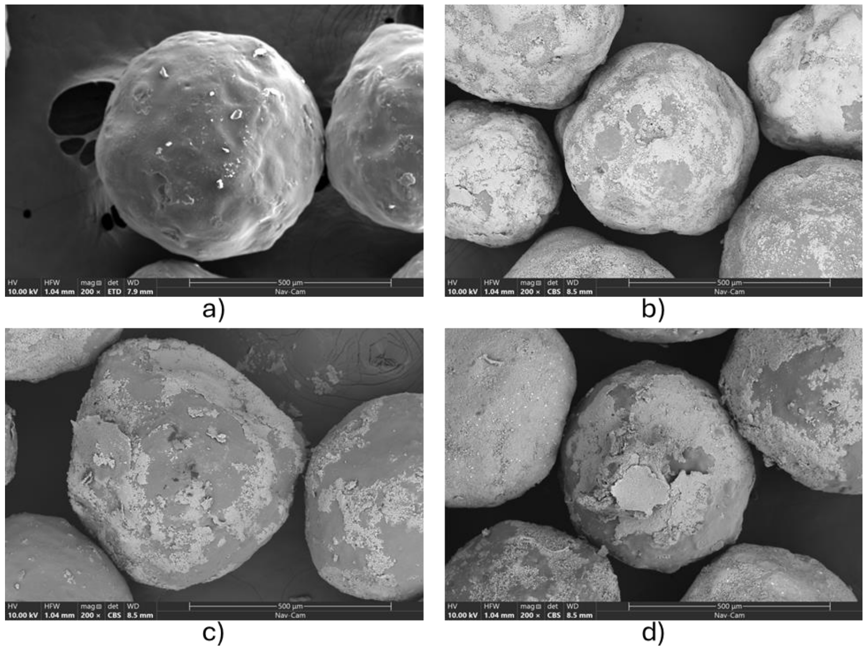

Figure 3.33: SEM images of RC 35/60 proppants at 200x magnification. (a) Surface morphology of intact proppants, showing a smooth and unaltered structure. (b), (c), and (d) show the surface of proppants that were exposed to heat for 7 days, 15 days, and 30 days, respectively showing significant degradation of coating surface.

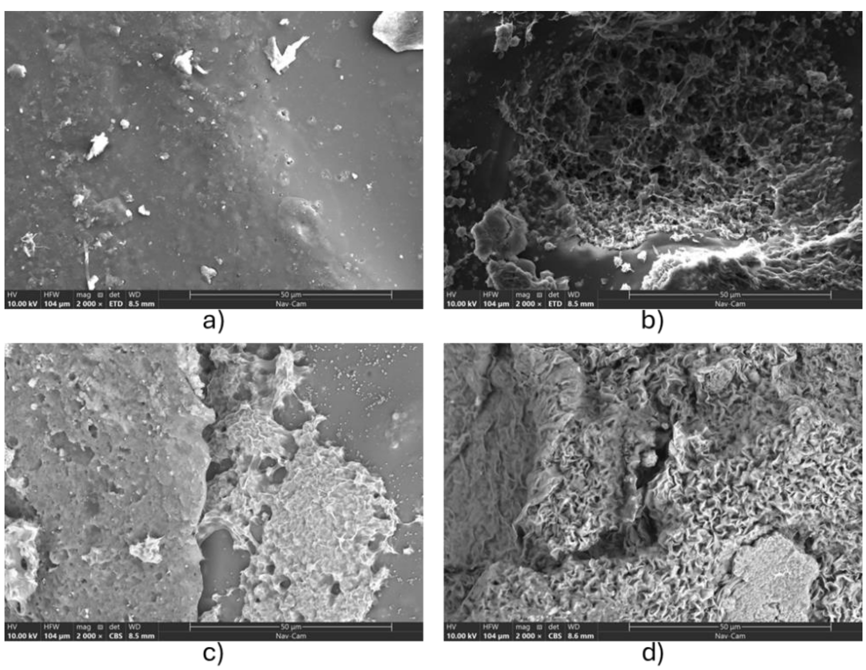

Figure 3.34: SEM images of RC 35/60 proppants at 200x magnification. (a) Surface morphology of intact proppants, showing a smooth and unaltered structure. (b), (c), and (d) shows the surface of proppants that were exposed to heat for 7 days, 15 days, and 30 days, respectively showing significant degradation of coating surface.

Chapter 4 Conclusions

Employing a comprehensive modeling approach, the investigation explores various factors influencing fracture behavior, including fluid viscosity, leak-off, perforation friction, and rock anisotropy. By examining the near-tip region of fluid-driven semi-infinite fractures, there are distinct fracture propagation regimes governed by toughness, leak-off, and viscosity. Vertex solutions provide the fracture aperture in these regimes, offering insights into the distribution of injected fluid volume and dissipated energy. Furthermore, transition distances delineate the shift between dominant mechanisms as the fracture evolves. Numerical simulations elucidate the impact of parameters such as fluid viscosity on the fracture propagation and propagation regime. The study examined how fluid viscosity, perforation density, and fluid leak-off coefficient influence fracture propagation characteristics in hydraulic fracturing operations. It was found that high-viscosity fluid injections tend to promote fracture propagation within a viscous regime, while low-viscosity fluid injection facilitates a toughness-dominated regime. By varying the number of perforations per cluster, the impact of perforation density on fracture propagation was further evaluated. The findings reveal that a higher perforation count per cluster significantly reduces its influence on fluid distribution within a multi-cluster fracture system. In these cases, flow partitioning is predominantly governed by stress shadow effects, rather than by perforation friction. Conversely, when there are fewer perforations per cluster, flow partitioning is primarily determined by perforation friction, with minimal influence from stress shadow effects. This indicates that stress shadowing has a negligible effect on flow partitioning under conditions of low perforation density.

Additionally, the study explored the role of fluid leak-off on fracture propagation. The results indicate that the leak-off coefficient is a critical parameter in controlling the rate at which fracture aperture decreases. The impact of fluid leak-off on fracture behavior is also investigated, showing that higher leak-off coefficients impede fracture growth due to increased fluid dissipation. A higher leak-off coefficient results in a more rapid closure of fractures due to accelerated fluid loss from the fracture into the surrounding formation. This finding underscores the importance of carefully managing the leak-off coefficient to optimize fracture aperture and maintain desired fracture conductivity over time. Together, these results provide insights into how fracture propagation behavior can be tailored through careful control of fluid viscosity, perforation density, and fluid leak-off properties in hydraulic fracturing processes. The Results highlight the interplay between these factors and the fracture growth, demonstrating how variations in parameters influence fracture dimensions, pressure distribution, and stress shadowing effects.

Furthermore, the study analyzed the impact of stress barriers on fracture height growth, considering cases with both symmetric and asymmetric stress barriers. The results demonstrate that a higher stress barrier effectively restricts vertical fracture propagation, resulting in longer lateral fracture growth compared to scenarios with lower stress barriers. In cases of asymmetric stress barriers, fracture growth in the vertical direction was observed to be uneven, attributed to the differential stress levels on either side of the fracture. This uneven growth shows how non-uniform stress barriers affect fracture shape, emphasizing the need to consider vertical stress differences in fracture design. These insights on stress barriers complement the understanding of fracture dynamics, aiding in the development of more precise and efficient hydraulic fracturing strategies for various geological conditions.

This experimental study provides a comprehensive evaluation of the mechanical properties of various proppants under simulated downhole conditions. The findings demonstrate that while PC proppants are economically advantageous, they exhibit lower strength compared to ceramic-based alternatives. Among the ceramic proppants, RC proppants showed superior stress tolerance.

Temperature has a significant impact on proppant performance. The crush resistance and packing strength of all proppants decreased with rising temperatures; however, the extent of degradation was notably different between proppant types. PC proppants retained their strength even after exposure to high temperatures, whereas ceramic-based proppants experienced a substantial reduction in strength. The results underscore the importance of selecting appropriate proppants based on both economic considerations and performance requirements. For applications involving high temperatures, such as in geothermal systems, PC proppants might offer a more stable and cost-effective solution compared to ceramic proppants, which show more significant strength reduction under similar conditions. Further research and field testing are recommended to optimize proppant selection and mixing strategies for enhanced efficiency and cost-effectiveness in various fracturing scenarios

The SEM-EDX analysis of the proppants before and after heat exposure displayed noticeable changes in the surface structure. Microcracks were more prevalent in the proppant exposed to heat, and the presence of gas release pores was observed, suggesting potential alterations in the proppant's properties due to high-temperature conditions. The findings will contribute to the selection and optimization of proppant materials for efficient and sustainable development of unconventional oil and gas reservoirs, as well as geothermal fields.

Reference:

Abou-Sayed, A. S., Andrews, D. E., & Buhidma, I. M. (2007). *Evaluation of Oily Waste Injection Below the Permafrost in Prudhoe Bay Field*. https://doi.org/10.2523/18757-ms

Adachi, J. I., Detournay, E., & Peirce, A. P. (2010). Analysis of the classical pseudo-3D model for hydraulic fracture with equilibrium height growth across stress barriers. *International Journal of Rock Mechanics and Mining Sciences*, *47*(4). https://doi.org/10.1016/j.ijrmms.2010.03.008

Adachi, J., Siebrits, E., Peirce, A., & Desroches, J. (2007). Computer simulation of hydraulic fractures. *International Journal of Rock Mechanics and Mining Sciences*, *44*(5). https://doi.org/10.1016/j.ijrmms.2006.11.006

Ali Daneshy, A., & Services, H. (n.d.). *Experimental Investigation of Hydraulic Fracturing Through Perforations*.

Bandara, K. M. A. S., Ranjith, P. G., Rathnaweera, T. D., Wanniarachchi, W. A. M., & Yang, S. Q. (2021). Crushing and embedment of proppant packs under cyclic loading: An insight to enhanced unconventional oil/gas recovery. *Geoscience Frontiers*, *12*(6). https://doi.org/10.1016/j.gsf.2020.02.017

Barenblatt, G. I. (1962). The Mathematical Theory of Equilibrium Cracks in Brittle Fracture. *Advances in Applied Mechanics*, *7*(C). https://doi.org/10.1016/S0065-2156(08)70121-2

Barnett, D. M., & Asaro, R. J. (1972). The fracture mechanics of slit-like cracks in anisotropic elastic media. *Journal of the Mechanics and Physics of Solids*, *20*(6). https://doi.org/10.1016/0022-5096(72)90013-0

Batchelor, G. K., & Young, A. D. (1968). An Introduction to Fluid Mechanics . *Journal of Applied Mechanics*, *35*(3). https://doi.org/10.1115/1.3601282

Brown, D. (2000). A Hot Dry Rock Geothermal Energy Concept Utilizing Supercritical Co2 Instead of Water. *Twenty-Fifth Workshop on Geothermal Resevoir Engineering*, *1995*(April 1992).

Carbonell, R., Desroches, J., & Detournay, E. (1999). A comparison between a semi-analytical and a numerical solution of a two-dimensional hydraulic fracture. *International Journal of Solids and Structures*, *36*(31–32). https://doi.org/10.1016/S0020-7683(98)00269-8

Chang, J.-H., & Liao, G.-J. (2014). Nonhomogenized Displacement Discontinuity Method for Calculation of Stress Intensity Factors for Cracks in Anisotropic FGMs. *Journal of Engineering Mechanics*, *140*(12). https://doi.org/10.1061/(asce)em.1943-7889.0000799

Cipolla, C. L. (2009). Modeling production and evaluating fracture performance in unconventional gas reservoirs. *JPT, Journal of Petroleum Technology*, *61*(9). https://doi.org/10.2118/118536-JPT

Crouch, S. L., Starfield, A. M., & Rizzo, F. J. (1983). Boundary Element Methods in Solid Mechanics. *Journal of Applied Mechanics*, *50*(3). https://doi.org/10.1115/1.3167130

Desroches, J., Detournay, B., Lenoach, E., Papanastasiou, P., Pearson, J. R. A., Thiercelin, M., & Cheng, A. (1994). The crack tip region in hydraulic fracturing. *Proceedings - Royal Society of London, A*, *447*(1929). https://doi.org/10.1098/rspa.1994.0127

Detournay, E. (2004). Propagation Regimes of Fluid-Driven Fractures in Impermeable Rocks. *International Journal of Geomechanics*, *4*(1). https://doi.org/10.1061/(asce)1532-3641(2004)4:1(35)

Dontsov, E. V., & Peirce, A. P. (2015). An enhanced pseudo-3D model for hydraulic fracturing accounting for viscous height growth, non-local elasticity, and lateral toughness. *Engineering Fracture Mechanics*, *142*, 116–139. https://doi.org/10.1016/j.engfracmech.2015.05.043

Dontsov, E. V., & Peirce, A. P. (2017). A multiscale Implicit Level Set Algorithm (ILSA) to model hydraulic fracture propagation incorporating combined viscous, toughness, and leak-off asymptotics. *Computer Methods in Applied Mechanics and Engineering*, *313*, 53–84. https://doi.org/10.1016/j.cma.2016.09.017

Elbel, J. L., Piggott, A. R., Mack, M. G., & Schlumberger, D. (1992). *SPE Numerical Modeling of Multilayer Fracture Treatments*.

Fung, R. L., Vijayakumar, S., & Cormack, D. E. (1987). CALCULATION OF VERTICAL FRACTURE CONTAINMENT IN LAYERED FORMATIONS. *SPE Formation Evaluation*, *2*(4). https://doi.org/10.2118/14707-PA

Ghassemi, A., Tarasovs, S., & Cheng, A. H. D. (2005). Integral equation solution of heat extraction-induced thermal stress in enhanced geothermal reservoirs. *International Journal for Numerical and Analytical Methods in Geomechanics*, *29*(8), 829–844. https://doi.org/10.1002/nag.440

Ghassemi, A., & Zhang, Z. (2019). Modeling Hydraulic Fracturing of Unconventional Reservoirs. In *Geophysical Monograph Series* (Vol. 245). https://doi.org/10.1002/9781119066699.ch12

Hari, S., Krishna, S., Gurrala, L. N., Singh, S., Ranjan, N., Vij, R. K., & Shah, S. N. (2021). Impact of reservoir, fracturing fluid and proppant characteristics on proppant crushing and embedment in sandstone formations. In *Journal of Natural Gas Science and Engineering* (Vol. 95). Elsevier B.V. https://doi.org/10.1016/j.jngse.2021.104187

Huerta, N. J., Cantrell, K. J., White, S. K., & Brown, C. F. (2020). Hydraulic fracturing to enhance injectivity and storage capacity of CO2 storage reservoirs: Benefits and risks. *International Journal of Greenhouse Gas Control*, *100*. https://doi.org/10.1016/j.ijggc.2020.103105

Jeffrey, R. G., & Mills, K. W. (2000). Hydraulic fracturing applied to inducing longwall coal mine goaf falls. *4th North American Rock Mechanics Symposium, NARMS 2000*.

Johnson, S. M., & Morris, J. P. (2009). Hydraulic fracturing mechanisms in carbon sequestration applications. *43rd U.S. Rock Mechanics Symposium and 4th U.S.-Canada Rock Mechanics Symposium*.

Ko, S., Ghassemi, A., & Uddenberg, M. (n.d.). *Selection and Testing of Proppants for EGS*.

Kresse, O., Cohen, C., Weng, X., Wu, R., & Gu, H. (2011). Numerical modeling of hydraulic fracturing in naturally fractured formations. *45th US Rock Mechanics / Geomechanics Symposium*.

Kresse, O., & Weng, X. (2018). Numerical Modeling of 3D Hydraulic Fractures Interaction in Complex Naturally Fractured Formations. *Rock Mechanics and Rock Engineering*, *51*(12). https://doi.org/10.1007/s00603-018-1539-5

Kresse, O., Weng, X., & Mohammadnejad, T. (2017). Modeling the effect of fracture interference on fracture height growth by coupling 3D displacement discontinuity method in hydraulic fracture simulator. *51st US Rock Mechanics / Geomechanics Symposium 2017*, *4*.

Kumar, D., & Ghassemi, A. (2016). A three-dimensional analysis of simultaneous and sequential fracturing of horizontal wells. *Journal of Petroleum Science and Engineering*, *146*, 1006–1025. https://doi.org/10.1016/j.petrol.2016.07.001

Lister, J. R. (1990). Buoyancy-driven fluid fracture: The effects of material toughness and of low-viscosity precursors. *Journal of Fluid Mechanics*, *210*(263). https://doi.org/10.1017/S0022112090001288

Liu, B., & Ghassemi, A. (2024). Simulation of Proppant Placement in Multiple Simultaneously Propagating Hydraulic Fractures in Horizontal Wells. *Rock Mechanics and Rock Engineering*. https://doi.org/10.1007/s00603-024-04022-1

Mcdaniel, B. W., & Services, H. (1986). *SPE SPE 15067 Conductivity Testing of Proppants at High Temperature and Stress*. http://onepetro.org/SPEWRM/proceedings-pdf/86CRM/All-86CRM/SPE-15067-MS/2029159/spe-15067-ms.pdf/1

Nordgren, R. P. (1972). *Propagation of a Vertical Hydraulic Fracture*. http://onepetro.org/spejournal/article-pdf/12/04/306/2691154/spe-3009-pa.pdf/1

Olson, J. E. (2004). Predicting fracture swarms - The influence of subcritical crack growth and the crack-tip process on joint spacing in rock. *Geological Society Special Publication*, *231*, 73–87. https://doi.org/10.1144/GSL.SP.2004.231.01.05

Olson, J. E. (2008). Multi-fracture propagation modeling: Applications to hydraulic fracturing in shales and tight gas sands. *42nd U.S. Rock Mechanics - 2nd U.S.-Canada Rock Mechanics Symposium*.

Palisch, T., Duenckel, R., Chapman, M., Woolfolk, S., Ceramics, C., & Vincent, M. C. (2010). *How To Use and Misuse Proppant Crush Tests: Exposing the Top 10 Myths*.

Schultz, R. A. (1988). Stress intensity factors for curved cracks obtained with the displacement discontinuity method. *International Journal of Fracture*, *37*(2). https://doi.org/10.1007/BF00041718

Sesetty, V., & Ghassemi, A. (2018). Effect of rock anisotropy on wellbore stresses and hydraulic fracture propagation. *International Journal of Rock Mechanics and Mining Sciences*, *112*, 369–384. https://doi.org/10.1016/j.ijrmms.2018.09.005

Sesetty, V., & Ghassemi, A. (2019). *SPE-194328-MS Simulation and Analysis of Fracture Swarms Observed in the Eagle Ford Field Experiment* (Vol. 2). http://onepetro.org/SPEHFTC/proceedings-pdf/19HFTC/1-19HFTC/D011S002R004/1143532/spe-194328-ms.pdf/1

Sesetty, V., Ghassemi, A., & Gil, I. (2018a). An integrated field and numerical study of the impact of formation anisotropy on stage spacing in horizontal wells. *SPE/AAPG/SEG Unconventional Resources Technology Conference 2018, URTC 2018*. https://doi.org/10.15530/urtec-2018-2878152

Sesetty, V., Ghassemi, A., & Gil, I. (2018b). An integrated field and numerical study of the impact of formation anisotropy on stage spacing in horizontal wells. *SPE/AAPG/SEG Unconventional Resources Technology Conference 2018, URTC 2018*. https://doi.org/10.15530/urtec-2018-2878152

Shou, K. J. (1993). A higher order three-dimensional displacement discontinuity method with application to bonded half-space problems. In *Dissertation*.

Shou, K. J., & Crouch, S. L. (1995). A higher order displacement discontinuity method for analysis of crack problems. *International Journal of Rock Mechanics and Mining Sciences And*, *32*(1). https://doi.org/10.1016/0148-9062(94)00016-V

Sih, G. C., Paris, P. C., & Erdogan, F. (1962). *Crack-Tip, Stress-Intensity Factors for Plane Extension and Plate Bending Problems Transactions of the AS ME*. http://asme.org/terms

Simo, H., Pournik, M., & Sondergeld, C. H. (n.d.). *SPE 164506 Proppant Crush Test: A New Approach*. http://onepetro.org/SPEOKOG/proceedings-pdf/13POS/All-13POS/SPE-164506-MS/1562137/spe-164506-ms.pdf/1

Simonson, E. R., Abou-Sayed, A. S., & Clifton, R. J. (1978). CONTAINMENT OF MASSIVE HYDRAULIC FRACTURES. *Soc Pet Eng AIME J*, *18*(1). https://doi.org/10.2118/6089-pa

Simonson Member, E. R., Abou-Sayed, S.-A. A. S., & Cli Fton, R. J. (n.d.). *Containment of Massive Hydraulic Fractures ABSTRACT*. http://onepetro.org/spejournal/article-pdf/18/01/27/2157781/spe-6089-pa.pdf/1

Spence, D. A., & Sharp, P. (1985). SELF-SIMILAR SOLUTIONS FOR ELASTOHYDRODYNAMIC CAVITY FLOW. *Proceedings of The Royal Society of London, Series A: Mathematical and Physical Sciences*, *400*(1819). https://doi.org/10.1098/rspa.1985.0081

Spence, D. A., & Turcotte, D. L. (1985). MAGMA-DRIVEN PROPAGATION OF CRACKS. *Journal of Geophysical Research*, *90*(B1). https://doi.org/10.1029/JB090iB01p00575

Suponik, T., Labus, K., & Morga, R. (2023). Assessment of the Suitability of Coke Material for Proppants in the Hydraulic Fracturing of Coals. *Materials*, *16*(11). https://doi.org/10.3390/ma16114083

Waters, G., Dean, B., Downie, R., Kerrihard, K., Austbo, L., & McPherson, B. (2009). *SPE 119635 Simultaneous Hydraulic Fracturing of Adjacent Horizontal Wells in the Woodford Shale*.

Wu, K., Olson, J., Balhoff, M. T., & Yu, W. (2017). Numerical analysis for promoting uniform development of simultaneous multiple-fracture propagation in horizontal wells. *SPE Production and Operations*, *32*(1). https://doi.org/10.2118/174869-pa

Wu, & Kan. (n.d.). *Front Matter Template*.

Zhao, J., Chen, X., Li, Y., & Fu, B. (2016). Simulation of simultaneous propagation of multiple hydraulic fractures in horizontal wells. *Journal of Petroleum Science and Engineering*, *147*. https://doi.org/10.1016/j.petrol.2016.09.021

Zheng, W., Silva, S. C., & Tannant, D. D. (2018). Crushing characteristics of four different proppants and implications for fracture conductivity. *Journal of Natural Gas Science and Engineering*, *53*, 125–138. https://doi.org/10.1016/j.jngse.2018.02.028

Appendix-A:

For plane strain condition, b_{ij} is defined as,

$$b_{ij} = a_{ij} - \frac{a_{i3}a_{j3}}{a_{33}} \tag{A-1}$$

$$\Delta_1 = 2(\beta_1 - \beta_2)$$

$$\Delta_0 = 4\beta_1\beta_2(\beta_1 - \beta_2)^2$$

$E' = \frac{4\Delta_1}{b_{11}\Delta_0}$ (For Anisotropic rock)

$E' = \frac{E}{2(1-\vartheta^2)}$ (For Isotropic rock)

Where a_{ij} are the material constants defined as,

$$a_{11} = \frac{1}{E_1}, \quad a_{22} = \frac{1}{E_2}, \quad a_{33} = \frac{1}{E_3}, \tag{A-2}$$

$$a_{12} = \frac{-\vartheta_{21}}{E_2} = \frac{-\vartheta_{12}}{E_1}, \quad a_{13} = \frac{-\vartheta_{31}}{E_3} = \frac{-\vartheta_{13}}{E_1}, \quad a_{23} = \frac{-\vartheta_{32}}{E_3} = \frac{-\vartheta_{23}}{E_2},$$

$$a_{66} = \frac{1}{G_{13}}$$

β_1 *and* β_2 are the imaginary part of complex root of the following characteristic equation,

$$b_{11}\mu^4 + 2(b_{12} + b_{66})\mu^2 + b_{22} = 0 \tag{A-3}$$

The definition of $H_{11}, H_{21}, H_{12}, and\ H_{22}$ those were used in calculating stress intensity factor at the fracture tip.

$$H_{11} = Im\left(\frac{\mu_2 p_1 - \mu_1 p_2}{\mu_1 - \mu_2}\right) \tag{A-4}$$

$$H_{12} = Im\left(\frac{p_1 - p_2}{\mu_1 - \mu_2}\right)$$

$$H_{21} = Im\left(\frac{\mu_2 q_1 - \mu_1 q_2}{\mu_1 - \mu_2}\right)$$

$$H_{22} = Im\left(\frac{q_1 - q_2}{\mu_1 - \mu_2}\right)$$

$$p_1 = b_{11}{\mu_1}^2 - b_{16}\mu_1 + b_{12} \tag{A-5}$$

$$p_2 = b_{11}{\mu_2}^2 - b_{16}\mu_2 + b_{12}$$

$$q_1 = b_{12}\mu_1 + \frac{b_{22}}{\mu_1} - b_{26}$$

$$q_2 = b_{12}\mu_2 + \frac{b_{22}}{\mu_2} - b_{26}$$

μ_1 and μ_2 are the complex root the characteristic equation given below:

$$b_{11}\mu^4 - 2b_{16}\mu^3 + 2(b_{12} + b_{66})\mu^2 + b_{22} = 0 \quad \text{(A-6)}$$